

# University of St Andrews



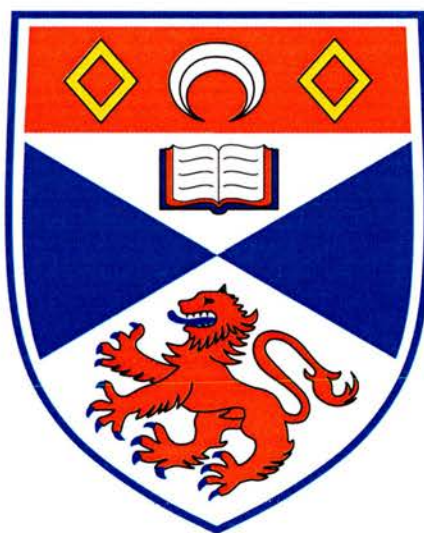
Full metadata for this thesis is available in  
St Andrews Research Repository  
at:

<http://research-repository.st-andrews.ac.uk/>

This thesis is protected by original copyright

# Integrated Optical Manipulation in Microfluidics

Simon J. Cran-McGreehin



Thesis submitted for the degree of Doctor of Philosophy  
of the University of St Andrews

March 31, 2006



Th F395

# Abstract

This Thesis presents a novel application of integrated optics to the field of optical manipulation. As pioneered by Ashkin, the optical forces exerted by laser beams can be used to manipulate microscopic objects, ranging from biological matter in solution through to atomic condensates in vacuum. Conventional systems use macroscopic optical components to couple beams from external laser sources into sample chambers. In this unique approach the chamber is built directly onto the semiconductor material in which the lasers are lithographically-fabricated, giving it two major advantages: small size and intrinsic alignment.

With the small size, many parallel operations can be conducted, each with their own dedicated, pre-aligned lasers, making for a versatile system that brings the advantages of miniaturisation and multiplexing to scientific studies of optical interactions. The intrinsic alignment removes the need for optical experience in the operator, making the power of optical manipulation more accessible to the broader scientific community. Observations can be made with any microscope system, and it requires only low voltages; indeed, it lends itself to automation, for some operations could be conducted without any external observation whatsoever, and under computer control.

As a first demonstration, this integrated optical manipulation device was applied to microfluidics. Particles in solution were flowed through channels adjacent to the lasers, whereupon demonstrations were made of trapping, shunting and spectroscopy of colloidal and biological matter. This paves the way for complex biological analysis chips where samples may be held, analysed and treated, and then guided to new interrogation regions, all by means of optical forces generated by the on-chip lasers, and without the need for external optical apparatus. Looking ahead, applications are foreseen in chemistry, cell culturing, gene therapy, spectroscopy, microfluidics and lab-on-a-chip medical tests, and also in fundamental studies of molecular motors, Brownian dynamics and Bose-Einstein condensates.

# Declaration

I, Simon Cran-McGreehin, hereby certify that this Thesis, which is approximately 40,000 words in length, has been written by me, that it is the record of work carried out by me and that it has not been submitted in any previous application for a higher degree.

Signature of candidate

Date ..13/11/06.....

I was admitted as a research student in October, 2001 and as a candidate for the degree of Doctor of Philosophy in October, 2002; the higher study for which this is a record was carried out in the University of St Andrews between 2001 and 2006.

Signature of candidate

Date ..13/11/06.....

I hereby certify that the candidate has fulfilled the conditions of the Resolution and Regulations appropriate for the degree of Doctor of Philosophy in the University of St Andrews and that the candidate is qualified to submit this Thesis in application for that degree.

Signature of supervisor

Date ..13/11/06.....

In submitting this Thesis to the University of St Andrews I understand that I am giving permission for it to be made available for use in accordance with the regulations of the University Library for the time being in force, subject to any copyright vested in the work not being affected thereby. I also understand that the title and abstract will be published, and that a copy of the work may be made and supplied to any *bona fide* library or research worker.

Signature of candidate

Date ..13/11/06.....

# Acknowledgements

I would like to thank the many people here in the School of Physics and Astronomy who have given assistance during the course of my studies. Professor Thomas Krauss offered me a studentship, and Professor Kishan Dholakia offered me an exciting project. I am indebted to them for the opportunity to develop my analytical skills through this work. I have learned much, and travelled far. I have enjoyed solving problems for a very practical goal, and have been thrilled to see success.

Mr George Robb has kept the fabrication facility on its feet, despite our best efforts; his skills are apparently unlimited, and he inspires a desire to do things well. The same can be said of Dr Donald Brown, in whose entertaining company an afternoon in the cleanroom would show how things should be done. Dr Rab Wilson is a fount of knowledge, from whom I learned the common sense approach to research. Dr Liam O'Faolin is our laser pioneer who taught me the first steps of laser fabrication and gave much more advice besides. Others too numerous to name have made contributions, but I feel the need to mention the technicians in the Electronics Workshop who have never tired of my questions, and also Mr Scott Johnson, the storeman who has brought several items from his treasure trove to facilitate my bizarre schemes.

Thanks are owed to colleagues who have assisted with the project in some specific way. Mr Phil Jess has conducted spectroscopy, Dr Lynn Paterson has provided cells and Dr Peter Reece has given advice about imaging. Thanks are also owed to the computing staff in the Mathematical Institute whose organised facilities made the creation of this Thesis possible. I must also thank my secondary school physics teacher, Mr Rollie, for making the subject interesting, where many are discouraged.

I greatly appreciate the encouragement that my parents have always given; I am glad that they are pleased with my achievements, and I hope that I can do even half of the good that they have done, and complain as little. I also appreciate having two such intelligent and generous brothers. I would like to acknowledge the wise influence of my late Grandma who asked if I was considering a Ph.D.; I hadn't been, but did so immediately. I would also like to thank EPSRC for providing funding and thus alleviating Grandma's only concern.

Finally, I want to express my sincere gratitude and love toward my infinitely talented wife, Alexandra. She has shared the ups and downs of Ph.D.-dom, and has sacrificed so much, especially when work took valuable time away from us. In a final act of generosity she has applied her great knowledge of Latex programming to transform my disparate drafts into this elegant tome.

# Contents

<b>Contents</b>	<b>iv</b>
<b>List of Figures</b>	<b>vii</b>
<b>1 Introduction</b>	<b>1</b>
1.1 Historical Background . . . . .	1
1.2 Magnitude of Scattering Forces . . . . .	2
1.2.1 Forces Acting Upon Planar Surfaces . . . . .	2
1.2.2 Forces Acting upon Spherical Particles . . . . .	5
1.3 Historical Moments in Optical Manipulation . . . . .	8
1.4 Comparison with Other Methods . . . . .	9
1.5 Novel Beam Geometries . . . . .	10
1.6 Biological Applications . . . . .	11
1.6.1 Initial Work . . . . .	11
1.6.2 Studies using Forces . . . . .	12
1.6.3 Genetic Manipulation . . . . .	13
1.6.4 Optical Analysis . . . . .	13
1.6.5 Conclusion of Review . . . . .	14
1.7 Dual-Beam Trap . . . . .	15
1.7.1 Background and Properties . . . . .	15
1.7.2 Device Concept . . . . .	15
1.7.3 Design Overview . . . . .	16
<b>2 Device Fabrication</b>	<b>20</b>
2.1 Overview of Chapter . . . . .	20
2.2 Standard Fabrication Techniques . . . . .	21
2.2.1 Outline of Polymer Processing . . . . .	21
2.2.2 Deposition of Thin Films by Evaporation . . . . .	22
2.2.3 Etching of GaAs-based Materials . . . . .	25
2.3 Fabrication Overview . . . . .	26
2.3.1 Lasers . . . . .	27

2.3.2	Microfluidics . . . . .	29
2.4	Complete Fabrication Instructions . . . . .	29
2.4.1	Preparation and Cleanliness . . . . .	30
2.4.2	Laser Ridges . . . . .	32
2.4.3	Inter-Ridge Insulation . . . . .	33
2.4.4	Top Contacts . . . . .	34
2.4.5	Back Contact . . . . .	35
2.4.6	Facets . . . . .	35
2.4.7	Channel . . . . .	36
2.4.8	Channel Lining . . . . .	37
2.4.9	Chamber and Capillaries . . . . .	38
2.5	Background and Optimisation . . . . .	38
2.5.1	Polymer processing . . . . .	39
2.5.2	Chemically-Assisted Ion Beam Etching (CAIBE) . . . . .	47
2.6	Superseded Methods . . . . .	51
2.6.1	Definition of Ridges and Facets . . . . .	51
2.6.2	Arrangement of Inter-Ridge Insulation and Facets . . . . .	53
2.6.3	Patterning Inter-Ridge Insulation . . . . .	53
2.6.4	SU8-2000 Polymer Processing . . . . .	56
2.7	Further Work . . . . .	59
<b>3</b>	<b>Semiconductor Lasers</b> . . . . .	<b>60</b>
3.1	Design Considerations . . . . .	60
3.2	Basic Semiconductor Processes . . . . .	61
3.2.1	Increased Conduction by Doping . . . . .	62
3.2.2	PN Junction and the Generation of Light . . . . .	64
3.3	Internal Laser Action . . . . .	65
3.3.1	Aspects of Particle and Wave Models . . . . .	65
3.3.2	Building up to a Laser Mode . . . . .	67
3.3.3	Benefits of Heterostructures . . . . .	68
3.3.4	Ridges . . . . .	72
3.3.5	Ridge Width and Depth . . . . .	74
3.4	Laser Performance . . . . .	77
3.4.1	Total Power within a Laser Cavity . . . . .	77
3.4.2	Model of a Single Round-Trip to Determine the Output Power . . . . .	78
3.4.3	Optimum Cavity Length . . . . .	80
3.4.4	Additional Electrical Considerations . . . . .	83
3.5	Power Estimation . . . . .	84
3.5.1	Reductions in Measured Power . . . . .	84
3.5.2	Power Emitted from Opposite Facets . . . . .	86

3.6	Final Considerations . . . . .	89
3.6.1	Additional Effects of SU8-2000 Channel Lining . . . . .	89
3.6.2	Beam Divergence . . . . .	89
<b>4</b>	<b>Optical Trapping Results</b>	<b>91</b>
4.1	Set-up, Measurements and Uncertainties . . . . .	91
4.2	Drag Force . . . . .	92
4.3	Motion in a Single Beam . . . . .	93
4.4	Equilibrium Position in a Dual-Beam Trap . . . . .	94
4.5	Axial Restoring Force in a Dual-Beam Trap: Recoil . . . . .	97
4.6	Transverse Q-value . . . . .	100
4.7	Conclusions of Physical Data . . . . .	103
4.8	Detection . . . . .	104
4.9	Demonstrations . . . . .	106
<b>5</b>	<b>Conclusions</b>	<b>110</b>
5.1	Fabrication . . . . .	110
5.2	Results . . . . .	112
5.3	Impact . . . . .	112
<b>6</b>	<b>Appendix</b>	<b>114</b>
6.1	Ray Optics Regime . . . . .	114
6.2	Direction of Photon Propagation . . . . .	114
6.3	Photon Momentum . . . . .	116
6.4	Power Striking a Three-dimensional Ring . . . . .	117
6.5	Number of Photons on Each Route . . . . .	118
6.6	Forces Due to Routes . . . . .	120
6.7	Accuracy of Model . . . . .	122
6.8	Mode Area and Force in a Device . . . . .	123
	<b>List of Abbreviations</b>	<b>125</b>
	<b>List of Publications</b>	<b>126</b>
	<b>Bibliography</b>	<b>127</b>

# List of Figures

1.1	A comet with its two tails . . . . .	1
1.2	Light incident upon planar surfaces . . . . .	3
1.3	Light interacting with a sphere . . . . .	5
1.4	Gradient force acting upon a spherical object . . . . .	6
1.5	Water droplet in a levitation trap . . . . .	7
1.6	Dual-beam trap with focused beams . . . . .	7
1.7	Forces in a single-beam tweezer . . . . .	8
1.8	Cross-section of Bessel beams . . . . .	10
1.9	Concept diagram of device . . . . .	15
1.10	SEM images of trapping channel . . . . .	17
1.11	Photographs of trapping channel . . . . .	18
1.12	Multiple functions along a channel . . . . .	18
1.13	Plumbing and electrical connections . . . . .	19
1.14	Test apparatus . . . . .	19
2.1	Photograph of a simple sorting device . . . . .	20
2.2	Processing of photosensitive polymers . . . . .	22
2.3	A crucible containing white-hot nuggets of pure gold . . . . .	23
2.4	Lift-off process . . . . .	24
2.5	Chemically-Assisted Ion Beam Etching (CAIBE) . . . . .	25
2.6	SEM image of the cross-section of a quantum well laser . . . . .	27
2.7	Photographs of laser fabrication . . . . .	28
2.8	Two-layer method for defining ridges . . . . .	32
2.9	Edge bead formation . . . . .	40
2.10	Lift-off mask for deep etching . . . . .	41
2.11	Discontinuity due to deep channel . . . . .	41
2.12	Exposure intensity in a polymer layer . . . . .	43
2.13	Exposure edge effects . . . . .	44
2.14	Rate at which LOR-7B recedes in lift-off mask . . . . .	46
2.15	Considerations in CAIBE processing . . . . .	47
2.16	Non-vertical etch profiles . . . . .	48

2.17	Etch data for laser ridges . . . . .	49
2.18	Effects of turbo drag upon etch profile . . . . .	50
2.19	Deep etching data for GaAs . . . . .	50
2.20	SEM image of poor quality facet . . . . .	51
2.21	Three configurations of facets and ridges . . . . .	52
2.22	Etch-back method for defining inter-ridge insulation . . . . .	54
2.23	SEM image of mesas in cross-section . . . . .	55
2.24	SEM image of “tear-off” method in cross-section . . . . .	55
2.25	Thicknesses of diluted SU8-2000.5 . . . . .	56
2.26	SU8-2000/PMMA mask for etching channel . . . . .	57
2.27	Thicknesses of blends of SU8-2000.5 and SU8-2050 . . . . .	58
2.28	Scheme for etching curved facets . . . . .	58
3.1	Electronic processes in intrinsic semiconductors . . . . .	62
3.2	Electronic processes in extrinsic semiconductors . . . . .	63
3.3	The operation of a pn junction . . . . .	64
3.4	Issues concerning cavity modes . . . . .	66
3.5	Sequence for laser action . . . . .	67
3.6	Properties of GaAs-based compounds . . . . .	69
3.7	Structure of QT1841 quantum well material . . . . .	70
3.8	Structure of DO451 quantum dot material . . . . .	72
3.9	Electrical and optical effects of deep and shallow etches . . . . .	73
3.10	Propagation of light in a rectangular waveguide . . . . .	74
3.11	Effects of ridge depth upon slope efficiency and threshold current in quantum dot lasers . . . . .	76
3.12	Effects of carrier concentration . . . . .	78
3.13	Photon population throughout a round-trip of a laser cavity . . . . .	79
3.14	Reasons for the existence of an optimum cavity length . . . . .	81
3.15	Effects of cavity length upon performance of quantum well and quantum dot lasers . . . . .	82
3.16	Effects of probe position upon output power . . . . .	83
3.17	Reductions of measured power . . . . .	85
3.18	Power-current performance of nine quantum dot lasers . . . . .	85
3.19	Comparison of powers emitted through opposite facets . . . . .	87
3.20	Additional optical effects of SU8-2000 lining . . . . .	89
4.1	Data of motion of a polymer sphere in a single beam . . . . .	94
4.2	Stills from footage of motion in a dual-beam trap . . . . .	95
4.3	Forces that determine the equilibrium position in a dual-beam trap . . . . .	95
4.4	Data for equilibrium position in a dual-beam trap . . . . .	96
4.5	Particle motion due to axial restoring force of a dual-beam trap . . . . .	98
4.6	Values of spring constant for different beam powers in a dual beam trap . . . . .	99
4.7	Forces that determine transverse Q-factor of a dual-beam trap . . . . .	100

4.8	Data for motion of a sphere as it escapes from a dual-beam trap . . . . .	101
4.9	Data for escape speeds of spheres from dual-beam traps . . . . .	102
4.10	Fluorescence signal from a sphere in a dual-beam trap . . . . .	104
4.11	Data for integrated detection methods . . . . .	105
4.12	Alignment of asymmetric particles within a dual-beam trap . . . . .	106
4.13	Vertical alignment of a planar crystal within a dual-beam trap . . . . .	107
4.14	Image of an SA2 cell in a dual-beam trap . . . . .	107
4.15	Configurations for simple sorting devices . . . . .	108
4.16	Sequence of stills showing the motion of a sphere in a simple sorting device . . . . .	109
6.1	Paths of rays through a sphere . . . . .	115
6.2	Axial Q-values for various routes within a sphere . . . . .	117
6.3	Definitions of angles $\theta_r$ and $\phi$ . . . . .	118
6.4	Numbers of photons on different routes . . . . .	120
6.5	Forces due to different routes . . . . .	120
6.6	Variation of axial force with sphere radius . . . . .	121
6.7	Improvements to accuracy of model . . . . .	122
6.8	Axial force for different refractive indices . . . . .	123

# Chapter 1

## Introduction

### 1.1 Historical Background

Light is one of the fundamental phenomena of everyday life. It is generally thought of as the portion of the electromagnetic spectrum to which our human eyes are sensitive, providing the illumination by which we image the world. Light does, however, extend beyond the scope of our senses, and its effects extend well beyond simple illumination.

As early as the 17th century, the German astronomer Johannes Kepler, during the studies that yielded his laws of planetary motion, noticed that the tails of comets, such as those of comet Hale-Bopp in Figure 1.1, always pointed away from the Sun. He surmised that some force emanated from the Sun, and in 1609,



Figure 1.1: A photograph of a comet with its two tails. The straight (upper) tail consists of charged particles that stream away from the Sun under the electromagnetic influence of the solar wind. The curved (lower) tail consists of uncharged dust that also moves away from the Sun, and therefore must be under the influence of some other force. (Courtesy of Igor Gladstone; taken from <http://wsx.lanl.gov/WebPub/images/>).

the same year in which he published his first law of planetary motion, he proposed the notion of flying from the Earth to the Moon, propelled solely by the radiation pressure of light. The idea of radiation pressure was given added credence by the theoretical predictions of Scottish physicist James Clerk Maxwell's 19th century wave model of light. In addition, Albert Einstein's 1905 study of the photo-electric effect led to his 1916 assertion, via the particle model, that light, although possessing no mass, does indeed carry linear momentum that can be transferred to matter during collisions. Experimental verification waited until Arthur Compton's 1923 confirmation of predictions made by himself and by Debye in 1922. In a beautifully simple experiment the transfer of momentum from light to matter, and hence the very existence of photon momentum, can be demonstrated by simply setting off a bright flash bulb in front of a small, thin sheet of metal foil in air. The intense flash contains sufficient photons of light, each colliding with the foil, that the force exerted by the light is manifested as an audible "ping".

And so, the prospect of sailing through not the blackness of space, but actually on the light that fills it, was made real. However, it is only a realistic proposal because, in outer space, there is plenty of room to accelerate macroscopic bodies over long periods of time, and in the absence of resistive forces, such as strong gravity and viscous drag. These forces completely swamp our observation of natural, macroscopic optical forces here on Earth, but, on a small enough scale, high intensity laser beams can provide sufficient photon momentum to exert meaningful forces upon microscopic particles.

The first demonstration of the exertion of mechanical forces by light upon microscopic matter was published by *Ashkin (1970)* of Bell Laboratories. Using a Gaussian beam from an argon ion laser operating at 514.5 nm, he utilised the radiation pressure to accelerate a variety of microscopic particles: latex spheres in water, air bubbles in glycerol, and water droplets in air. It was observed that a second, unexpected force also acted upon the particles, attracting the latex to the central propagation axis of the beam, and repelling the bubbles. It was identified as the gradient force, and was used in conjunction with the radiation pressure to trap the latex spheres at the equilibrium point of two counter-propagating beams. The paper concluded with a plan to extend the technique to the manipulation of atoms and molecules, using resonant frequencies to cool and guide them. Thus this one paper opened up an entirely new field of practical research that was guided and interpreted by the developing theoretical work.

## 1.2 Magnitude of Scattering Forces

### 1.2.1 Forces Acting Upon Planar Surfaces

The order of magnitude of the simple scattering force, or radiation pressure, can be ascertained by considering Figure 1.2. It illustrates two cases of a ray (a bundle of photons) striking the flat end of a cylinder at normal incidence; one cylinder is made of a perfect reflector, and the other of a polymer. The fundamental issue is that momentum is a vector parameter,  $p$ , and so any change in either the magnitude or the propagation direction of a photon constitutes a change in the momentum. The magnitude of the momentum is

$$p = \frac{nh}{\lambda} = \frac{n\epsilon}{c} \quad (1.1)$$

where  $h$  is Planck's constant,  $n$  is the refractive index of the medium,  $\lambda$  is the wavelength of the light in a vacuum,  $c$  is the speed of light in a vacuum and  $\epsilon$  is the photon energy. The magnitude of the momentum depends upon the medium, and in water ( $n = 1.33$ ), for example, is  $9.69 \times 10^{-27} \text{ kg m s}^{-1}$  for Ashkin's argon ion laser beam, and  $3.86 \times 10^{-28} \text{ kg m s}^{-1}$  for the GaAs-based quantum dot lasers (emitting at 1290 nm) that were used in this project.

The changes that exert forces are due to changes in propagation direction, which occur as a result of reflection and refraction at the interfaces between optically-different media. In the cases of normal incidence in Figure 1.2, the reflected rays undergo a  $180^\circ$  change of direction, so the change in momentum per reflected photon is just twice its incident momentum; the transmitted photons are not refracted and so their direction does not change. If the total optical power striking an area is  $P$ , then the number of photons involved per second is  $P/\epsilon$ , and the total photon momentum striking that area per second is simply

$$p_{\text{total}} = \frac{Pn}{c} \quad (1.2)$$

and the fraction of this that is transferred to the particle as a force is determined by the reflectivity and by the so-called Q-factor. The Q-factor gives the fractional change in momentum along any particular axis; in this case it is a measure of the change in momentum along the axis of propagation, and, because the photons are reflected back in their tracks, the value is  $Q = 2$  for each photon. That is, the magnitude of the change in momentum is twice that of the incident momentum. More is said about this in the Appendix.

If 1 mW of power, at any wavelength, is incident upon a perfect reflector (with reflectivity  $R = 1$ ) that is immersed on water of refractive index 1.33, then the total force is  $8.86 \times 10^{-12} \text{ N}$ . If the particle is a metal cylinder with dimensions of radius  $2.5 \mu\text{m}$  and length  $3.3 \mu\text{m}$  (so that its volume equals that of a  $2.5 \mu\text{m}$ -radius sphere, a typical test particle) and mass density  $10^4 \text{ kg m}^{-3}$ , then the acceleration thus induced would be  $13.6 \text{ m s}^{-2}$ . If this force was unopposed then the particle would quickly attain speeds

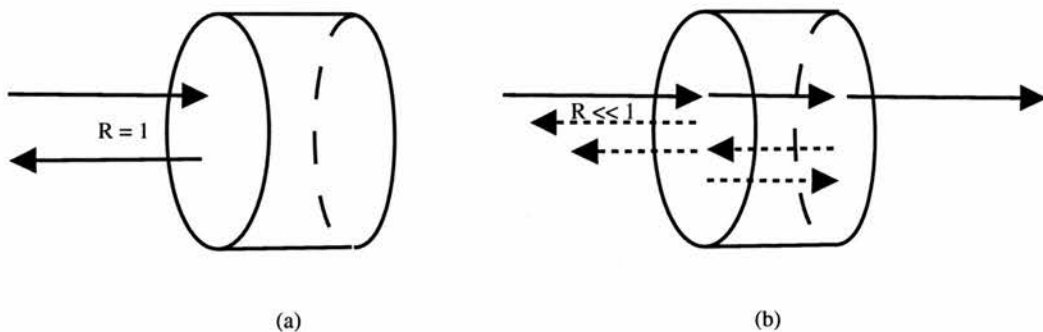


Figure 1.2: Light at normal incidence upon a cylinder made of (a) a “perfect reflector” (e.g. metal), and (b) a low index medium (e.g. polymer). The refractive index contrast determines how much of the incident light is reflected at the boundary and hence how much momentum is transferred by reflection.

that are more common in the macroscopic world; that is, it would not remain for long in the laser beam. In reality these accelerations are not seen, firstly because the laser beam would diverge, reducing the incident power along the path, and, secondly because the drag forces acting between the fluid and the particle would oppose the acceleration and limit the maximum speed.

In Figure 1.2(b), the low refractive index contrast between the water and the polymer means that a much smaller proportion of the incident light is reflected backwards, giving a smaller force; but of the transmitted light, a certain amount is reflected from the second interface, adding to the force, noting that the photon momentum is different in the polymer. Of this reflected light, a little is reflected back into the particle from the first interface, partially cancelling the forward force. Indeed, an ever-diminishing amount of light remains in the polymer cavity, but the low reflectivity makes this insignificant. The number of photons thus reflected at each interface depends upon the reflectivity, which, at normal incidence between two media of refractive indices  $n_1$  and  $n_2$  is

$$R = \left( \frac{n_1 - n_2}{n_1 + n_2} \right)^2 \quad (1.3)$$

which is 0.00849 for polymer of refractive index  $n_p = 1.6$  in water of refractive index  $n_w = 1.33$ . The total change in momentum per second, that is, the force, is

$$\Delta p_{\text{total}} = \frac{2P}{c} [n_w R + n_p (1 - R) R - n_p (1 - R) R^2 + \dots] \quad (1.4)$$

which, for 1 mW of power, is  $1.64 \times 10^{-13}$  N. This translates to an acceleration of  $0.99 \text{ m s}^{-2}$  for a polymer cylinder with aforementioned dimensions and mass density  $1050 \text{ kg m}^{-3}$ . Again, such accelerations are not seen in reality, but they do contribute towards net forces that are significant on the microscopic scale, and are typically of the order of pico-Newtons ( $10^{-12}$  N) or less. In reality, the photons will not strike the surface at normal incidence, but at some angle that depends upon the beam's focusing, and upon the particle's position within the beam. By means of comparison, the force exerted by gravity upon such a particle is  $6.67 \times 10^{-13}$  N, which would be balanced by 4.1 mW of power striking the polymer cylinder.

The most common use of optical manipulation is in the movement of biological cells. However, cells are essentially bags of water containing small structures, so their refractive indices are not much higher than that of water, and so the reflectivity, and hence the radiation pressure, are small; a typical value is  $n = 1.367$  for a red blood cell. The situation is made worse by the fact that the refractive index of water increases with salinity. For example, the refractive index of pure water at some wavelength at  $20^\circ\text{C}$  is 1.3333, whereas the value is 1.3339 for sea water (3.5ppt salts of various types) at the same temperature and wavelength. The same effect is seen with other dissolved materials, so the buffer solutions (mixtures of dissolved salts and nutrients) that are essential for keeping cells healthy have the effect of reducing the forces that are exerted. Some gain is made by increasing the temperature, because the refractive index of pure water falls from 1.335 at  $0^\circ\text{C}$ ; many cells are happiest at higher temperatures, at which the index contrast is slightly higher. For these reasons, manipulating entire cells usually requires several tens of milli-Watts of optical power, as will be discussed with reference to the literature in Section 1.6.2.

### 1.2.2 Forces Acting upon Spherical Particles

Returning now to the work in *Ashkin (1970)*, it is necessary to consider the forces that act upon non-planar surfaces such as spheres. This will be considered in more detail in the Appendix, but for now a qualitative view is given. The idea of momentum transfer is still central to the argument, but it needs to be extended to two dimensions, as in Figure 1.3 which shows a cross-section of the reflection and refraction of light due to a polymer sphere of refractive index 1.6. It is important that the refractive index of the sphere is higher than that of the surrounding medium, and a little more will be said about that later on. Whereas before, the direction of a photon's momentum was either unchanged or completely reversed, in this case its direction can be altered incrementally, and so it is best expressed in terms of axial and radial components. In addition, this two-dimensional picture gives a qualitative description of the three-dimensional case.

The incremental changes mean that the axial Q-factor of a photon can range from 0 to 2. It can also be deduced that the radial (or transverse; that is, across the beam) Q-factor of a photon can range from 0 to 1. The overall Q-factor (in either direction) due to a beam of light will be combinations of those for the individual photons, and will fall within the same bounds.

The situation is complicated by the polarisation of the light, and by the fact that the reflectivity varies around the surface of the sphere, but these effects are ignored at present. Also, an ever-diminishing amount of light will travel around inside the sphere, but the basic effects can be understood with reference to just the two high-lighted rays. There are, then, four changes in momentum to be considered: an axial and a radial, for both the reflected and transmitted photons, and the net force acting upon the sphere is determined by the size of each momentum change and by the relative numbers of photons that follow each path. However, in these cases, when the refractive index contrast is low, the reflectivity is very low over all but the largest of incident angles, and so the reflected forces are generally much less powerful than the refracted forces.

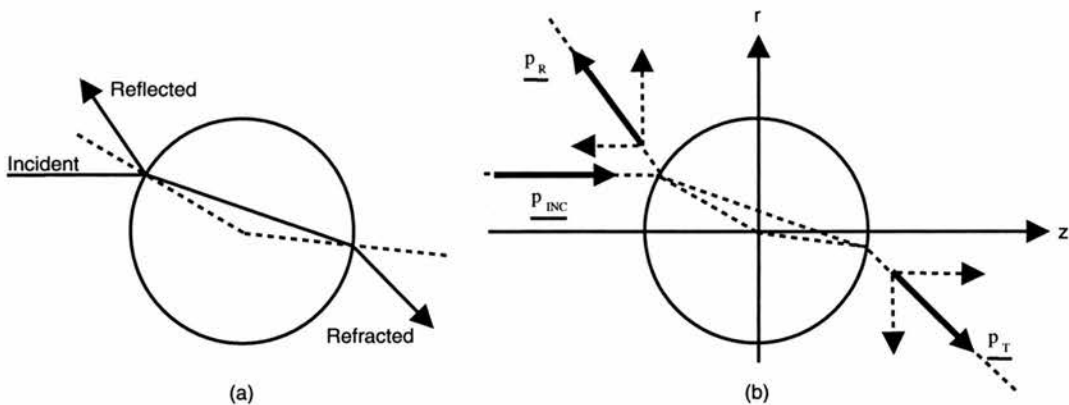


Figure 1.3: A two-dimensional illustration of light interacting with a sphere ( $n_w < n_p$ ), showing only two effects: (a) The simple ray optics model shows the directions in which reflected and refracted rays travel. (b) The different angles of propagation lead to changes in photon momentum, expressed in terms of vector components. In this case the incident photon's momentum,  $\underline{p}_{INC}$ , has an axial component, but no radial component. The reflected and transmitted photons' momenta,  $\underline{p}_R$  and  $\underline{p}_T$  (black arrows), can be expressed as radial and axial components (dotted arrows).

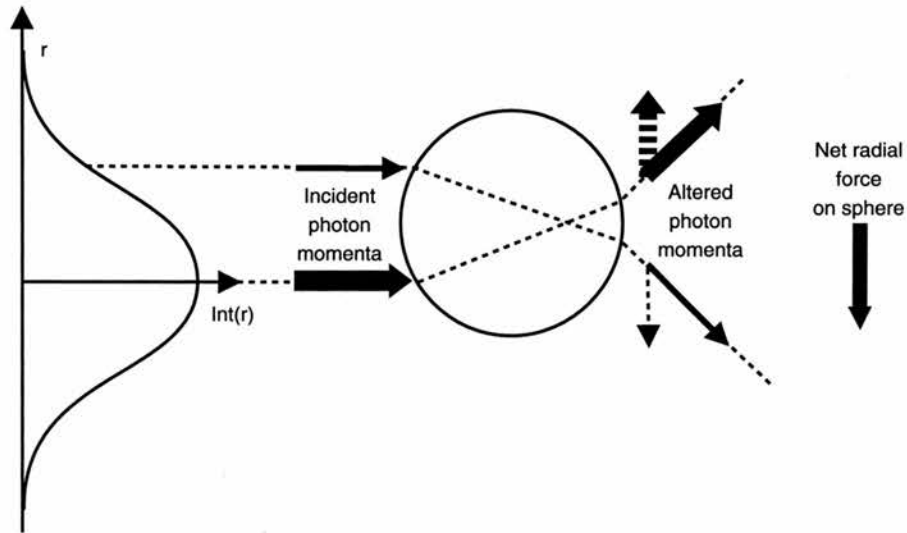


Figure 1.4: Gradient force in a two-dimensional slice through a Gaussian beam. The thickness of the ray represents the intensity at that radius from the beam's centre. The refraction (as in Figure 1.3) leads to radial forces, whose net effect draws the sphere onto the beam's axis.

The reflected axial momentum determines the scattering force, but it has a lower efficiency than for the flat reflectors, although it is augmented by the refracted axial momentum. Even then, because of the beam's divergence, the radiation pressure falls along the beam's axis, limiting the range over which Gaussian beams can usefully transport particles.

It is the radial forces that lead to the unexpected gradient force in *Ashkin (1970)*, and they can be understood by considering Figure 1.4. The resultant gradient force depends upon the relative intensities acting on opposite halves of the sphere: higher intensities relate to higher numbers of photons per second and hence larger forces. If the sphere is initially off the laser beam's central axis, then the higher intensity at the beam's centre will give a larger reflected radial force that will try to push the sphere out of the beam. However, because the reflected forces are so much weaker, it is overcome by the refracted radial force that tends to draw the sphere onto the beam's axis, giving the dipole force witnessed by Ashkin, but only for particles whose refractive index is larger than that of the surrounding medium. For the opposite regime, as is the case for air bubbles and hollow dielectric spheres, the refraction will occur in the opposite directions, pushing the particle away from the higher intensity at the centre of the beam, and thus providing no radial confinement, or at least not in a Gaussian beam.

The combination of the gradient force and the scattering force in a divergent beam serves to draw particles into the centre of the beam, and to then push them along the axis. This provides only two-dimensional (radial) confinement, unless the axial scattering force is balanced by some other force. In the simplest of traps, the levitation trap, it is gravity that does the balancing, and this is illustrated in Figure 1.5. It shows a negative of an image obtained during the author's Senior Honours project, in which a droplet of water is suspended in air above the focal point of an upward-pointing Gaussian beam of a Nd:YAG laser emitting at 1064 nm.

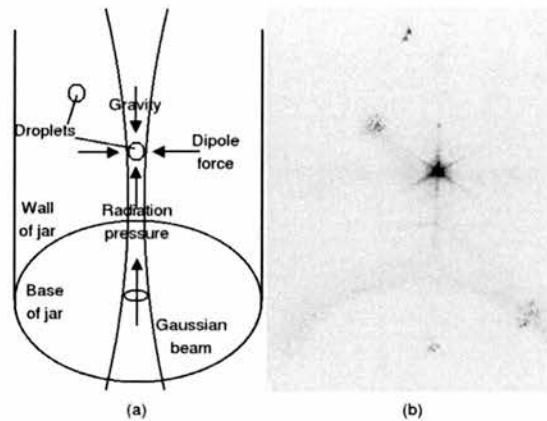


Figure 1.5: Water droplet in a levitation trap: (a) a sketch of the apparatus that illustrates the features seen in (b) a negative image taken of a trapped water droplet in air.

As demonstrated in *Ashkin (1970)*, the easiest way in which to provide entirely optical three-dimensional confinement is to use two counter-propagating beams. As illustrated in Figure 1.6, they were each brought to a focal point, after which they both diverged, and it was in this over-lapping region of divergence that particles experienced three-dimensional confinement. The radial forces act in two dimensions, and the axial confinement occurs at the point where the opposing axial forces balance. This dual-beam optical trap has been created using the outputs from two optical fibres (*Constable et al. (1993)*) and was used in this project, of which more details will be given in Section 1.7. It should be noted that the trap can be created without focusing the beams, and by simply moving the sources of the divergent beams closer together, as was the case in this project, and in some fibre traps.

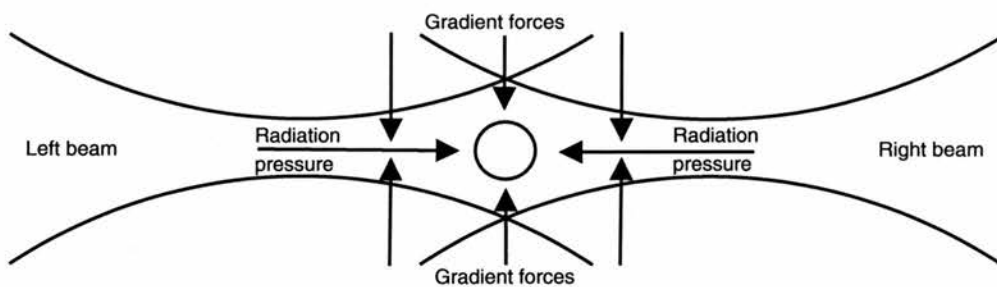


Figure 1.6: A dual-beam trap created with two focused Gaussian beams. The radiation pressure (as in Figure 1.2) from each side of the diagram pushes particles towards the equilibrium point where the forces balance, whose position depends upon the relative intensities of the beams. The gradient force (as in Figure 1.4) draws the particle onto the axis of the beams.

### 1.3 Historical Moments in Optical Manipulation

Having opened up this amazing new toolbox of micromanipulation, Ashkin continued the work apace. The 1970s saw advances in levitation both in air (*Ashkin (1971)*) and in vacuum (*Ashkin (1976)*), and also in atomic manipulation (*Schieder et al. (1972)*, *Bjorkholm et al. (1978)*) that eventually saw the inauguration of the field of atom optics. This progress continued in the 1980s, with the publication of what is now the standard reference for atomic-light interactions (*Gordon and Ashkin (1980)*), culminating in 1986 with the creation of the first stable, single-beam trap (*Chu et al. (1986)*), but that is where this Thesis' interest in atomic manipulation ends. In that same year this trap was used in work with microscopic spheres (*Ashkin et al. (1986)*), superseding the less stable single-beam levitation trap. The situation is illustrated in Figure 1.7: for simplicity the effects of reflected light are ignored, and only the refracted rays are considered. To the left of the beam's focal point the refracted rays act to reinforce the scattering force. However, beyond the focal point, the propagation direction of the rays can be altered such that they gain axial momentum; the sphere must therefore lose axial momentum and experience a force that draws it back towards the focal point. If the focus is tight enough then this dipole force can overcome the scattering force, leading to axial confinement in a single beam, provided that the refractive index of the sphere is higher than that of the surrounding medium.

This new style of trap then took optical manipulation in a new and radically important direction when *Ashkin and Dziedzic (1987)* and *Ashkin et al. (1987)* used these traps to hold biological material. From that time onwards the main focus of optical manipulation has been on the development of tools for the handling, interrogation and treatment of biological samples. Indeed, that is where its main strengths are of most importance: the optical methods provide no material contact, avoiding the risks of contamination that spoils biological samples, and also of damage and adhesion that are apparent with micro-mechanical tools, such as the glass capillaries used in *in vitro* fertilisation, which also tend to be fragile themselves. In addition, the optical methods are applicable across a wide range of microscopic studies, due, in part, to the broad spectrum of wavelengths and the variety of available beam profiles, from which can be selected the optimum optical interactions for each situation. Also, the forces are suitable for biological work. A single

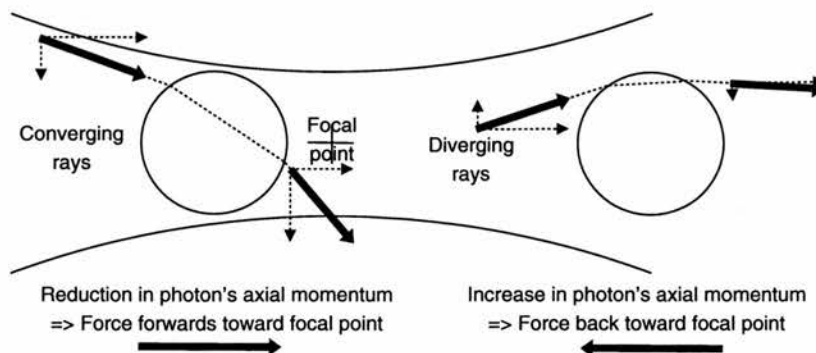


Figure 1.7: The dipole force in an optical tweezer. Ignoring the effects of reflection that would always act to push the particle to the right, it can be seen that the changes in axial momentum beyond the focal point generate a force that pulls the particle back to said focal point, thus providing axial confinement.

beam tweezer can be tuned with a resolution of the order of pico-Newtons, and motion can be monitored to within nanometres, under certain circumstances (*Ignatovich and Novotny (2006)*). The dual-beam trap can be used to measure forces in the range of pico-Newtons to 10pN, as discussed later with reference to the optical stretcher (*Guck et al. (2001)*).

## 1.4 Comparison with Other Methods

Optical manipulation is certainly not the only means by which microscopic matter can be interfered with, and it is not without its disadvantages. One of its main drawbacks has already been discussed in Section 1.2.2; that is, the reliance on refractive index results in small forces acting upon water-based cells in water-based media. Other problems relate to the absorption of light by the trapped particles. Fluorescent signals from molecules within cells, whether naturally-occurring or added artificially, can provide useful information. This analysis can be conducted using the trapping beam if the wavelength is suitable; but prolonged exposure to such excitation will bleach the fluorescent molecules so that they no longer respond reliably. Absorption of light by the general cellular material causes heating. Water absorbs more strongly in the infrared part of the spectrum, and more complex molecules absorb more towards the ultraviolet region; it is, therefore, a general problem, but a careful choice of wavelength can reduce the problems in each specific application. That said, there is evidence that the actual temperature rises in cells are of the order of only 1°C every few minutes per 100 mW of applied optical power. So it is believed that the damaging effects of absorption are more likely to be the result of photochemical damage due to absorption at specific wavelengths, rather than the result of thermal denaturing of molecules within the cell as a whole.

With these issues in mind optical trapping can be compared to other methods of micromanipulation; useful categories for comparison are the resolution of forces and distances, the risk of damage to samples, and the generality of the technique. When considering the forces it is important to recognise the difference between the maximum magnitude and the resolution. The maximum available force determines the usefulness for moving objects for such applications as arranging, sorting and rotation. The resolution determines the smallest force that can be exerted and therefore the usefulness of the technique for examining the responses of small objects to such forces, such as the motion of the molecular motors that move materials within cells.

The technique that is most similar to optical trapping is dielectrophoresis, which uses an oscillating electric field to exert a force on a particle. The size of the force depends upon various factors that include the electrical properties of the medium and the particle, the shape and size of the particle, and the frequency of oscillation of the electric field, but some force is exerted upon every particle, making it a very general method. The electric field can be provided by a laser beam, allowing the “landscape” to be tailored with sub-micron resolution for the intricate movement of objects. The forces are of the order of nano-Newtons, so they can move objects more effectively than can optical methods, but they reveal less detail about subtle motions. In addition, the need to tailor the chemical composition of the fluid to maximise the forces is not necessarily compatible with the nutritional needs of biological cells.

Magnetic forces can be used to manipulate particles, but only those that possess a magnetic moment, al-

though that can be added to a particle by the addition of a magnetic bead. By carefully altering the applied magnetic field, forces of the order of fempto-Newtons can be applied, giving very accurate information about small-scale biological functions. In addition, magnetic forces can apply torsion to objects, revealing more complex information. At the other end of the force scale atomic force microscopy (AFM) has a resolution of the order of tens of pico-Newtons. This limit is imposed by the thermal noise within the system, which consists of a tiny tip that is attracted by varying amounts to a surface in close proximity. However, its spatial resolution is excellent (of the order of Angstroms), and such motion on that scale can be measured on a millisecond timescale. The biggest risk is that the tip will touch the sample, contaminating the former and damaging the latter. Another limitation is that it must be conducted under vacuum, prohibiting studies of live biological specimens. A variation upon this theme is a kind of scanning force microscope (*Ghislain and Webb (1993)*) that uses an optically-trapped particle as a stylus; it is more delicate than a mechanical tip, making it suitable for analysing soft samples in water. Finally, micro electromechanical systems (MEMS) have been fabricated for the manipulation of particles; these are more like miniaturised versions of macroscopic tools, and include the fine capillaries that are used in *in vitro* fertilisation. They exert large forces (nN -  $\mu$ N), with the associated pros and cons, and suffer from the risks of adhesion and sample damage.

Each of these various methods has its uses in the broad field of micromanipulation and can be tailored to meet specific challenges in niche areas. They provide a continuum of techniques from which a complete picture of biological functions can be built up, in particular where the regions of overlap allow comparison and corroboration of evidence.

## 1.5 Novel Beam Geometries

In the quest for ever more articulate methods of control, more elaborate beam geometries and even large-scale optical landscapes have been generated using simple optical components, holograms and spatial light modulators (SLMs). Figure 1.8 shows images, again obtained during the author's Senior Honours project, of three Bessel beams, so called because their radial intensity patterns are Bessel functions of different orders. The set of solutions was determined by *Durnin (1987)*, who then generated zero-order Bessel

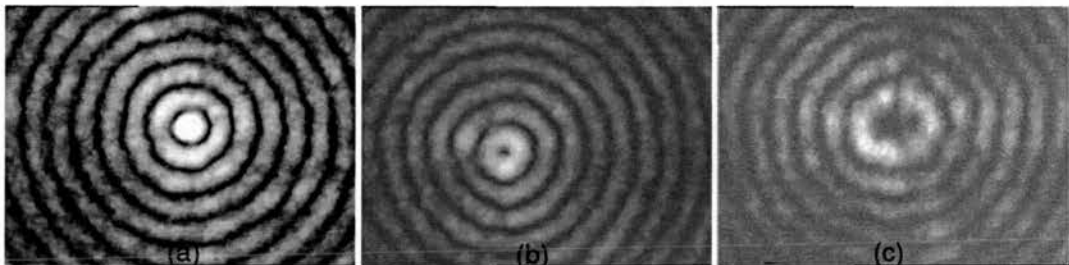


Figure 1.8: Cross-sections of (a) 0<sup>th</sup> order, (b) 1<sup>st</sup> order and (c) 4<sup>th</sup> order Bessel beams. The total beam power is split amongst the rings, but the profile is invariant along the axis of propagation for many millimetres. The 0<sup>th</sup> order beam has a central maximum, whereas the higher-order beams have central minima that attract particles whose refractive indices are lower than that of the surrounding medium.

beams using an annular slit (*Durnin et al. (1987)*), although more efficient methods use axicons (cones of glass) or holograms, the latter being used to generate the beams in Figure 1.8. Their unique property is that, although the photons are all diverging from the beam's axis, interference causes the ring patterns to be constantly regenerated over an axial range of up to a few millimetres, giving an unchanging intensity pattern, and the appearance of a non-diverging beam. They are therefore very useful in the long distance transport of particles, where Gaussian beams perform poorly. The zero-order beam will push higher index particles along its high intensity central axis, whereas the higher order beams are useful for moving lower index particles, which are repelled from the high intensity ring and hence confined within the low intensity central region.

Certain novel beam shapes are used to induce the rotation of particles. It can be done using tweezers (*Higurashi et al. (1994)*) to simply "man-handle" particles around, but it is more elegantly achieved by either the interference of two Laguerre-Gaussian beams (*Paterson et al. (2001)*) to create lobes that turn an asymmetric particle, or by exploiting a particle's birefringence, be it natural or manufactured form birefringence (*Neale et al. (2005)*). Sorting particles into different populations is an important precursor to tests and treatment, and doing so by optical methods removes the risk of contamination (*Huber et al. (1995)*). One method that passively sorts particles rapidly, by size, is the "optical washboard potential" (*MacDonald et al. (2003)*), which is an example of the use of holograms or SLMs for the creation of "optical landscapes". Other sorting methods use laser beams to push particles upon command (*Wang et al. (2005)*), and this has been extended to use fluorescence as a trigger (*Fu et al. (1999)*). The sorting and arrangement of biological particles draws upon work with general colloidal matter, which includes studies of Brownian motion (*Simon and Libchaber (1992)*), non-intuitive attractive forces (*Crocker and Grier (1996)*), entropic forces (*Crocker et al. (1999)*), and phase transitions in the creation of lattices, firstly in standing wave potentials (*Choudhury et al. (1985)*) and later in more complex geometries.

## 1.6 Biological Applications

### 1.6.1 Initial Work

With this ever-increasing repertoire of techniques at hand, scientists have achieved remarkable feats in biological optical manipulation. The very first biological matter to be trapped (*Ashkin and Dziedzic (1987)*) was tobacco mosaic virus (TMV), but that was not because of its biological nature, but rather because its rod shape ( $\sim 20$  nm in diameter,  $\sim 300$  nm in length) allowed a demonstration of alignment along the trap's axis. The potential for using optical tweezers in biological research seems to have become apparent only when unintentional bacterial contamination introduced cells into this medium. The resulting paper was dimmed only by the fact that the argon ion laser's 514.5 nm emission was strongly absorbed by haemoglobin, chlorophyll and even water, so that even low powers ( $>5$  mW) tended to kill, or "opticute", the cells. *Ashkin et al. (1987)* addressed this problem by using the 1064 nm emission of a Nd:YAG laser. E-coli and yeast cells were undamaged by high beam powers ( $>50$  mW); the yeast cells then managed to reproduce normally whilst being held in the trap. A variety of other cells was then trapped, showing the broad applicability of optical manipulation to biological work, and a series of important demonstrations was given: a single-beam

tweezer was used to sort cells, and to deform the surface membranes of pliable cells; and two tweezers were used in conjunction to hold, orientate and deform cells. Importantly, this was extended to the organelles (intracellular objects, analogous to organs in a body) within cells, which was then investigated further by *Ashkin and Dziedzic (1989)*, focusing on the elasticity of cytoplasm. The fields of research that were opened up by this seminal trio of papers are discussed more fully in various review articles including *Ashkin (2000)*, and are summarised below.

### 1.6.2 Studies using Forces

Studying the magnitudes and directions of the forces involved in biological processes was very difficult before the advent of optical tweezers. But tiny, controllable optical forces induced upon very small volumes can be used to oppose or mimic the biological forces, allowing estimates of the associated energies that help in the understanding of the processes. They also permit studies of the mechanical properties of biomolecules and structures, which are of interest from both fundamental and engineering points of view. Cells and other large objects can be probed directly with optical tweezers, but small or fast-moving objects can only be worked with if “handles” (microspheres or organelles) are chemically bound to them.

The first application was in a study of the flagella (whip-like tails) that propel certain bacteria (*Block et al. (1989)*). Using handles it was then applied to mechanoenzymes (*Block et al. (1990)*, *Ashkin et al. (1990)*), the “molecular motors” that move organelles around within cells on the “railway lines” of actin filaments. It eventually yielded results for the forces exerted by a single kinesin molecule *in vivo* (*Kuo and Sheetz (1993)*), and a similar result was obtained for the motors that drive RNA transcription (*Yin et al. (1995)*), and those that move particles within an immune system cell towards a target cell (*Burkhardt et al. (1993)*). Such accuracy cannot be obtained via any other method. Molecular interactions on the outer membranes of animal cells (as opposed to plant cells whose rigid cell walls cover the membranes) were investigated by tweezing cells and antigen-coated microspheres and then bringing them together with known forces. The work also yielded information about the growth of connective tissue, and about the forces (*Mammer et al. (1996)*) that provide the activation energies (*Wei et al. (1999)*) for immune response reactions.

Mechanical properties were also investigated, especially those of cell membranes, both internal (*Bar-Ziv et al. (1995a)*, *Bar-Ziv et al. (1995b)*) and external, and also those of biomolecules. The elasticity of red blood cells (*Svoboda et al. (1992)*) was found to change as they grow older (*Bronkhorst et al. (1995)*), and the same changes were exhibited by cells during hypoxia (lack of oxygen) by *Wang et al. (1993)*. The mechanical manipulation of cell membranes was used recently to develop the “optical stretcher” for the detection of cancerous cells (*Guck et al. (2001)*). The disease inhibits the creation of the elastic fibres of actin that maintain the cell’s physical integrity, reducing its strength and thus increasing its elasticity, which can be measured in terms of its deformation under a certain optical force.

All of these applications illustrate the usefulness of optical tweezing for revealing information about the health of a cell population, whether it is from a blood test or a bacterial culture. The ability to stretch the cell membranes (*Dai and Sheetz (1995)*) has also been put to further practical use, allowing control over the growth direction of algal cells (*Leitz et al. (1995)*) and neurons, which could result in treatments

for nerve damage. The mechanical properties of bio-molecules have been investigated, firstly microtubules with (*Kurachi et al. (1995)*) and without (*Feigner et al. (1996)*) handles, and then DNA (*Wang et al. (1997)*). Such molecules, especially DNA with its chemical patternability, have great engineering potential both for the definition of nano-structures and in the creation of nano-machines.

### 1.6.3 Genetic Manipulation

Optical tweezing has proven to be useful in the field of genetics, offering general methods with which chromosomes can be tampered. The high intensity of a pulsed laser has been used as a “scalpel”, first for cutting into and moving cells and organelles (*Seeger et al. (1991)*), and then to encourage the fusion of two tweezed cells (*Steubing et al. (1991)*), and even of “artificial cells”. A combination of scalpel and tweezers (with handles) allowed the manipulation of chromosomes for the analysis of mitosis (cell division) by *Liang et al. (1993)*, and genes have been removed from, and added to, chromosomes for simple gene therapy experiments. Recently, photoporation, or optoporation as it was originally dubbed (*Palumbo et al. (1996)*), has emerged as a powerful technique for gene therapy, allowing the insertion of genes into a nucleus through a small, photo-induced hole that promptly heals up. This method has utilised a variety of different wavelengths, some simply because a particular laser was available, but others because they had some advantage, as in the following example. A common technique in gene therapy experiments is to introduce into a cell, along side the gene of interest, additional genes that produce green fluorescent protein (GFP); the presence of the fluorescence indicates that the other genes have also been incorporated into the cell’s DNA. A violet laser diode has been used to photoporate cells, the same laser being used to excite GFP fluorescence (*Paterson et al. (2005)*), thus combining two techniques in one laser system.

### 1.6.4 Optical Analysis

Whilst being held in a trap, particles are easy targets, not only for surgery, but also for spectroscopy and other indignities that can reveal much about their nature. The necessary light can be provided by the trapping beam itself, but that generally allows only simple measurements of scattered light; more specific techniques, such as fluorescence spectroscopy and Raman spectroscopy, usually require an additional beam of an appropriate wavelength. An in-depth study of spectroscopy in microchemistry (*Masuhara et al. (1994)*) has been published, but for now it suffices to briefly describe these two forms of spectroscopy. Most of the photons that are incident upon a material are scattered elastically in random directions; this is Rayleigh scattering. However, a small number are absorbed by processes that excite electrons into higher energy levels; some photons are never seen again, which is measured in terms of the absorption co-efficient, whilst others are re-emitted. The mechanism of re-emission uses the electronic energy levels within the material; the primary energy levels are determined by the electronic configuration within the molecule, but each level is further divided into vibrational energy states.

In fluorescent materials there exists a pathway by which the excited electron moves to a lower electronic energy level, losing energy to thermal vibrations within the molecule, and then moves to its original, unexcited state, emitting a photon whose energy is lower than that of the incident photon. The fluorescence signal

is hence distinct from the excitation signal, and can be detected with a correct arrangement of filters and a spectrometer. It does, however, require an excitation wavelength that matches the absorption spectrum of the fluorophore, and it is only applicable to the small number of materials that fluoresce. However, these can be used as labels for tracking other particles to which they are chemically-bound, be they small molecules or large colloidal particles (*Jensen-McMullin et al. (2005)*), and in gene therapy experiments, as discussed in Section 1.6.3. The issue of specific absorption wavelengths is constantly being addressed by the development of new laser systems to span the spectrum, and by the development of artificial fluorophores, such as soluble quantum dots whose absorption and emission wavelengths can be tuned via the size to which they are allowed to grow.

Raman spectroscopy is seen in non-fluorescent species, making it a more general technique. The process starts with the absorption of a photon, of virtually any wavelength, which excites an electron into a higher energy state. The positions of the original and excited states do not matter; what matters is the fact that some of the electrons relax down by a single vibrational energy level and then back down to their original levels with the emission of a photon. The difference between the absorbed and emitted wavelengths, translated into a wavenumber [ $\text{m}^{-1}$ ] gives a measure of the vibrational energy level spacing, which is characteristic of the material. That is the key advantage of Raman spectroscopy, detecting the clear signatures of a variety of materials, even being able to distinguish the changes that occur as biological materials age, allowing the progress of diseases to be monitored non-invasively. It has certain drawbacks, most noticeable of which are the small wavelength difference and the weak emission signal (1 in  $10^7$  of incident photons), which can be overcome only with the use of an advanced spectrometer and a sensitive detector, respectively.

### 1.6.5 Conclusion of Review

It is clear that optical methods provide very good solutions to a wide variety of problems in micromanipulation, especially in biological applications. Although other techniques, as discussed in Section 1.4, have their advantages, and although there are cases in which they are more accurate, or stronger, or otherwise better than their optical analogues, none of them offers such a wide range of tools. Indeed, not only are many optical tools available, but they can be tailored for specific situations by choosing wavelengths from across the spectrum. Sometimes one wavelength can perform a variety of different tasks, making the system simpler and more compact. In other situations, though, it is helpful to have different wavelengths performing different functions; they do not interfere with one another, allowing a level of multiplexing that is not possible with magnetic or MEMS methods.

A particular part of the biological field is the lab-on-a-chip market, in which biological tests are conducted on miniaturised devices that are portable and often automated. The aim is to make tests cheaper and easier. They sometimes use optical methods, but the large components tend to be an obstacle: that is where the system presented in this Thesis fits in. It allows optical functions to be conducted on a single, integrated chip, bringing the power of optical manipulation to bear upon the world of lab-on-a-chip testing.

## 1.7 Dual-Beam Trap

### 1.7.1 Background and Properties

As a first demonstration of this new technology, the dual-beam trap was considered. It has been largely over-looked since the advent of its single-beam counterpart, the optical tweezer. This is mainly because more work is needed to focus two beams, let alone to align them with one another. It is also because the trapping occurs in the diverging regions of the beams, so the intensity, and hence trapping efficiency, are lower than for tweezers that trap particles at the high intensity focal point. But this divergence gives the dual-beam trap two advantages: a lower intensity that is less likely to cause damage to particles, and a larger catchment area that is useful for gathering particles together. Another difference is that to move the tweezer, the beam's focal point must be moved, but the beam power and trap strength are maintained, whereas the equilibrium point of the dual-beam trap can be moved by simply varying the relative beam powers, but that changes the strength of the trap. The advantages of the dual-beam trap have only really been exploited since the demonstration of the first fibre optic trap (*Constable et al. (1993)*), a design that reduces the number of optical components and allows the insertion of laser beams deep within microfluidic devices where normal objectives cannot reach. It has been used in lab-on-a-chip position sensing (*Jensen-McMullin et al. (2005)*), for Raman spectroscopy (*Jess et al. (2006)*), and for optical binding (*Metzger et al. (2006)*). The various advantages make the dual-beam trap a valuable first demonstration of this new technique presented in this Thesis. It is anticipated that most of the dual-beam techniques that have been published to date can be replicated in this system, but with the advantages of small size and intrinsic alignment.

### 1.7.2 Device Concept

By way of introduction, Figure 1.9 shows the initial concept diagram of the device. This does not show all of the details of a real device, but rather illustrates some of the proposed functions. The device is created in GaAs-based laser material, that will be described in more detail in Chapter 2. For now it suffices to say

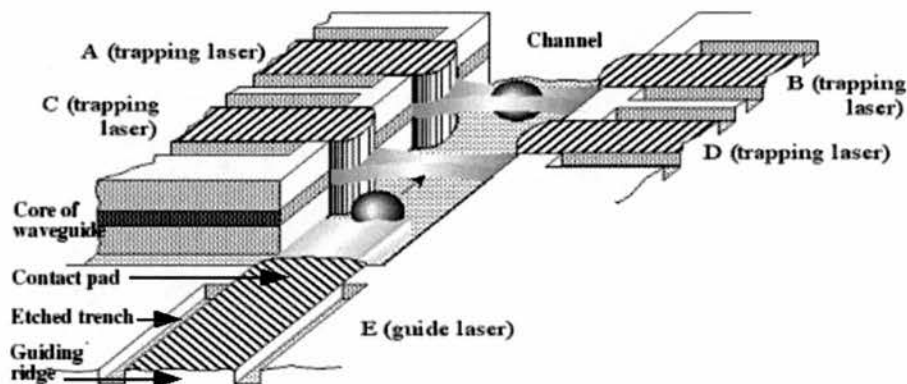


Figure 1.9: Concept diagram of device showing two proposed functions (propulsion and trapping) and some details of the lasers.

that the material generates light via the injection of electrical carriers, and that this light can be shepherded into a coherent laser mode by waveguiding ridges and partially-reflecting facets. One of these facets on each laser points into a channel that is etched into the GaAs-based material, allowing samples to interact with the laser beams. Laser E performs the simplest function, pushing particles along the channel, whilst pairs of lasers (A and B or C and D) form dual-beam traps, holding particles against the flow. This simple configuration would allow particles to be moved into trap AB, analysed in some manner, released, pushed by laser E, held in trap CD and analysed in some other manner. Expanding upon this prototype, any two-dimensional configuration of lasers could be fabricated, allowing the complex pumping, trapping, analysis and sorting of particles.

The work in this project used colloidal particles, such as polymer spheres and biological cells, in water, but the use of water necessitates the addition of electrical insulation, which is not shown in Figure 1.9. In many ways this application is a much simpler proposition than the other envisioned application, namely the trapping of Bose-Einstein condensates (BECs), as in *Gustavson et al. (2002)*, which could also be created on a chip (*Feenstra et al. (2004)*). However, that work, carried out in a vacuum, would negate the need for the electrical insulation, but would be more demanding in other ways.

The use of integrated optics endows the device with two major advantages: small size and intrinsic alignment. This compares favourably with conventional optical manipulation systems that take the outputs of external lasers and use discrete optical components to shape the beams and to couple them into sample chambers. These components take up space, and require careful alignment, neither of which are problems with this device. Its small size comes about for a number of reasons. Firstly, the diode lasers are naturally small, typically 1-2 mm in length, and a few microns in width. Secondly, their output beams feed straight into the sample chamber, so no optical components are necessary. This second factor also removes coupling losses, which is important because the diode lasers generate only up to 20 mW, which, for diverging beams, does not provide much leeway. The device's intrinsic alignment stems from the microfabrication techniques that have been developed for use in the electronics and optical communications industries. The positioning of the features relies upon patterned masks that are created by electron beam lithography with an accuracy of  $\sim 20$  nm. The dimensions of the features depend partly upon the use of the masks, which will be discussed later, but they are of less importance than the actual positioning; any mis-alignment of facing lasers will reduce the trap efficiency.

To summarise, the major advantage of this technique is that, whereas conventional optical manipulation systems couple external light sources into a sample chamber, this approach integrates the sample chamber directly onto the light source.

### 1.7.3 Design Overview

The primary aspect of the design is that of the fabrication of the lasers, which is explained in more detail in Chapter 2. For now it suffices to say that they have the same requirement as any other lasers: a gain medium, a pumping mechanism, a waveguiding mechanism, and partially-reflective facets. These can be discussed with reference to Figure 1.9. The dark band represents the core of the heterostructure, within which are located either quantum wells or quantum dots that provide the optical gain. Those used in this

project emitted at 980 nm and 1290 nm, respectively; the quantum wells were used for the initial tests and the quantum dots for the main experiments. The electrical pumping of the gain material is provided by electrical injection through the contact pads on the top surface. There are etched regions along the side of each laser, leaving ridges that provide the horizontal waveguiding, and vertical confinement is provided by the heterostructure. Etched facets define the length of the laser cavity providing feedback to sustain the laser mode, whilst also transmitting some of the power into the channel.

The waveguiding confines the laser beams to a small volume within the GaAs, and they naturally diverge upon exiting the GaAs. The vertical confinement is much tighter than the horizontal confinement, so the vertical divergence is greater. For ease of viewing, this vertical divergence is not included in the concept diagram. In fact, the concept diagram also shows cylindrical lenses that bring the beams, horizontally, to focal points within the channel. This would provide higher powers within the traps, and could even allow the realisation of a single beam optical tweezer, but the manufacture of such curved facets has yet to be perfected. Indeed, in some ways, a more significant advance would be the ability to focus the beams vertically, counteracting the larger divergence, thus having a bigger impact upon trap efficiencies, but vertical facet shaping is even harder to achieve. So, the actual devices presented in this Thesis have neither horizontal nor vertical beam-shaping, and instead use simple planar facets that give diverging Gaussian beams.

An accurate illustration of these features is given by the SEM images in Figure 1.10, which show the lasers terminating in the vicinity of the etched channel, before the polymer lining had been added. The photographs in Figure 1.11 show a plan view and a cross-section of the channel after the addition of the insulating SU8-2000 polymer, which is necessary to separate the electrically-active laser diodes from the water that holds the colloidal particles. A thin layer of the polymer covers the base, and thicker layer is lithographically-defined to coat the walls of the channel. A lid of glass or plastic is placed on top of the polymer insulation, creating a sealed channel with a small volume so that most of the colloidal material should pass through the laser beams. In the plan view the lasers are indicated by the gold contact pads, and in the cross-section the beams exit through the facets at the top of the GaAs-based material, about halfway up the polymer wall, and they overlap in the channel to create dual-beam traps. So, with a little study, Figures 1.10 and 1.11 should give a clear idea of how the concepts of Figure 1.9 were translated into a real device.

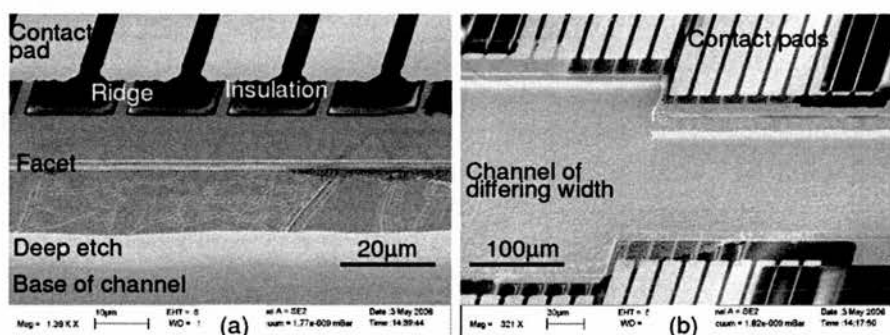


Figure 1.10: SEM images of trapping channel showing (a) the configuration of the lasers, the etched facets and the deeply-etched channel, and (b) pairs of lasers facing across the channel. The devices are viewed at 45° to the surface, and the SU8-2000 polymer has not yet been applied.

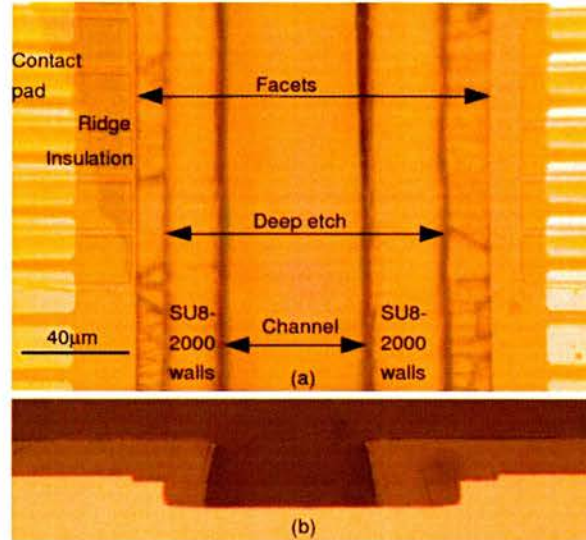


Figure 1.11: Photographs showing the channel with the electrical insulation: (a) a plan view showing the ends of the lasers on either side of the trapping channel; (b) a cross-section through the trapping channel, showing the depth of the facets, the deeply-etched channel and the polymer lining. To introduce the liquid, capillaries are laid down inside the polymer lining, and a lid is laid directly on top of the polymer walls.

Under lower magnification Figure 1.12 shows a plan view of a specific device that features in Chapter 4. Along the trapping channel there are alternating sets of dual-beam traps and single lasers facing into side channels. In addition, there are lasers at the right end of the channel that could provide propulsion between the different sections. This design illustrates the ease with which the individual components (lasers and channels) can be configured for different purposes, and also multiplexed for parallel processing. In this case, for instance, particles can be moved along the main channel (either by the lasers or by an externally-generated fluid flow), and a different test could be conducted at each trap, allowing the progressive separation of particles into the different side channels.

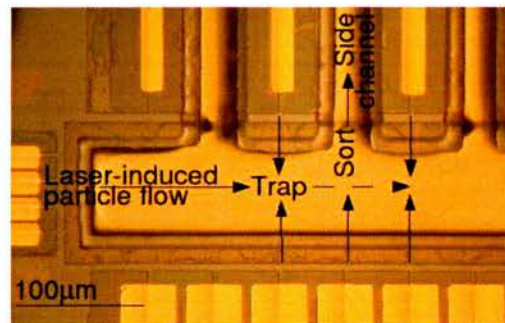


Figure 1.12: Multiple functions along a channel. This photograph shows a plan view of a device in which dual-beam traps alternate with side channels along the length of the main channel. Tests can be conducted at each trap site and particles could be ejected by a laser into a side channel, allowing a mixture of particles to be sorted into various categories.

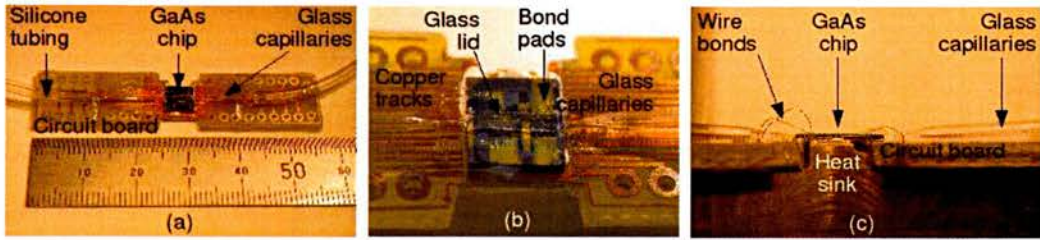


Figure 1.13: Plumbing and electrical connections. Photographs showing (a) the circuit board to which an external power supply can be connected and that also provides structural support for the capillaries, with the GaAs chip mounted in the middle (ruler marked in mm); (b) a close-up view of the chip, including the wire bonds that connect it to the circuit board; and (c) a side view of the chip.

Figure 1.13 (a) shows the full extent of the circuit board, to which wires can be soldered, facilitating an interface with a low voltage computer control board. Figure 1.13 (b) shows the piece of GaAs material; the length of the lasers, as indicated by the extent of the gold contact pads, accounts for much of the size, as do the larger “bond pads” via which the lasers can be wire-bonded to the electrical circuit board. Also shown are the plumbing connections that allow the introduction of solutions, and the glass chamber that is placed on top of the GaAs device, creating a water-tight system in which solutions can flow, whilst allowing observation from above. Figure 1.13 (c) shows these features from the side. The wire-bonding has yet to be perfected, so during the project voltages were applied using micro-positioning probes, as seen in Figure 1.14. Clearly the large items take up far more space than does the device itself, which provides the motivation for the wire-bonding and the computer interfacing. The microscope was used only for observation, and could, in future, be removed in some cases. When it is required, its size could be reduced by using a normal objective; the long working distance objective was necessary only because of the need to allow clearance for the electrical probes.

Having outlined the position of this technology in the field of optical manipulation, as well as some of the planned tests and the device’s layout, it is now appropriate to consider the details of its fabrication in Chapter 2. The performance of the GaAs-based lasers is investigated in Chapter 3, and the use of the devices to demonstrate useful functions is reported in Chapter 4.

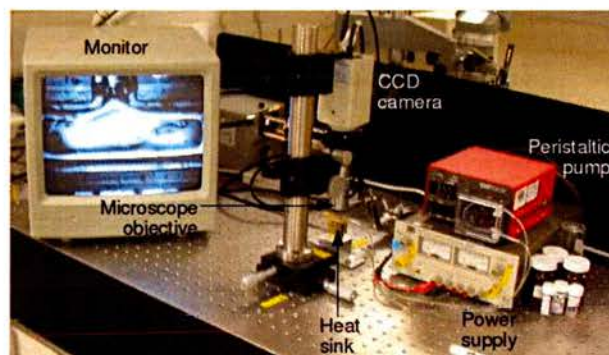


Figure 1.14: Test apparatus. The electrical probes could be removed, and even the microscope is not essential, showing just how small this technology can be.

## Chapter 2

# Device Fabrication

### 2.1 Overview of Chapter

The primary purpose of this Chapter is to provide a detailed list of instructions from which a device could be replicated, such as the simple sorting device seen in Figure 2.1. However, because the work in this Thesis could be of interest to scientists from a variety of disciplines, and not just those with a micro-fabrication background, this Chapter begins with two introductory Sections. Firstly, Section 2.2 gives a brief overview of the standard fabrication techniques that were used in the project. Secondly, Section 2.3 gives a simple overview of the fabrication; it expands upon Section 1.7, and provides a context in which to understand the instructions. Only then are the detailed protocols given. Thereafter, Section 2.5 discusses the background of the techniques, and the investigation and optimisation that were required for the deduction of the protocols, but only those readers who are interested need wade through the details.

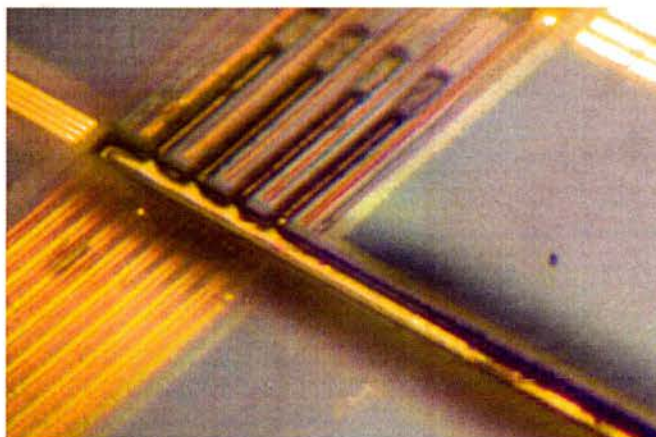


Figure 2.1: Photograph of a simple sorting device (as discussed with reference to Figure 1.12), viewed at an angle to the surface. Particles flow along the main channel (of width  $\sim 80 \mu\text{m}$ ), and can be held in dual-beam traps, and then pushed into the side channels, all using the on-chip lasers.

## 2.2 Standard Fabrication Techniques

The GaAs-based material in which the lasers were fabricated consisted of a 500  $\mu\text{m}$ -thick substrate of GaAs onto which layers of specific chemical compositions had been grown by molecular beam epitaxy. The quantum well material, named QT1841, was grown at the National III-V Semiconductor Facility at Sheffield University, U.K., and the quantum dot material, named DO451, by Nanosemiconductor GmbH, Dortmund, Germany. These layers created a heterostructure via which the electrical and optical properties were tuned. Upon receipt of these materials, all further processing was done in the cleanroom fabrication facilities at the University of St. Andrews, by the author. The modifications that created the lasers used standard techniques that fell into two categories: adding layers to the surface and removing portions of the heterostructure; the addition of layers was further sub-divided into polymer processing and metal deposition by evaporation. These standard techniques are now discussed.

### 2.2.1 Outline of Polymer Processing

Polymers can be added to the surface by spin-coating solutions of the polymer in a solvent, after which they are dried by baking. The thickness depends upon the viscosity of the solution and the spin speed. These polymers can constitute permanent features in their own right, or they can be used as sacrificial layers in other processes; in fact, their use as sacrificial masks in etching leads to the name “resists”. Some can then be patterned using U.V. lithography through masks in a mask aligner machine and are called photoresists, and others can be patterned by electron beam lithography; the former type, first suggested by *Andrus (1957)*, was used in this project. The mask aligner machine allows the operator to position the sample beneath the desired mask feature, before giving it a timed exposure. The energy of the photons provides the energy for reactions that either destroy polymer chains, making them more susceptible to specific solvents, or promote cross-linking between chains, making them more resistant to specific solvents. This discriminating dissolving is known as development, just as in photography, and the former polymers are known as positive resists, whilst the latter are called negative resists; both processes are illustrated in Figure 2.2. In this work, a negative resist called SU8-2000 was used (as distinct from the older SU8) to create permanent features: SU8-2000.5 (14% solids) for thin layers ( $\sim 400$  nm), SU8-2050 (72% solids) for thick layers ( $\sim 25$   $\mu\text{m}$ ), and blends of the two for intermediate thicknesses. It is developed in EC solvent, which is then rinsed in IPA and then dried with nitrogen. SU8-2000 is transparent and very resilient to chemical attack; so tough, in fact, that there is a \$3,000 reward for the discovery of a solution-based process that can remove it. Sacrificial layers were made from a positive resist called SR1800, of which two different blends were used: SR1805 for thin layers ( $\sim 500$  nm), and SR1818 for thicker layers ( $\sim 1.8$   $\mu\text{m}$ ). It is developed in MF319, rinsed in water and dried with nitrogen. Once it has served its purpose it can be dissolved in acetone and rinsed in IPA. Hard bakes make it tougher, and sometimes SVC-14 positive resist stripper (whose rinsing agent is water) is required.

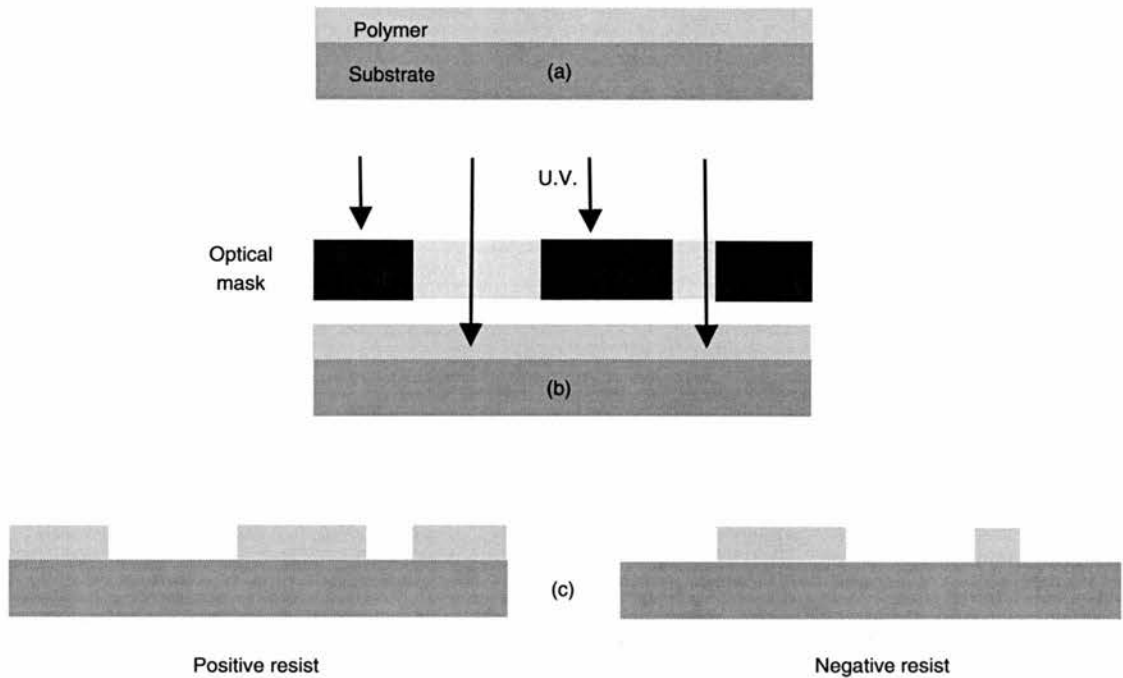


Figure 2.2: Processing of photosensitive polymers: (a) spin-coating gives a uniform layer that can be baked to remove any remaining solvent; (b) exposure with U.V. light (through a mask) causes reactions in the polymers; (c) development in a solvent reveals a copy of the mask feature.

### 2.2.2 Deposition of Thin Films by Evaporation

Another way of adding material to the surface is evaporation. In this project, an Edwards 360A electron-beam evaporation was used, in which a crucible containing either a metal such as gold or nickel, or a dielectric material such as silicon nitride or boron, is heated by the impacts of an electron beam, under vacuum, as seen in Figure 2.3. The evaporated material forms a vapour that condenses on the inside of the vacuum chamber, including on the surface of the sample, creating a layer whose thickness can be controlled by the evaporation time, and whose quality is affected by the evaporation rate and the vacuum pressure. A slower rate allows more time for the atoms to settle into preferred sites on the surface, and a lower pressure means that there are fewer foreign particles to hinder the flow of evaporated material and to contaminate the deposited layer. The method is wasteful of material, coating the entire chamber, rather than just the sample. Also, the impacts of high energy electrons on the metals can generate x-rays that can damage the samples, and the electrons themselves can affect electron-sensitive polymers such as PMMA. Thermal evaporation uses an Ohmic heater instead of an electron beam, but it is still wasteful. In addition, all evaporation methods are intrinsically unsuitable for compounds because the evaporation rate of each component element depends upon its vapour pressure; the different values result in different rates for each element and so the deposited layer lacks the correct composition.

A method that does not suffer from this problem, and which is therefore suitable for dielectrics, is sputtering, in which a source is bombarded with ions (such as argon ions) to eject a beam of the source



Figure 2.3: A crucible containing white-hot nuggets of pure gold. The impacts of electrons heat the metal, forming a vapour within the vacuum chamber, that then condenses on the samples.

material, which then settles on the sample to form a layer. The ejection from the source is an impact phenomenon, so the rate of ejection depends upon the amount of material at the surface, rather than upon its vapour pressure. So, even if one element in a compound is ejected more quickly than another, that has the effect of depleting the surface supply of the former element, so that the relative rates remain constant. For this reason, sputtering is suitable for the deposition of dielectric compounds, and materials can be modified further by the introduction of gases, such as oxygen and nitrogen. Other advantages are that the large area of the target provides a more uniform plume of material and hence a more uniform layer over larger samples, and no damaging x-rays are generated. The main disadvantage is cost, a sputtering system being more complicated and more expensive than an evaporator.

All such evaporation techniques are suitable for creating nm-scale thicknesses, even up to several 100 nm, but more advanced techniques are needed for more delicate applications. For example, various forms of epitaxy allow deposition with an accuracy of single atomic layers. They come under different names, but all follow the basic principles of molecular beam epitaxy (MBE), in which the relevant materials are introduced into the chamber in the form of gaseous compounds that react to liberate the desired atoms. They then settle at bonding sites on the surface of the target. The application of heat provides sufficient thermal energy to agitate the atoms out of any undesirable sites, creating a high quality layer. A slow flow rate allows the creation of layers with an accuracy of a single monolayer. The flow can be stopped, the chamber evacuated of remaining gas, and a new combination of gases can be introduced to create the next layer. The heterostructures in the GaAs-based laser materials were grown in such a manner.

Whatever its source, a deposited layer can be patterned by means of a polymer mask that is removed by a solvent such as acetone, taking the over-lying deposit with it, and leaving behind only the deposited material that is in direct contact with the substrate. This process, known as “lift-off”, is an example of polymers being used as a sacrificial layer, and is illustrated in Figure 2.4. It uses SR1805 and also LOR (lift-off resist)-7B, which is not photosensitive, but which is soluble in MF319. Therefore, a feature can be defined lithographically in the SR1805 and then developed, at which point the LOR-7B is laid bare to the MF319 that then dissolves it anisotropically, creating an undercut. This undercut then creates a discontinuity in a deposited layer of material, a gap through which solvents can gain access to the polymers. When dissolved by said solvents, the polymers no longer support the layers that then float off, leaving only those layers that are in direct contact with the substrate.

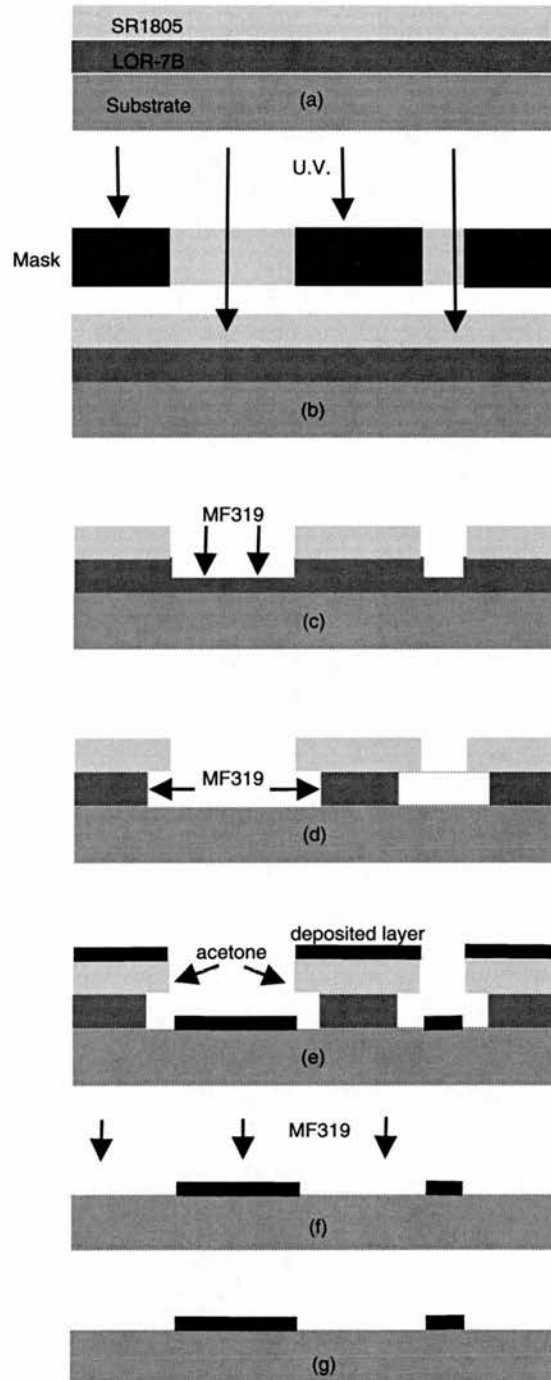


Figure 2.4: Lift-off process for patterning layers of metal: (a) spin coating and baking; (b) exposure; (c) development of exposed SR1805 by MF319; (d) LOR-7B is soluble in MF319 and so dissolves where the SR1805 is absent; (e) after deposition of a metal or dielectric layer by evaporation, acetone is used to remove the SR1805; (f) MF319 removes the LOR-7B; (g) the deposited material is left on the substrate.

### 2.2.3 Etching of GaAs-based Materials

The removal of material from the heterostructure is broadly divided into two main categories: wet and dry etching. In wet etching a solution dissolves the material, and tends to etch isotropically and roughly. In dry etching a gaseous reactant is introduced to the sample, under vacuum, sometimes with the addition of ion beam bombardment to provide both energy for the reactions and a degree of directionality, or anisotropy. In this work, all of the GaAs etching was done using Chemically-Assisted Ion Beam Etching (CAIBE), which is discussed in *Tyrell et al. (1991)* and illustrated in Figure 2.5. Chlorine gas is introduced through a ring into the vicinity of a heated stage to aid the physical bombardment of GaAs- and InP-based materials via singly-charged argon ions under high vacuum. The physical impacts act isotropically downward, ejecting atoms from the surface; the chemical chlorine etching acts anisotropically, reacting with the ejected atoms,

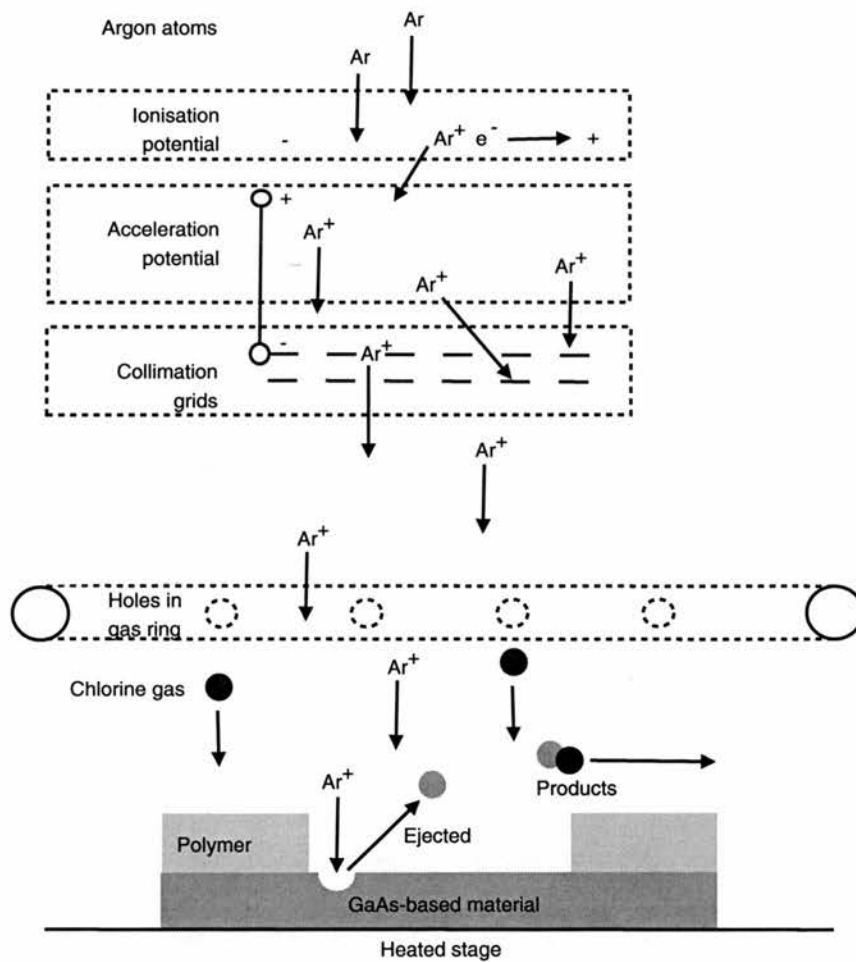


Figure 2.5: Chemically-Assisted Ion Beam Etching (CAIBE). From the top: Argon atoms are ionised to give  $Ar^+$  ions that are then accelerated by an electrostatic potential. Two grids block those ions that are travelling at large angles to the vertical axis, leaving a beam of ions travelling downwards. They strike the surface of the material, ejecting atoms that then react with chlorine gas, and the products move off into the vacuum.

and the product compounds then move away into the vacuum. These two components, the physical and the chemical, can be balanced in order to give a vertical profile, which is important for the laser facets, but less important in other applications on these devices.

The intensity [ $\text{W m}^{-2}$ ] of the physical bombardment over the area of the sample is determined by the beam voltage (typically 200-1500 V) that imparts kinetic energy to the ions, and the beam current (typically 10-20 mA). The beam current can be translated to the ion flux by dividing by the cross-sectional area of the beam, and then dividing by the value of a single electronic charge,  $e$ , which is the charge carried by each argon ion. This ion flux can be increased, with a corresponding increase of  $\sim 25\%$  in the etch rates, by adding a neutraliser current of electrons that shield the ions from one another's mutual repulsion, thus reducing the beam's divergence, while the high energies in the beam prevent the electrons and ions combining to form atoms.

The effect of the chemical component is determined by the combination of the chlorine concentration and the temperature of the stage. Increasing either will increase the etch rate, but care must be taken: temperatures above  $125^\circ\text{C}$  tend to hard bake SR1818 masks, making them difficult to remove, and too much chlorine tends to cause the growth of "grass", an undesirable by-product that is discussed further in Section 2.5.

## 2.3 Fabrication Overview

The fabrication of an integrated optical trapping device involved about a dozen different processes with at least one hundred distinct steps. These were divided into two groups, the laser fabrication and the addition of the microfluidic components. Of these, the laser manufacture came first, followed by that of the microfluidics, allowing the lasers to be tested prior to proceeding with the final fabrication steps. The other reason that dictated this order is that the deeply-etched microfluidic channels distorted subsequent layers of polymer, giving non-uniform layers that affected the lithography and other processes.

Dimensions were measured by one of three methods: Scanning electron microscope (SEM) images have a maximum magnification of  $\sim 100,000$ , and a resolution of  $\sim 20$  nm. Traces from a Dektak<sup>3</sup> surface profiler gave a vertical resolution of  $\sim 50$  nm and a horizontal resolution that depended upon the length of the scan, but could be as good as  $\sim 2$   $\mu\text{m}$ . Observing through an optical microscope's  $100\times$  objective and making measurements on a calibrated graticule in the eye-piece allowed a resolution of  $\sim 0.5$   $\mu\text{m}$ . It could easily be used for horizontal measurements, and could be used for vertical measurements if the sample was cleaved and stood on its end. Non-destructive, vertical measurements of deep features could be made by adjusting the optical microscope's focal plane from the top of the feature to its base, noting the difference in the heights on the calibrated dial whose resolution was  $\sim 0.5$   $\mu\text{m}$ .

### 2.3.1 Lasers

As was mentioned in Chapter 1 and is explained more fully in Chapter 3, the lasers required four basic features. These are illustrated in Figure 2.6, which shows an SEM image of the cross-section of a quantum well laser; the operation and fabrication of the quantum dot lasers are the same, varying only in the ridge dimensions. Firstly, an optical gain medium in which light could be generated was defined by the heterostructure, and so was already present. Secondly, pumping of this gain medium was provided by electrical injection through metal contact pads; these were defined by lift-off, and the optimum structure was determined to be 20 nm nickel followed by 200 nm gold, as discussed in Section 2.4.4. Thirdly, waveguiding to confine the generated light to a stable, sustainable mode was provided by the heterostructure in the vertical direction, and by a shallow ridge in the horizontal direction. The ridges were created by etching material from either side, and SU8-2000.5 polymer was added to these etched regions in order to insulate them from the top contact pads so that the current would pass through only the ridges, giving optimum pumping of the mode. Fourthly, partially-reflecting facets that provided both a useful output and feedback into the laser cavity were created either by cleaving the material, or by etching through the heterostructure.

The sequence of photographs in Figure 2.7 illustrates the laser fabrication process, as viewed from above one end of the lasers. The first step was the shallow etching of regions; the unetched regions in between were the guiding ridges. The ridges were transferred photolithographically into an SR1805 photoresist mask, using a two-step process that is explained in Section 2.5. The ridge pattern was then transferred into the heterostructure to the desired depth using the CAIBE machine; a low power (3.5W) etch provided the necessary etch depth precision. The remaining photoresist was removed in SVC-14 in an ultrasonic bath, ready for the application of the electrical insulation that prevented current from being wasted between the ridges. For this, SU8-2000 polymer was spun on, patterned to the length of the laser ridges, reflowed off

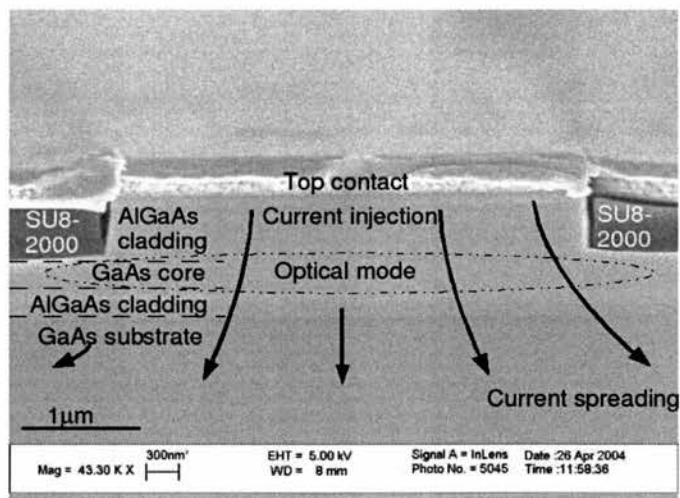


Figure 2.6: SEM image of the cross-section of a quantum well laser. The main features are: the vertical heterostructure that provides vertical waveguiding, and that also contains the optical gain material; the ridge that provides horizontal waveguiding and current confinement; the top contact pad through which current is injected; and the SU8-2000 insulation that directs the current through the ridge.

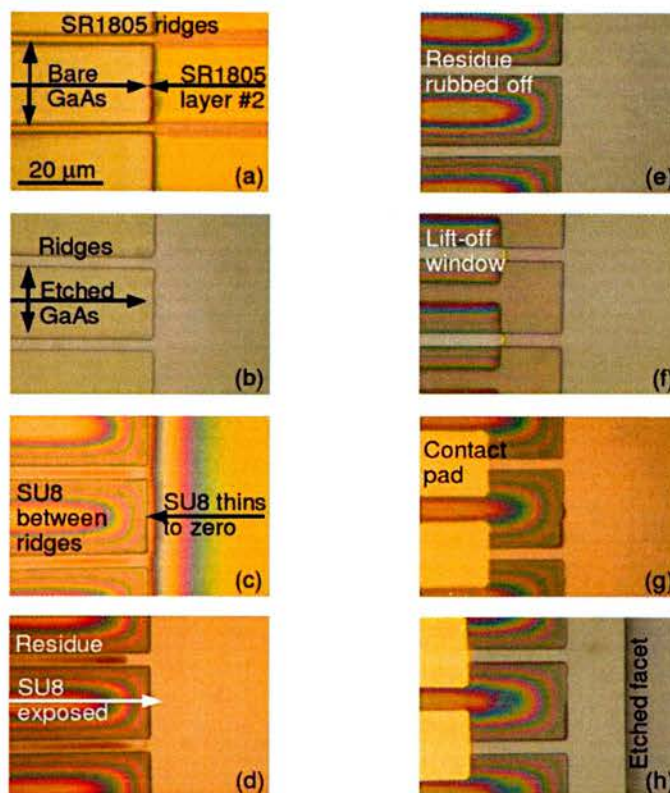


Figure 2.7: Photographs of laser fabrication. These show the ends of two adjacent lasers at different stages in the process: (a) two-stage SR1805 mask defines width and length of ridges; (b) ridges etched in CAIBE and SR1805 removed in SVC-14; (c) SU8-2000.5 applied; (d) SU8-2000.5 patterned to length of ridges; (e) hard-baked and residue wiped off ridges; (f) lift-off mask; (g) top contact pads; (h) facet etched. The period of the ridges is  $20\ \mu\text{m}$ .

the ridges at high temperature, and then hard-baked, and the remaining residue wiped off using an acetone-soaked cotton bud. This left ridges of clean, bare, undamaged GaAs to which, after removing the native oxide layer with HCl, a good electrical contact could be made. A lift-off mask defined windows along the length of each ridge, onto which 20 nm of nickel and at least 150 nm of gold were deposited in an electron beam evaporator, and the unwanted metal was removed by lift-off, leaving only the desired top contacts. After another HCl soak, a back contact was deposited onto the underside of the GaAs; the sandwich (14 nm gold, 14 nm germanium, 14 nm gold, 11 nm nickel and at least 150 nm gold) provided a good Ohmic contact with the GaAs, and had been developed empirically at Glasgow University. The length of the lasers was defined by etched facets; the patterns were transferred into an SR1818 photoresist mask, and etched in the CAIBE machine to a depth of  $\sim 2\ \mu\text{m}$ , using a medium power (14.4W) that was high enough to give speed, whilst low enough to give good quality facets for optimum reflectivity. The depth reached through the heterostructure to give complete reflection of the guided mode. The SR1818 mask was then removed in SVC-14 positive resist stripper; it worked better than did acetone. The hardening effect of the CAIBE bombardment made it difficult to remove, but patient soaking for up to 10 minutes and squirting with a pipette worked, and was preferable to an ultrasonic bath that could damage the electrical contacts.

### 2.3.2 Microfluidics

The photographs in Figure 1.11 show a plan view and a cross section of the microfluidic features, including the channel that was etched between the facing facets, which had to be at least 10  $\mu\text{m}$  deep in order to accommodate biological cells without the risk of adhesion to the base of the channel. Whereas the laser facets had to be vertical and smooth in order to provide a good optical interface, the channel walls serve no optical role and therefore quality of the CAIBE etch was not important, so a faster etch was used. The mask was made in the same way as is a lift-off mask, and is explained later; the SR1818 provided the etch resistance but was hard to remove after a harsh CAIBE etch; the LOR-7B allowed the charred remains to be easily removed. Electrical insulation was provided by coating the base of the channel with a thin layer of SU8-2000 polymer, and the walls with a lithographically-patterned, thicker SU8-2000 blend. The resolution of the lithography created the negative slope (undercut) that is seen in the SU8-2000 wall. This has the effect refracting the laser light upwards, and hence raising the point at which the beams overlap to create the optical trap. This unavoidable effect is advantageous because it keeps trapped particles away from the base of the channel, reducing the risk of adhesion. The adhesion of particles to the channel presumably depended upon the specific chemistry of the situation, and could be reduced as discussed in Section 2.4, but the best approach was to prevent contact between the particles and the channel.

As was seen in Figure 1.13, the device was then mounted onto a circuit board that provided both a rigid structural support for capillaries, and an electrical connection to the back contact. For containing the fluid, a glass chamber was built, and was sealed with wax that also sealed narrow metal or glass capillary tubes into the ends of the chamber. The original method used metal tubes (1 mm OD) whose ends were simply placed on the top of the GaAs chip; a glass box was built around it, but that had a larger wasted volume above the channel, so most of any sample did not pass through the laser beams. The best method used glass capillaries that had been drawn very thin at the end ( $\sim 30 \mu\text{m}$ ) that could be laid directly in the channel. A lid was then placed directly on top of the SU8-2000 channel wall insulation, removing the wasted volume of the older methods, and ensuring that the entirety of any sample passed through the laser beams. Silicone tubes were attached to the capillaries that led to a reservoir and either a peristaltic pump or a simple gravity feed. In order to prevent the device from over heating, which reduced the efficiency of the lasers and melted the wax, adequate heat sinking had to be provided. The metal tracks on the circuit board did not provide that, so the device was connected to a brass mount, via a hole in the circuit board beneath the device.

## 2.4 Complete Fabrication Instructions

With the fabrication overview in mind, the exact recipes that were used to create a device are now presented. The dimensions of the laser cavities are for the quantum dot material, but they are easily adapted for the quantum well material. All exposures were conducted on a Karl Zuss mask aligner with a U.V. lamp whose intensity was measured to be  $3.1 \pm 0.1 \text{ mW cm}^{-2}$  and  $5.3 \pm 0.1 \text{ mW cm}^{-2}$ , at 365 nm and 400 nm, respectively.

### 2.4.1 Preparation and Cleanliness

The GaAs-based material was cleaved into pieces of size  $\sim 6$  mm x  $\sim 6$  mm; this accommodated the length of facing pairs of 2 mm-long lasers. It was important that the entire area remained clean, for dirt of various sorts could interfere with the creation of the long lasers and with the etching of the long channels. This contrasts with many other micro-optic devices that are very small and can therefore be placed inbetween spots of dirt; they also involve fewer steps and so have less opportunity to pick up dirt. These optical trapping devices need a large area of clean material, that must be kept clean from one process to the next. There were three main sources of contamination: dust from the environment, and that created during scribing, cleaving and when the GaAs was chipped; touching with greasy or dirty objects; and evaporation of liquids to leave stains. Each of these would interfere with the processing, either masking regions that should be etched, or preventing the proper adhesion of layers to the GaAs. In all cases, the best approach was prevention rather than treatment.

#### Cleaving

The first step to cleanliness was careful cleaving, which could be a major source of dust and grease. Once the scribe mark had been made, the dust from that operation was removed with a nitrogen blow gun to prevent the dust from scratching, or adhering to, the surface in the next step, the cleave. This was conducted with the GaAs in a clean plastic wallet, with a piece of cleanroom wipe on the upper surface of the GaAs; this protected the GaAs from any contaminants that were on the plastic. The actual cleave was conducted by breaking the GaAs from the scribe over a razor blade; afterwards the GaAs was again blown with nitrogen to remove the new dust. At all times the GaAs material was never touched on the upper surface, but was held by the vertical edges. Immediately after cleaving the samples were cleaned in analar grade acetone in an ultrasonic bath for 3 minutes, then in IPA under the same conditions, and then blow-dried with nitrogen.

#### Mounting

When the samples had to be held directly, the best tweezers to use were plastic-tipped, metal tweezers. The metal provided strength and control, and the plastic did not chip the GaAs as metal would. Whenever possible, the GaAs pieces were mounted on glass cover slips that acted as handles, thus avoiding contact with the GaAs, and hence reducing the chances of damage and contamination. This was done as follows:

Spin PMMA onto a cover slip at at least 3000 rpm for  $\sim 2$  s, until flat but still wet

Place sample on PMMA at middle of cover slip

Place on 60°C hotplate for  $\sim 30$  s, until no longer visibly wet

Place on 100°C hotplate for  $\sim 60$  s to dry PMMA

The two bakes were conducted on one hotplate, but at different positions, so that the sample could be moved between bakes without being lifted off the heat source. A temperature of at least 100°C was required in order to dry the PMMA such that the GaAs adhered securely. However, it was found that when the sample was placed on the hotplate at such a temperature, a film of condensation formed on the

GaAs and then quickly disappeared. It was assumed that this was the result of chlorobenzene evaporating from the PMMA on the glass, then partially saturating the atmospheric vicinity, and thereby condensing on the cooler GaAs before evaporating again when the GaAs heated up to the temperature of the hotplate. If it all evaporated then presumably no trouble would result, but in order to avoid the risk of any solvent remaining on the surface, the 60°C bake was added; it heated the glass coverslip and the GaAs more slowly. The solvent evaporated more slowly than before, allowing it to escape from the vicinity without saturating the atmosphere. Increasing the bake temperature to 100°C then removed the remaining solvent, but there was not enough left to saturate the atmosphere, and the GaAs more quickly reached the temperature of the hotplate, both of which factors prevented condensation on the GaAs. The PMMA was easily removed by soaking in acetone, but that was much more difficult if it had been heated to above ~150°C, and any remaining PMMA would have spoiled the back electrical contact. So, before any such bakes, the samples were removed from their cover slips by gently pushing the edge of the GaAs with a plastic tool (such as the handle of a pair of tweezers), and rubbed over an acetone-soaked cotton bud to remove the PMMA, taking care to avoid any acetone causing damage to the features on the upper side.

### Solvents

In order to avoid the formation of stains on the material, it was important to rinse and dry them properly. Each solvent had to be displaced by another before the first had evaporated. For example, acetone dissolves many stains and polymers, but it evaporates easily, leaving stains behind. IPA displaces acetone and the dissolved material from the surface of the GaAs, and then evaporates only slowly, giving time for it to be blown off (with any dissolved material) from the surface before any natural evaporation can occur. The correct combinations are given in Section 2.2.1.

### CAIBE Processing

Before each CAIBE process, the samples were removed from their cover slips and the backsides were cleaned, taking care not to spoil the polymer masks with acetone. In the CAIBE, samples were held in place on the stage by a heat sink compound (HSC); it is a horribly greasy substance that could only be removed in an ultrasonic bath, but that would damage the contact pads, so it was often not possible. Fortunately, because the pieces of GaAs were so small, only a tiny spot ( $\approx 1 \text{ mm}^2$ ) was necessary. It was removed very carefully immediately after the etch by scraping over the edge of a cover slip, without getting any on the upper surface of the sample. Another approach was to put no HSC on the sample, but to use the HSC to hold little metal plates on the CAIBE stage in a fence arrangement. The sample could then sit within the fence, without moving and without contact with the HSC. The thermal contact must have been good, even without the HSC, because the etch depths were the same as when it was used directly on the samples.

### 2.4.2 Laser Ridges

The direction of propagation of each laser beam was determined by the orientation of the guiding ridge and the facets. In order to ensure that facing lasers were precisely aligned, their ridges had to be defined in the same exposure step; two separate exposures never gave alignment any closer than  $\sim 2 \mu\text{m}$ . Therefore, the facing laser ridges could best be defined by using a mask that had both sets, with a gap in between. However, the desired gap depends upon the application of the device, and so it was unsuitable to make a general mask feature, and insufficient space was available on the photomask to create numerous different versions. Three different methods for creating facing ridges using general mask features are described in detail in Section 2.5, but for now only the successful two-step method is given. The ridges were exposed in a layer of SR1805 resist over the length of the GaAs. Then the lengths of the laser ridges were defined in a second layer of SR1805, allowing the lengths and spacing to be tailored to the application, as seen in Figure 2.8. The recipe is as follows:

Mount on cover slip  
 Spin-coat SR1805 at 5000 rpm for 1 minute  
 Wipe off corner beads using a cotton bud moistened with acetone  
 Bake on  $100^\circ\text{C}$  hotplate for 2 minutes  
 Expose for 9.0 s through mask with  $3 \mu\text{m}$ -wide lines  
 Develop in MF319 for  $20 \pm 2$  s  
 Rinse in de-ionised water for 5 s  
 Blow-dry in dry nitrogen  
 Remove from cover slip and clean underside  
 Bake in  $180^\circ\text{C}$  oven for 1 minute to harden layer.

The above procedure was repeated for a second layer of SR1805 (excluding the  $180^\circ\text{C}$  bake) in which sections were exposed in order to define the lengths of the ridges, as is shown in Figure 2.8. The  $180^\circ\text{C}$  bake hardened the first layer of SR1805 so that it did not develop with the second layer. The length of the

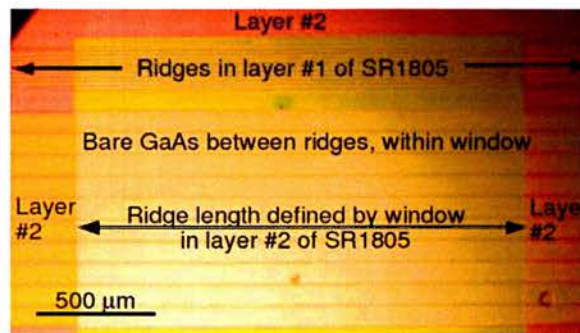


Figure 2.8: Two-layer method for defining ridges in the etch mask. The ridges were created in the first layer of SR1805 that was then hard baked; the length and position of each laser cavity was then defined by opening windows in a second layer of SR1805. The GaAs-based substrate was only uncovered (and hence only etched in the CAIBE) where both layers of SR1805 had been developed, creating ridges of specified lengths.

second exposure feature was chosen to be  $\sim 1800 \mu\text{m}$ , as explained in Chapter 3. The gap between the facing pairs of ridges (note that only one set of lasers is shown in Figure 2.8) was typically  $\sim 100 \mu\text{m}$ , but could be reduced to  $\sim 50 \mu\text{m}$ , so long as sufficient space was left for the addition of the channel and its lining. The  $180^\circ\text{C}$  bake caused the polymer to reflow and spread slightly, but the final result gave ridges that were reliably  $3.2 \pm 0.2 \mu\text{m}$  wide and  $\sim 400 \pm 50 \text{ nm}$  thick.

As will also be explained in Chapter 3, the correct depth of the laser ridges was determined to be around  $750 \text{ nm}$ , and the slower the etch rate, the more accurately the depth could be controlled. The following recipe was found to be suitable, giving vertical walls as seen in Figure 2.6 previously, although the profile was not critical in this application. The profile did not have to be exactly vertical so long as there was a clear contrast between the high refractive index GaAs and the lower refractive index etched region, as described in Chapter 3, and a vertical etch gave the best contrast, confining the mode to a smaller size and giving a higher current density. In common with the other CAIBE recipes to follow, this one is given in a table, in which the important etching parameters are divided into two categories: physical and chemical. Here,  $V_b$  is the beam voltage,  $i_b$  is the beam current and  $T$  is temperature. Argon and chlorine flow rates are given in standard cubic centimetres per minute (sccm).

Physical	Chemical
Ar 10 sccm	$\text{Cl}_2$ 2.5 sccm
$V_b$ $350 \pm 5 \text{ V}$	$T$ $120 \pm 1^\circ\text{C}$
$i_b$ $10.0 \pm 0.5 \text{ mA}$	

The etch selectivity was 3:1 in favour of the resist; that is, the GaAs was etched three times more rapidly than the SR1805. The remaining SR1805 mask was removed by a few minutes in SVC-14 in an ultrasonic bath, rinsed in water, and then cleaned in an ultrasonic bath in fresh acetone, then isopropanol (IPA) and then blow-dried with nitrogen. The SVC-14 was important here because it removed all of the SR1805 from the GaAs, whereas acetone tended to leave little patches that would then gather at the ends of the etched regions, where they could interfere with future processes.

### 2.4.3 Inter-Ridge Insulation

SU8-2000.5 polymer was used for the inter-ridge insulation; being a negative resist it had to be patterned carefully, because the cured polymer could not be removed. The following “reflow and rub” method (or simplified chemical-mechanical polishing) was developed, and is illustrated in Figure 2.7(d) and (e).

Mount on cover slip  
 Spin coat SU8-2000.5 at 5000 rpm for 1 minute  
 Bake on  $60^\circ\text{C}$  hotplate for 4 minutes  
 Bake on  $100^\circ\text{C}$  hotplate for 1 minute  
 Expose for 40.0 s only over etched regions between ridges  
 Bake on  $100^\circ\text{C}$  hotplate for 1 minute  
 Develop in EC solvent for 5 s  
 Rinse in de-ionised water for 5 s

Blow-dry in dry nitrogen  
Remove from cover slip and clean underside  
Bake in 180°C oven for 5 minutes  
Gently wipe with acetone-soaked cotton bud for  $\sim 30$  s, parallel to ridges  
Rinse in acetone  
Rinse in IPA  
Blow-dry in dry nitrogen  
Hard bake in 180°C oven for 5 minutes

The exposure avoided the polymer that lay on the facet regions, leaving them clear; this alignment was made easier by the fact that the polymer thinned to nothing, at a distance of several microns from the etched edges, giving a margin for error in the positioning of the exposure mask. Also, it was important that the SU8-2000.5 was exposed only where the GaAs had been etched to leave the ridges. Any SU8-2000.5 that was exposed on unetched GaAs was vulnerable to the cotton bud and tended to be rubbed off and deposited in little bits elsewhere on the surface, interfering with future processing. It proved to be very stubborn and hard to remove without vigorous rubbing or the ultrasonic bath, both of which risked damaging the desired SU8-2000.5 insulation. Heating above  $\sim 150^\circ\text{C}$  caused the polymer to reflow, leaving the ridges with only a thin, brown residue that was rubbed off using a cotton bud soaked in acetone. This did not affect the polymer because, after causing the polymer to reflow, the 180°C oven bake hard-baked it, making it chemically and physically resilient, even to a cotton bud. The result was a layer whose minimum thickness was  $\sim 400$  nm, rising up to meet the top of each ridge, as seen in the SEM image in Figure 2.6. Even layers as thin as  $\sim 100$  nm were electrically-insulating up to the maximum tested value of 25 V, and they were unaffected by any of the subsequent processing steps or by the operation of the device.

#### 2.4.4 Top Contacts

The top contacts were deposited using an Edwards 360A electron beam evaporator. To define the positions a lift-off mask was created, as outlined in Section 2.2.2, using the following recipe, with 1750  $\mu\text{m}$ -long mask features that fitted within the length of the ridges:

Mount on cover slip  
Spin on LOR-7B at 4000 rpm for 60 s  
Remove from cover slip and clean underside  
Bake in 180°C oven for 5 minutes  
Mount on cover slip  
Spin on SR1805 at 5000 rpm for 60 s  
Bake on 100°C hotplate for 2 minutes  
Expose for 15.0 s through 1750  $\mu\text{m}$ -long windows  
Develop for  $\sim 40$ -50 s until an undercut is visible  
Rinse in de-ionised water  
Blow-dry in nitrogen

Immediately prior to being placed in the evaporator chamber, the sample was soaked in a solution of

~18% hydrochloric acid (a 1:1 mixture of water and 37% HCl) for 60 s, rinsed in water and blow-dried in nitrogen. The acid removed the layer of native oxide that would prevent a good electrical contact, and it was imperative that the sample was put under vacuum within a few minutes of the HCl step, and without being breathed upon after the acid step. Then once the evaporator chamber's pressure was below  $2 \times 10^{-6}$  mB, two layers of metal were deposited: 20 nm of nickel on the GaAs, and then 200 nm of gold on the nickel. The purpose of the gold was to provide a low resistance path through which an electrical current could spread evenly to create an equipotential surface from which the current could uniformly pump the length of the laser ridge. Gold does not adhere well to polymers or to GaAs, but nickel is extremely "sticky", acting like glue that adheres to the GaAs and the SU8, and to which the gold in turn adheres very well. Although its resistivity is higher than that of the gold, the nickel does not affect the spreading of the current through the gold, and the nickel layer is so thin that it has little effect upon resistance of the laser as the current travels downwards from the gold. Having been removed from the evaporator, the sample was left to soak in acetone until the SR1818 had been dissolved and the unwanted metal had floated off. It was rinsed in IPA, then soaked in MF319 to remove the LOR-7B, then in water; to clean it properly, it was then dipped in acetone, then IPA, and finally blow-dried with nitrogen.

#### 2.4.5 Back Contact

This, too, was deposited in an Edwards 360A electron beam evaporator, the sample was treated with HCl as for the top contacts, but no mask was used; the sandwich of materials was applied to the entire underside of the GaAs. The layers were, starting from the GaAs: 14 nm gold, 14 nm germanium, 14 nm gold, 11 nm nickel and at least 150 nm gold. This was developed empirically at Glasgow University and created a good Ohmic contact on the GaAs.

#### 2.4.6 Facets

When used as an etch mask for the facets, SR1818 had to meet two main criteria: it needed to have a straight, smooth edge, and this edge had to remain intact throughout the duration of the 7.5 minute CAIBE etch. Both of these conditions were met by the following recipe, so long as the photomask feature was clean and undamaged. The facets were defined beyond both ends of each laser ridge, whilst leaving enough space in between the facing facets for the channel and the channel coating.

Mount on cover slip

Spin coat SR1818 at 5000 rpm for 1 minute

Wipe off corner beads using an acetone-moistened (but not wet) cotton bud

Bake on 100°C hotplate for 5 minutes

Expose for 23.0 s

Develop in MF319 for ~25 s

Rinse in de-ionised water for 5 s

Blow-dry in nitrogen

This gave an SR1818 layer that was ~1.6  $\mu\text{m}$  thick. In contrast to the ridges which required a specific

depth but just a roughly-vertical profile, the etching of the facets specifically required vertical etches, but the depth was less critical, the only requirement being that it had to be  $> 2 \mu\text{m}$  deep. The profile had to be vertical and smooth so that the laser light would experience the maximum possible reflectivity, which is  $\sim 30\%$  for a perfect GaAs-air interface at normal incidence. The following recipe, etched for 7.5 minutes, removed  $\sim 2.4 \mu\text{m}$  of GaAs, again with an etch selectivity of  $\sim 3:1$ .

Physical	Chemical
Ar 10 sccm	T $120 \pm 1^\circ\text{C}$ rising to $126 \pm 1^\circ\text{C}$
$V_b$ $1200 \pm 5 \text{ V}$	$\text{Cl}_2$ 3.9 sccm
$i_b$ $12.0 \pm 0.5 \text{ mA}$	

The mask was then removed by soaking in SVC-14, and by agitating the solvent by squirting with a pipette; no ultrasonics could be used, for fear of damaging the contact pads. As before it was then rinsed in water, and then soaked in acetone, then IPA and then blow-dried with nitrogen. Here, again, the SVC-14 was better at removing the SR1818; acetone tended to leave fragments that could adhere to the facets, spoiling the laser performance.

### 2.4.7 Channel

The quality of the etch of the channel was not as important as it was for the facets; it needed only to be deep, but that was best achieved by etching at high temperatures, such as  $150^\circ\text{C}$ . Such temperatures, though, hard-bake SR1818, making it very difficult to remove, even with SVC-14, so a lift-off mask was used, which is explained more fully in Section 2.5.

Mount on cover slip  
 Spin on LOR-7B at 4000 rpm for 60 s - repeat three time to cover tops of facets  
 Remove from cover slip and clean underside  
 Bake in  $180^\circ\text{C}$  oven for 5 minutes  
 Mount on cover slip  
 Spin on SR1818 at 5000 rpm for 60 s  
 Bake on  $100^\circ\text{C}$  hotplate for 2 minutes  
 Expose for 25.0 s to give a window between the facing facets  
 Develop for  $\sim 30\text{-}40$  s until LOR-7B has retreated beyond edge of SR1818 feature  
 Rinse in de-ionised water  
 Blow-dry in nitrogen

The following CAIBE recipe was used for two 8 minute etches;  $\sim 13 \mu\text{m}$  of GaAs was etched, adding to the  $\sim 2 \mu\text{m}$ -deep facets to give a  $\sim 15 \mu\text{m}$ -deep channel. The mask was then removed as in Section 2.4.4.

Physical	Chemical
Ar 10 sccm	T $\sim 145^\circ\text{C}$ (rising to $\sim 155^\circ\text{C}$ due to ion bombardment)
$V_b$ $1450 \pm 5 \text{ V}$	$\text{Cl}_2$ 5 sccm
$i_b$ $17.0 \pm 0.5 \text{ mA}$	

### 2.4.8 Channel Lining

SU8-2000.5 was used to coat the base of the channel, as follows:

Mount on cover slip  
Spin coat SU8-2000.5 at 2000 rpm for 1 minute  
Bake on 60°C hotplate for 1 minute  
Bake on 100°C hotplate for 4 minutes  
Expose base of channel for 40.0 s  
Bake on 100°C hotplate for 4 minutes  
Develop in EC solvent for 5 s  
Rinse in IPA for 5 s  
Blow-dry in dry nitrogen  
Remove from cover slip and clean underside  
Hard bake on 150°C hotplate for 5 minutes

Then SU8-2050 was used for lining the walls of the channel, according to the following recipe:

Mount on cover slip  
Spin coat SU8-2050 at 5000 rpm for 1 minute  
Bake on 60°C hotplate for 3 minutes  
Bake on 100°C hotplate for 9 minutes  
Expose walls of channel and ends of lasers for 40.0 s  
Bake on 60°C hotplate for 3 minutes  
Bake on 100°C hotplate for 9 minutes  
Develop in EC solvent for 30 s, squirting if necessary to remove residues  
Rinse in IPA for 5 s  
Blow-dry in dry nitrogen  
Remove from cover slip and clean underside  
Hard bake on 150°C hotplate for 5 minutes

As an additional touch, 20 nm of nickel and 200 nm of gold were added to the base of the channel which served two purposes in the operation of the devices. Firstly, the gold reflected illuminating light back upwards, aiding in the viewing of trapped particles. This was especially important when the ends of the top contacts were in the field of view; the strong reflection tended to saturate the CCD camera, diminishing the contrast of the particles against the polymer background. Secondly, the gold reduced the incidence of adhesion to the base, presumably because the specific chemistry of the situation tended to bond cells and polymer spheres to the SU8-2000 polymer more easily than to gold. The deep channel, however, prevented the use of normal lift-off techniques, so a crude plastic mask was placed around the channel. When it was removed after the evaporation, the excess gold around the channel was removed by gently wiping with a cotton bud soaked in acetone, although that sometimes damaged the gold that was in the channel. The use of nickel beneath the gold would have prevented such damage by improving the adhesion as it did with the top contacts, but the improved adhesion would also have prevented the removal of the unwanted gold around the edges of the channel. Eventually, a lift-off mask was created by building up many layers of

LOR-7B polymer; its creation was unreliable, and it often needed to be repeated before a successful mask was ready for the evaporation step, but it did allow the use of nickel that held the gold more securely in the channel. The microfluidic features that resulted from these steps are shown in Figure 1.11.

### 2.4.9 Chamber and Capillaries

As is seen in Figure 1.13, the dimensions of the chamber were dictated largely by the dimensions of the capillaries. Metal capillaries had a circular cross-section of 1 mm outer diameter, but one end of each was flattened so that they had flat upper and lower surfaces that sat more evenly on the device, with heights of  $\sim 0.4$  mm. The glass capillaries shown in Figure 1.13 also had 1 mm outer diameters, but they tapered to points, and could be trimmed to a length that gave the desired final diameter. The best arrangement used such a glass capillary with 30  $\mu\text{m}$  OD ends that could simply sit within the polymer lining of the channel, allowing a lid to be placed directly on top of the channel. The silicone tubes were attached to the circular ends and the capillaries were held in place on the circuit board with electrical insulation tape or U.V.-cured adhesive.

The chamber was built from tiny sheets of glass that were cut from cover slips, and sealed with dental wax that was softened by placing the entire arrangement on a 60°C hotplate and observing through a x5 microscope. The wax had to be soft enough to be pushed into the gaps with a fine needle, to form a complete seal, and yet not too soft, for then it would have flowed into the microfluidic channel. Removing the arrangement from the hotplate allowed the wax to cool and set hard, but the beauty of the method was that alterations (mainly plugging leaks) could be made by simply heating the wax and adding more. The whole assembly could be removed just by soaking it in trichloroethylene, but this tended to cause the SU8-2000 features to peel up from the device. The SU8-2000 remained intact, and it remained adhered to the material beneath it, but that meant that it tore up contact pads and even pieces of GaAs. These problems were avoided by using PMMA as a sealant, rather than dental wax. PMMA is soluble in acetone, which does not damage the devices, but it is harder to work with, being either too runny or too sticky. An ideal method would be to lithographically pattern an adhesive.

## 2.5 Background and Optimisation

The above fabrication sequence used some established, well-documented techniques that involved commercially available materials. However, other methods were novel, and even the established methods had to be adapted to suit the available equipment and the specific applications. There follow details of the background principles that were important when developing the recipes, with mention of specific examples, as well as discussions of some other methods that were investigated but were found to work less well. Some of the work was done with the original quantum well material, which responded in much the same manner as the quantum dot material to which the afore-mentioned fabrication details apply.

### 2.5.1 Polymer processing

Polymer processing formed the basis of the device fabrication, being used to create masks for etching and deposition, and also for forming permanent electrical insulation. The repeatable production of high quality polymer films was essential if devices were to be fabricated reliably, and that required some or all of the following steps:

Step	All polymers	Photoresists only	Some applications
1	Spin-coat to apply layer		
2			Remove edge beads
3	Bake to dry layer		
4			Surface treatment
5		U.V. exposure	
6			Bake to finalise reaction
7		Develop pattern	
8		Rinse and drying	
9			Bake to harden features

All of these steps affect the final result, and all are interconnected. So, before embarking upon the discussion of each step, it is helpful to put them in context. The spin-coating of a polymer in solution gives a uniform layer, but with beads that mound up around the edges of the sample; these can be removed. Baking removes the remaining solvent to give a hard, consistent layer that responds uniformly to photolithography and etching. Surface treatment at this stage can modify the response to the photolithography. Some polymers can be patterned by means of U.V. light in a mask aligner machine, allowing the selected parts of the polymer to be removed (positive resist) or left intact (negative resist). Good U.V. resolution requires close contact between the patterned mask and the polymer layer, but the edge beads create a separation, spoiling the resolution, so their prior removal is desirable. Some resists (usually negative) require another bake to finalise the photoreaction. Development in a particular solvent removes either the exposed (for positive resists) or unexposed (for negative resists) regions, and leaves the others, realising the pattern in much the same way as photographic development does. Rinsing in another solvent ends the development, and is followed by blow-drying to prevent the staining that can result from natural drying. A final, hotter bake can harden the layer by causing cross-linking between polymer chains for a more resilient result.

Observations of the layers at each stage are possible, provided that the illumination provides no significant U.V. exposure before the development stage; that is, if the brightness of the bulb is reduced. A mask aligner's microscope has no U.V. component, but only a limited magnification; a normal microscope can be used, so long as the intensity of its illumination is reduced. It was found that SR1800 was sensitive even to the low intensity of room light, if left out for an hour or so. Also, although negative resists generally require lower doses than positive resists do (a rare example of creation being easier than destruction), it was found that SU8 was less sensitive to the U.V. components in the room light and the normal microscope.

### Spin-coating

A solution of polymer in solution is dispensed onto the substrate, which is then rotated at high speed (typically 2000-9000 rpm) on a vacuum chuck. If the viscosity of the solution is insufficient to overcome the centrifugal force then some of the solution is flung off; the rapid motion of the solution with respect to the atmosphere also has the effect of increasing the rate of evaporation of the solvent. The combination of these two inter-linked effects leads to an increasingly viscous layer whose thickness tends towards a final, uniform value that is independent of the initial thickness of the layer, as explained in *Meyerhofer (1978)*. In general, the final thickness depends only upon the spin speed, and the general trend is seen later, in the discussion of SU8-2000 processing.

### Discontinuities in Surfaces

However, the uniformity of the layer will be perturbed by any discontinuities on the surface: that is, anything that interferes with the smooth, horizontal surface of the substrate, and includes etched features, deposited layers, and the edge of the substrate, the last of which is illustrated in Figure 2.9. The formation of edge beads affects all samples by separating the lithographic mask from the polymer layer. The necessary resolution for the 3  $\mu\text{m}$ -wide ridges is unobtainable unless the corner beads, the most extreme manifestations, are removed; and the straight, smooth edge that is required for etching the facets is more easily created in the absence of corner beads. Their removal can be accomplished, for positive resists, by exposure and development, but an easier, general method is to simply wipe them off with a cotton bud that has been slightly moistened with acetone whilst the polymer is still wet, before baking.

There are other, specific issues. Once the laser ridges have been etched, the SU8-2000.5 that is added for the inter-ridge insulation builds up at the edges, but does not properly cover the top. This is useful in this case, because the inconsistent layer on the top flows off when its viscosity is reduced by heating, leaving only weak patches of residue that can be easily rubbed off to leave bare GaAs. However, in other cases the discontinuities are unhelpful. Once the facets have been etched, another etch mask must be added for etching the deep channel. As was explained before, this uses a lift-off mask, but a normal layer of LOR-7B would not cover the top of the GaAs edge, and so three layers of LOR-7B are built up, as shown in Figure 2.10. These layers require no baking in between. A layer of SR1818 on top of this conglomeration provides the desired mask. The third example of a discontinuity is seen when lining the channel with

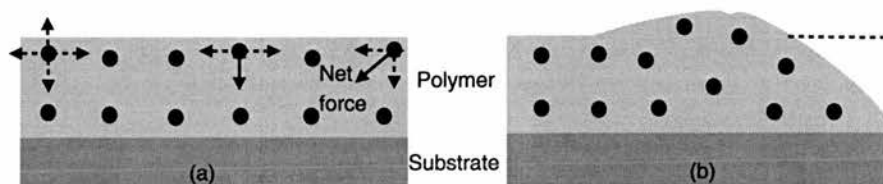


Figure 2.9: Edge bead formation: Edge beads form when (a) the inward-acting intermolecular attractions are imbalanced, drawing polymer in from the edge; (b) this displaces polymer, pushing it upwards to form the edge bead that then separates the polymer layer from the photomask.

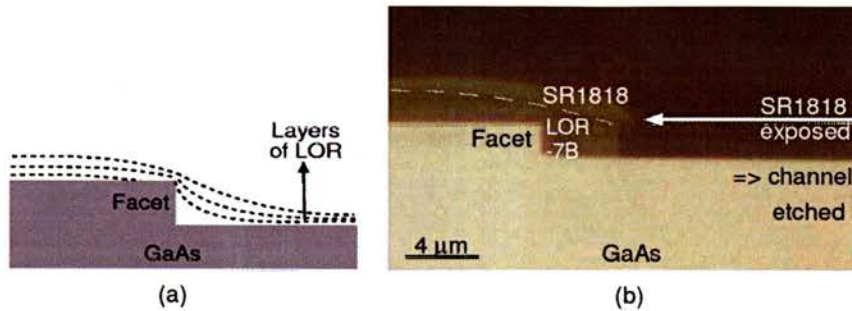


Figure 2.10: Lift-off mask for deep etching: (a) Sketch showing how successive layers of LOR-7B polymer build up to cover the facets; (b) photograph of cross-section of a patterned mask that covers a  $\sim 2 \mu\text{m}$  deep facet. The deep CAIBE etch can be conducted without damaging the facets, and the LOR-7B then comes off easily in MF319, leaving no polymer on the facets, preserving their good optical qualities.

SU8-2000 polymer. The thin SU8-2000.5 layer mounds up against the walls; the risk of completely filling narrow channels is reduced by spinning the layer faster to reduce the thickness at each point, but that then tends to create bald patches on the base of the channel, and so a compromise must be made. Also, the SU8-2000-blend that is used to coat the channel walls must be thick enough to give a planar layer, as illustrated in Figure 2.11. Otherwise, any significant “dip” in the SU8-2000 would mean that the laser light would not emerge from the roughly vertical SU8-2000 edge, but would be reflected downwards from the top surface of the SU8-2000, and would emerge from the SU8-2000 wall low down in the channel. Creating the optical trap there, in close proximity to the base, increases the risk of particle adhesion to said base.

### Bake

This step dries the layer by evaporating the remaining solvent, and the manner of this drying determines the layer’s uniformity and hence its processing performance. For example, non-uniformly dried layers of SR1800 and SU8-2000 give poor lithographic performance with curved or shallow edges that limit the resolution, as will be explained later with reference to Figure 2.13. Also, pockets of solvent prevent the formation of a rigid matrix in SU8, leaving it vulnerable to certain solvents, such as the trichloroethylene that is used to remove unwanted wax from the fluidic chambers. The way to dry a layer uniformly is to use

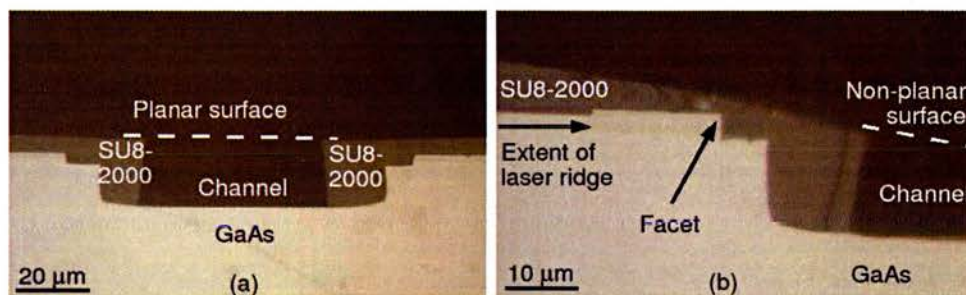


Figure 2.11: Discontinuity due to deep channel. (a) A thick layer of SU8-2000 gives a planar surface; (b) closer view of a feature created in a thin layer that did not give a planar surface.

a hotplate: it maintains a constant temperature beneath the sample that drives the solvent upwards and out into the non-enclosed volume of the ventilated wet-deck, quickly giving a uniformly dry layer. In contrast, the temperature in an oven drops when the door is opened, and the heating acts isotropically, drying the outer surface of the polymer, and tending to drive the remaining solvent inwards, whilst also trapping the evaporated solvent in the enclosed, increasingly saturated, atmosphere of the oven, all of which serves to more slowly create a less uniform layer.

Baking can also make a layer more resistant to the solvents that are in subsequent layers, but not always. For example, layers of SR1818 can be built up, with bakes after each layer, one on top of the other, up to at least six layers, with a total thickness that increases in increments of the thickness of a single layer. However, the solvent in SU8-2000 must be more “potent” in some way, for a pre-exposure bake is insufficient to protect a layer, and a second layer completely strips away the first. At the other extreme, LOR does not even require a bake to make it resistant to the next layer of itself. Similarly, the application of a different polymer can mess up an underlying layer. SR1800 polymer is compatible with LOR, but SU8-2000 will strip away SR1800, and such matters must be taken into account when planning processes.

The photosensitive polymers were baked on a hotplate at 100°C, for higher temperatures would have caused cross-linking that inhibits the photoreactions. Baking SR1805 for 2 minutes and SR1818 for 5 minutes gave good reliability. Thick layers of SU8-2000 were baked for times that depended upon the thickness; the literature recommends an initial bake on a 65°C hotplate to reduce the thermal shock, and this was indeed found to reduce cracking. A 60°C bake was also found to help with the thin layers of SU8-2000.5, preventing the formation of spots in the SU8 film that were seen, above only the etched regions of the GaAs, if the temperature was immediately raised to 100°C. These spots did not seem to cause any problems; the layer was still electrically-insulating and chemically-robust, but the spots caused bumps in the subsequent electrical contacts from which tears could begin, and the samples certainly looked prettier without them. The success of the two-step bake in preventing the spots’ formation confirmed the suspicion that they were formed when the solvent was evaporated too rapidly, either forming and then bursting bubbles of solvent, or crystallising small quantities of polymer. The fact that they formed on the etched GaAs but not elsewhere suggests either that the slightly roughened GaAs provided nucleation sites at which one or other of the two phenomena can occur, or that a role was played by the presence of other elements, such as aluminium, in the deeper layers.

### **Patterning**

As mentioned earlier, the resolution of the lithography was important in the creation of etch masks for both the ridges and the facets; once a uniform layer had been created, the pattern transfer was critical. The photolithography was conducted using the light from a mercury vapour discharge lamp that emitted within the wavelength range 350-450 nm. These short wavelengths have a small associated diffraction-limited spot and hence a higher resolution, whilst the individual photons have high enough energies to induce reactions within the polymers. Patterns were transferred into the polymer from a glass mask, on which features had been written by an electron beam and then etched into a layer of U.V.-opaque ferric oxide.

The processes that occur in negative resists are analogous, but opposite, to those that occur in positive

resists, but positive resists are used here to describe the phenomena. The ease with which a small volume of positive resist is removed by the developer depends upon the volume number density of broken polymer chains, which is proportional to the total dose of U.V. that has been received by the volume. For increasing total doses, the volume is removed more rapidly, and there is a critical dose per unit volume, above which the development occurs easily. Below that critical dose the development will occur, but slowly, and there might be sufficient unbroken chains left to hold the region together, albeit weakly.

Obviously, the polymer at a certain depth can only be developed once the over lying layers have been developed. For an area of the polymer to be removed right down to the substrate, the polymer at every depth must have received at least the critical dose. Figure 2.12 illustrates the ideal case that occurs away from the edges of mask features, in which the total dose received by a volume element is dependent upon both the depth of the element beneath the surface and the length of the exposure. Initially, as the U.V. light propagates through the layer, the intensity decreases exponentially with depth as photons are absorbed to initiate reactions. At normal incidence the GaAs substrate reflects about 25% of the U.V. light back into the polymer, and that then travels back up through the layer, adding to the intensity. So, the intensity at each depth depends upon the absorption coefficient of the polymer, the depth of the layer, and the reflectivity of the interface. But, as time progresses, the intensity distribution changes: each reaction that takes place removes one potential absorber of photons, reducing the absorption coefficient, and hence increasing the intensity at each depth. The time required for each unit volume of polymer to receive its full dose depends upon this ever-changing intensity at that point. The minimum exposure is that which is required for the lowest regions to receive the critical dose, and is called the clearing dose; by that time the upper regions have been over-dosed, but that matters not. In this area of work and in photography, the contrast between exposed and unexposed regions is measured in terms of the gamma function. Essentially this is change in dosed depth per unit exposure, although the definition is slightly more specific. A high gamma function means that a low dose will fully dose a region, making the process faster, but that also makes it easier to

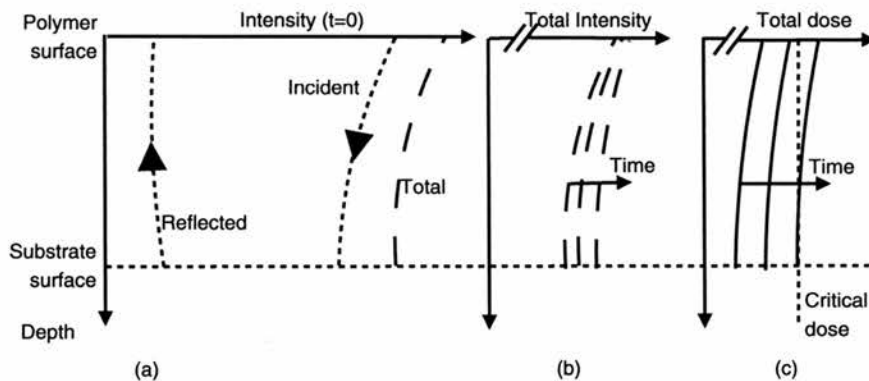


Figure 2.12: Exposure intensity in a polymer layer. (a) The intensity of the light in the polymer decreases as it propagates through the polymer. The total dose received at any depth is the sum of the intensities of the light that travels down into the layer and that which is reflected back from the substrate. (b) The absorption of light reduces the absorption coefficient, so that the intensity at any point actually increases as the exposure time goes on. (c) In order to allow the full development of the layer, each depth must receive a certain critical dose. Fully exposing the lower regions will generally give the upper regions an over-exposure.

dose the surrounding regions, causing the features to spread.

This spreading complicates the situation somewhat. At the edges of the features diffraction occurs, causing the light to diverge and spread out over a larger area than is defined by the mask feature. The horizontal range over which the light can spread is determined by the separation of the mask and the polymer, as shown in Figure 2.13. This separation is normally caused by the edge beads or the corner beads, that can be up to about five and ten times thicker than the layer, respectively. For example, a layer

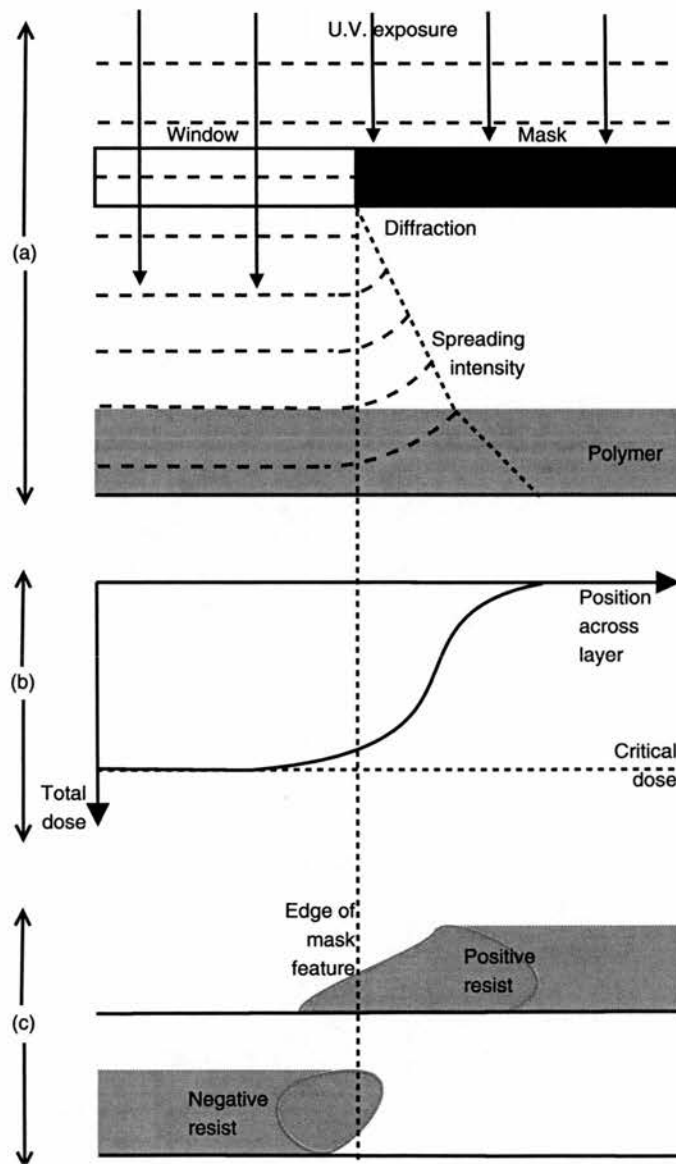


Figure 2.13: Exposure edge effects: (a) The divergence of the light at the edge of mask features causes the light to spread out over the polymer; the range is wider for larger mask to polymer separations; (b) The spreading reduces the intensity at the edges of the mask features; (c) hence, the polymers are not fully exposed to the desired depth.

of SR1805 spin-coated at 500 rpm is 500 nm thick, but its edge beads are  $\sim 1 \mu\text{m}$  thick, and the corner beads are several microns thick. This is why the corner beads are usually removed before the exposure. The spreading has two effects, one within the mask feature and one outwith its area. Firstly, the divergence reduces the intensity of the light at the edges of the features, so that although the exposure time gives a sufficient total dose to remove the total depth of polymer within the main area of the feature, the dose received near to the edges is insufficient. Therefore, the lower regions do not receive the critical dose, and so do not develop. Secondly, the spreading light exposes polymer outwith the mask feature, and, in addition, light reflects from the substrate at non-normal incidence, travelling along the polymer layer, and thus adding to the partial exposure of the regions outwith the mask feature. Again, only the upper regions receive a sufficient dose to dissolve in the developer, leaving the lower regions intact. The resulting profile is sloped, and the widths of the features are different to those on the mask, limiting the resolution: the features tend to be narrower, but the edges of the polymer are thin and might not provide sufficient etch resistance in future processing steps. The ideal case (of perfect contact between the mask and the polymer to give vertical polymer walls whose positions exactly match those of the mask features) can be achieved if the edge beads are completely removed and all of the relevant surfaces in the mask aligner are perfectly parallel. Deviation from this ideal is mainly due the edge beads preventing close contact. For moderate results, it generally suffices to remove just the corner beads, which are the highest. This spreading of a feature to give a sloped edge is the cause of the angled edges seen on the SU8-2000 lining of the trapping channel, as seen in Figure 2.11. Of course, in the case of SU8-2000, a negative polymer, the spreading intensity doses the upper regions of the layer, but the lower regions are not fully dosed and so are developed away, leaving the undercut. The angle is typically  $\sim 10^\circ$  for these thick layers.

Also, if the polymer coats an undulating surface, then the polymer's surface can undulate as well, depending upon the polymer layer's thickness. Any dips will separate the mask from the surface, degrading the resolution, which is particularly apparent when applying the SU8-2000 insulation to the walls of the deep channel. If the resolution is too poor, then the intensity can spread far enough to expose the SU8 throughout the the channel, especially because the thinner layer of SU8 around the channel requires a lower dose anyway. So, the SU8 layer must be thick enough to stay in close contact with the mask, even over the channel, adding to the case that was presented in Figure 2.11.

This limitation on the resolution was most problematic when creating the  $3 \mu\text{m}$  wide ridges in SR1805. There is an overlap between the spreading intensity distributions from each side of the mask's feature. If the mask and the polymer layer were in close contact, then an exposure time of 9.0 s cleared the layer on each side and left a ridge that was  $3.0 \pm 0.5 \mu\text{m}$  wide and  $\sim 300 \text{ nm}$  thick. If the exposure was even 0.5 s shorter the layer was not cleared on each side, and if it was even 0.5 s longer the overlapping intensity distributions reduced the thickness of the ridge, making it less likely to withstand the CAIBE process, and sometimes even creating holes down the centre of the polymer ridge that offered no etch resistance whatsoever. This accuracy could only be consistently achieved when the corner beads had been removed, as discussed above, otherwise the forced separation of the mask and the polymer layer allowed the spreading intensities from the two sides of the ridges to overlap, having the same effect as an over-exposure.

Once the bake time has been optimised to give straight slopes, and the exposure times have been optimised to give the correct feature sizes, the correct development time should be easily determined by trial and error. Negative resists, once sufficiently exposed, can be developed for longer periods of time, and

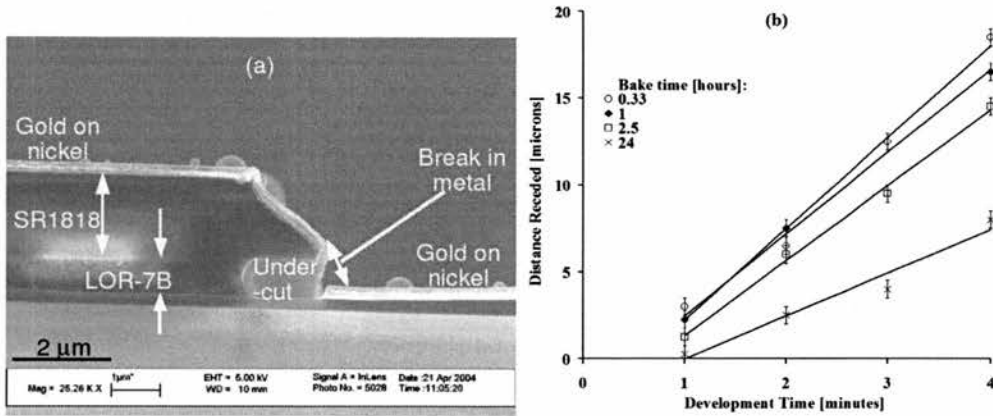


Figure 2.14: Rate at which LOR-7B recedes in lift-off mask: (a) SEM image showing receded edge of LOR beneath SR1818 feature; (b) distance receded by LOR (spun at 4000 rpm) for different bake conditions and development times. The size of the undercut can be carefully tuned if the development rate is slow enough, and that can be accomplished by increasing the bake time.

the exposed regions will remain intact. The unexposed regions of positive resists will eventually begin to dissolve, so excess development should be avoided. Development time is important in the creation of LOR lift-off masks. As already mentioned, the LOR is photo-insensitive, and dissolves in the MF319 developer; so, once the SR1800 has been developed, the LOR is removed to give an undercut. The bigger the undercut, the more easily the acetone can access the SR1800 and the faster the lift-off occurs, but if the lift-off features are very close to one another, the undercut has to be carefully tuned, otherwise all of the LOR is removed and the SR1800 collapses, ruining the mask. The longer the duration and the higher the temperature of the bake, the more slowly the LOR dissolves, giving greater resolution. Figure 2.14 shows the effect of the length of a 180°C oven bake upon the distance receded by the undercut with development time. Apparently, higher bake temperatures, or simply using a hotplate rather than an oven, have a larger effect, slowing the development rate after short bakes.

### Hard Bake

Once the pattern has been developed, it can be helpful to bake the polymer at a higher temperature to harden the polymer, making it physically stronger and chemically more robust. In a positive resist the unexposed molecules cross-link with one another, creating a strong matrix; in a negative resist the photo-induced cross-linking is reinforced; and in both cases remaining solvent can be removed. For both SR1800 and SU8-2000 a 180°C oven bake provides rapid cross-linking: it was used in the two-step definition of the SR1805 ridge waveguide masks, and was originally used in the creation of strong SU8-2000 masks for the deepest CAIBE etching. This can cause the polymers to temporarily soften, giving them the opportunity to reflow, which is used in the SU8 insulation step, and also widens the SR1805 ridges a little. Usefully, it often fills in the holes that are created in the middle of the SR1805 ridge when the lithographic resolution is poor.

### 2.5.2 Chemically-Assisted Ion Beam Etching (CAIBE)

#### Basic Process

The basic process was discussed in Section 2.2, but it is useful to now consider some of the more subtle effects. One of the main issues is the growth of grass, little pillars of product chemicals that re-adsorb to the surface. As illustrated in Figure 2.15, depending upon the exact circumstances of the collisions, the ion impacts eject atoms, singly or in groups, with a range of kinetic energies, and only the most energetic can escape without being re-adsorbed onto the surface. The others can only escape if they react with chlorine molecules that have sufficient kinetic energy to both initiate the reaction and to endow the product

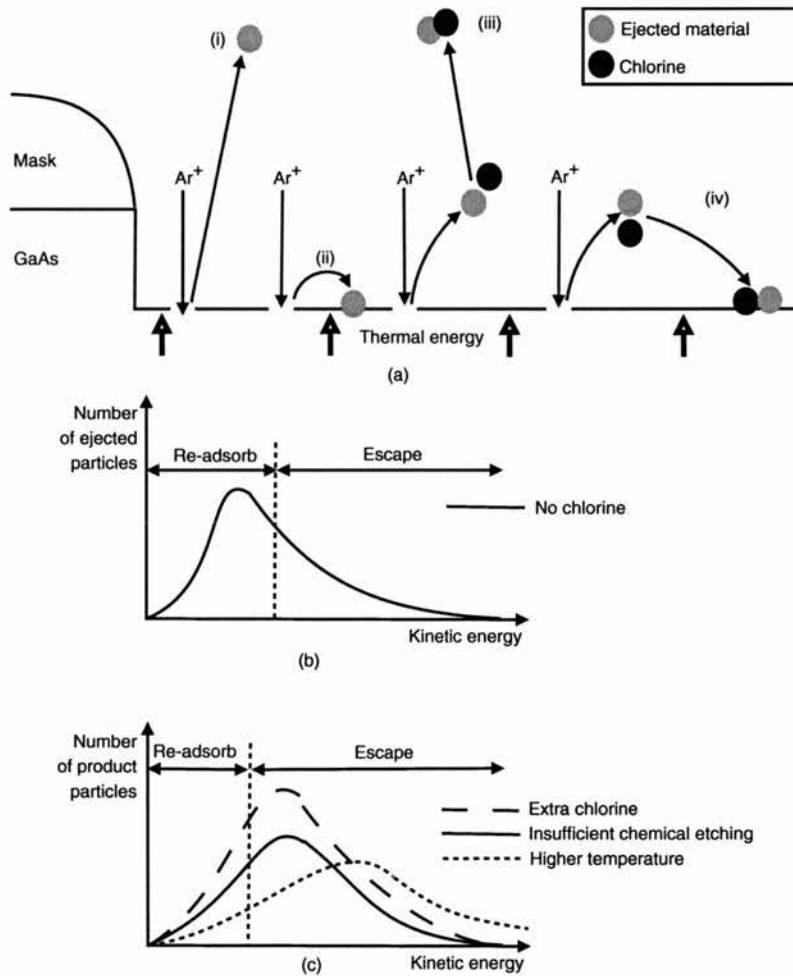


Figure 2.15: Considerations in CAIBE processing. (a) There are four possible fates of ejected material: (i) ejected away from the surface, (ii) re-adsorbed, (iii) reacts with chlorine and is carried away, and (iv) reacts with chlorine, but then the product re-adsorbs. (b,c) Illustrative plots of the distributions of kinetic energy of ejected particles in the processes. (b) Excess chlorine increases the number of undesirable, low-energy products that form grass; (c) excess thermal energy reduces that effect, giving “cleaner” etching.

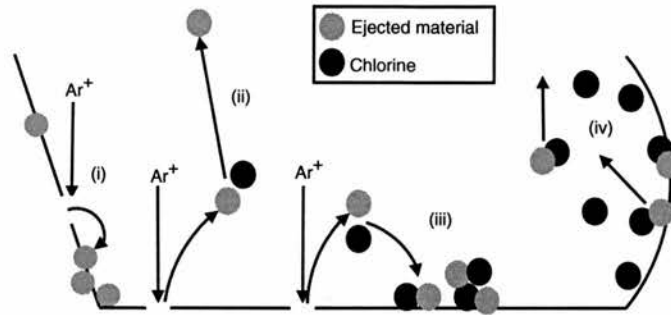


Figure 2.16: Non-vertical etch profiles. Sketch of processes that occur when etch parameters are imbalanced: (i) insufficient chemical etching cannot removed ejected particles quickly enough, so they re-adhere, giving a positive slope; (ii) correct etching provides sufficient chemistry to remove all of the ejected material, giving a vertical profile; (iii) excess chlorine introduces excess low-energy chlorine that create grass; (iv) excess thermal energy etches isotropically, giving a negative profile.

particle with the required escape energy. If the physical component is dominant, producing more ejected material than can be “mopped up” by the chlorine, then either the chlorine flow or the temperature can be increased to compensate. Increasing the chlorine flow introduces more high-energy chlorine molecules to the surface, but not always enough to deal with all of the ejected material, leaving some atoms available for the low-energy chlorine molecules, whose products cannot escape and instead form grass. Increasing the temperature, though, shifts the population distribution, increasing only the high-energy population while actually decreasing the low-energy population, and so actively preventing the formation of grass.

If the physical and chemical components balance one another, then the etched profile is vertical, whereas an excess of either component gives V-shaped and bulbous profiles, respectively, as illustrated in Figure 2.16. An excess of the physical component ejects more atoms than can be taken away by the chlorine, and the effect is greatest at the edge where the larger surface area offers both more readsorption sites and a greater frictional force that slows the impinging argon ions, reducing their kinetic energies, and hence the energies of all of the subsequent interactions. This reduction of the etch rate at the edges gives a V-shaped etch. An excess of the chemical component has one of two effects, depending upon its cause. If it is due to excess chlorine, then the excess low-energy chlorine busies itself by growing grass that inhibits the etch. If it is due to a higher temperature, then that gives the chlorine so much energy that it is able to react with material that is still attached to the surface, without having to first wait for the ions to dislodge it; it etches isotropically into the walls to give a bulbous profile.

### Consistency

The profile of the ion beam flux across the beam is roughly Gaussian, giving a variation in the physical component across the stage. In addition, the chlorine distribution and the temperature might vary across the stage, but this was not easily investigated. What was easily investigated was the variation of the overall etching effect. It was found that, over an area of  $\sim 1$  cm  $\times$   $\sim 1$  cm at the centre of the stage, the rate varied by no more than  $\pm 5\%$ , as measured by the Dektak<sup>3</sup> surface profiler that was introduced in Section 2.3. A sample measured  $\sim 6$  mm  $\times$   $\sim 6$  mm, so it was possible to achieve good uniformity across all of the

etched features. The difficulty came when trying to obtain repeatable results on a number of samples. The Ion Beam Source (IBS) controller could be programmed to give certain conditions, but some of the values fluctuated. The beam current in particular tended to vary by  $\pm 0.5$  mA throughout the course of an etch, but the weighted average was roughly the same for each etch. The temperature of the stage also varied; in the absence of heat sources it would drop due to Newton cooling, whilst the impacts of the ions imparted thermal energy to the stage. Generally, when etching around  $120^{\circ}\text{C}$ , thermal equilibrium was maintained if the beam power was  $\sim 3\text{-}4$  W.

The temperature display gave readings to the nearest  $1^{\circ}\text{C}$ . During deep etches the temperature varied by several degrees Celcius, so the uncertainty in the reading was less significant. But the uncertainty was an issue when etching the ridges, because the etch temperature varied by no more than  $\pm 1^{\circ}\text{C}$ . There was, therefore, no way of monitoring the temperature accurately, which would matter if the etch rate varied significantly over that temperature range. Fortunately, the data in Figure 2.17 (a) show that the etch rate varied only a little over the temperature range  $115 - 125^{\circ}\text{C}$ ; the  $\pm 1^{\circ}\text{C}$  range would have an even smaller effect and was therefore unimportant. That said, it was good practice to be consistent, and so the etches were begun at the moment when the displayed temperature fell from  $121^{\circ}\text{C}$  to  $120^{\circ}\text{C}$ . Using these conditions, a variety of etch times was tested, and the results are shown in Figure 2.17 (b). There is a clear linear relationship around the depth of interest. Incidentally, extrapolation back to shorter times suggests that there is a lag at the beginning of each etch. This is probably due to a surface layer of native oxide, which would have a different etch reponse. In a recent modification to the CAIBE machine, a shutter was added that allows the sample to be shielded for the first few seconds of the etch while the IBS settles down. The etch times were virtually the same after this modification, confirming that the lag in Figure 2.17 (b) is indeed due to the surface and not due to the ion gun.

Whilst etching the facets, the temperature increased by  $\sim 6^{\circ}\text{C}$ , so the exact starting value was less important than it was for the ridges. By contrast, the profile was important for the facets. It was not affected

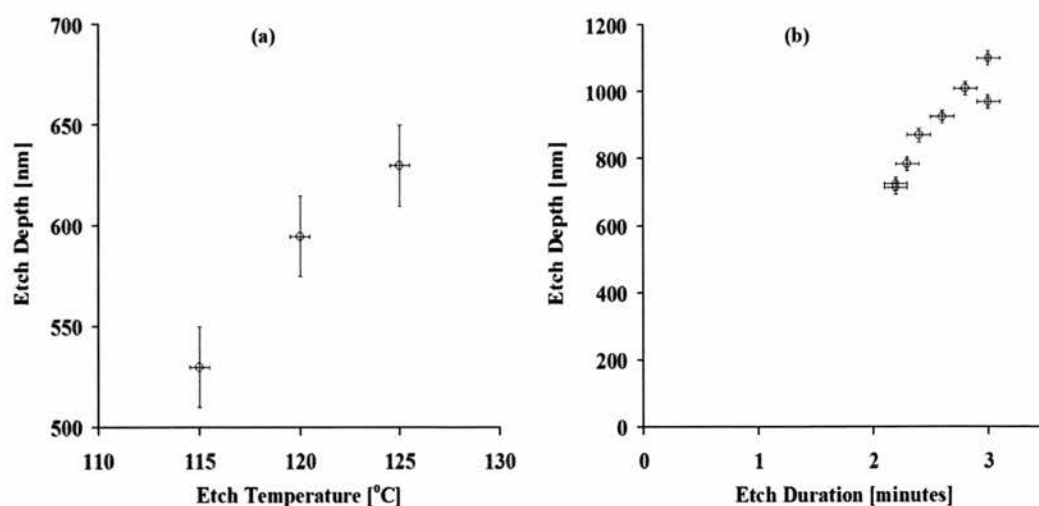


Figure 2.17: Etch data for laser ridges: (a) Etch depth after 2.0 minutes at different temperatures; (b) Etch depth vs etch time at  $120 \pm 1^{\circ}\text{C}$ .

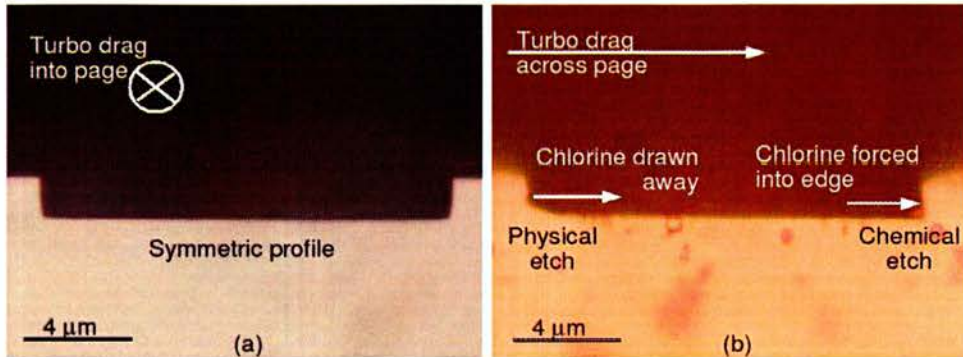


Figure 2.18: Effects of turbo drag upon etch profiles. Etch profiles of  $\sim 2 \mu\text{m}$  deep facets in GaAs-based heterostructure resulting from different orientations of the sample with respect to the gas flow into the turbo pump: (a) facets parallel to the turbo drag have the same profiles; (b) facets perpendicular to the turbo drag have unequal profiles.

noticeably by the temperature range, but it was affected by the orientation of the features with respect to the CAIBE's turbo pump. As illustrated in Figure 2.18, if the facets were aligned towards the turbo (so that the gases were dragged along the lines of the facets), then the facets etched equally. If, however, the facets were aligned at right angles to the turbo drag (so that the turbo pump dragged the chlorine across the facets at right angles), then the concentration of chlorine gas was reduced where it was sucked away, giving a physical etch; and it was increased on the opposite side, giving a chemical etch. Both such profiles gave poor optical performance.

Incidentally, there were no discernable differences between the performances of lasers that had two cleaved facets, two etched facets, or one of each, suggesting that this recipe does indeed produce etched facets that are as vertical and smooth as the cleaved facets. This is highly advantageous, because etching

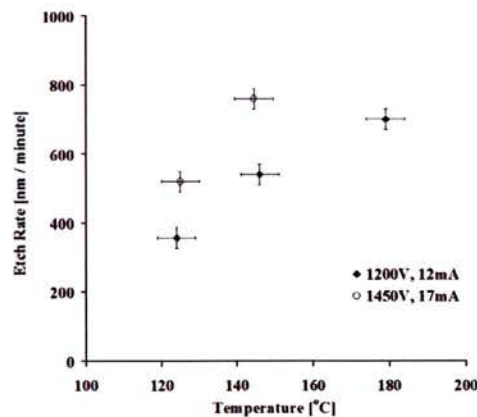


Figure 2.19: Etch rates of GaAs under two sets of beam conditions. These rates are simply the etch depths divided by the etch time; this is not entirely accurate due to the lag seen in Figure 2.17, and the fact that the rate is faster in the upper, epitaxially-grown layers than it is in the harder substrate. In each case, the argon and chlorine flows were 10 sccm and 2.5 sccm, respectively.

both facets on each laser allows them to be kept away from the edge of the device where they would be vulnerable during future processing, and it avoids the risks associated with cleaving: namely, poor cleaves that reflect badly, and smashing a sample into glitter.

The etching of the channel had even fewer stipulations, requiring to satisfy only the single criterion of depth, at least  $10\ \mu\text{m}$  thereof. This was etched fairly quickly in order to limit the degradation of the gun; long etches cause heating that thins the current-carrying wires, and the same effect is caused by multiple short etches, each of which exposes the wires to changes of current. As a compromise, it was desirable to etch deeply in two moderately long etches, and that required a fast etching process. To this end, various different etching conditions were investigated, and the results are shown in Figure 2.19. All of the etches had bulbous profiles, because the ion gun could not reliably supply high enough beam powers to balance the chemical components.

## 2.6 Superceded Methods

This penultimate Section gives a brief overview of some methods that were investigated, only to be replaced in order to make the processing either easier or more reliable.

### 2.6.1 Definition of Ridges and Facets

As was mentioned earlier, there were different ways of defining the positions of the laser ridges. Originally, the ridges were defined right across the samples by using a long set of ridges on a photomask. This gave freedom to position the contact pads and channel at any points along the ridges, but it gave unreliable lasers. Indeed, the SEM image in Figure 2.20 shows the poor facets that resulted from etching the facet straight through the ridges. The “step” in the facet was caused by the SR1818 layer thinning as it covered over the ridges; the exposure time required for the thicker layer between the ridges was too high for the thinner layer, which was therefore over exposed, expanding the region that could be developed to a distance further

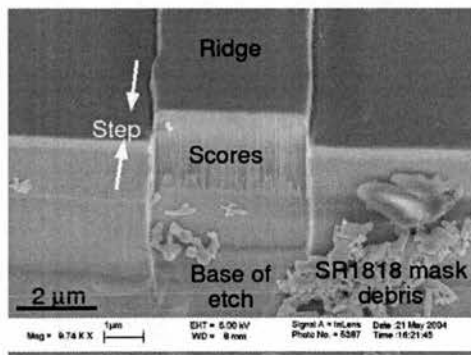


Figure 2.20: SEM image of poor quality facet. Etching the facet straight through the ridge resulted in a stepped profile and deep scores in the facet.

along the ridge. Presumably the “stepped” facet reflected the central and outer portions of the laser mode differently, spoiling the performance. This will also have been affected by the scoring on the facet, which presumably came about because the thinner SR1818 lasted for less time in the CAIBE, allowing ions to break through the edge of the polymer and damage the facet. This is why the process was changed so that the lengths of the ridges were defined to begin with; the facets could then be etched beyond the ends of the ridges, avoiding these problems. And, indeed, the lasers then became much more reliable.

It was then necessary to choose between two options, which are illustrated in Figure 2.21: should the region into which the facets are to be etched be left untouched beforehand, or etched along with the regions between the ridges? The second option was easier because the masks had 10 mm-long sets of ridges that could be split into two facing sets of  $\sim 1.8$  mm-long ridges by simply conducting additional exposures of suitable widths, at right angles to the ridges in the same layer of SR1805. That uncovered the facet regions so that they were etched to the depth of the ridges, which had the advantage of creating a simple mode filter because only the zero-order mode would be reflected at normal incidence and return along the ridge. But at a later point in the fabrication some sort of residue formed that manifested itself as a black scum

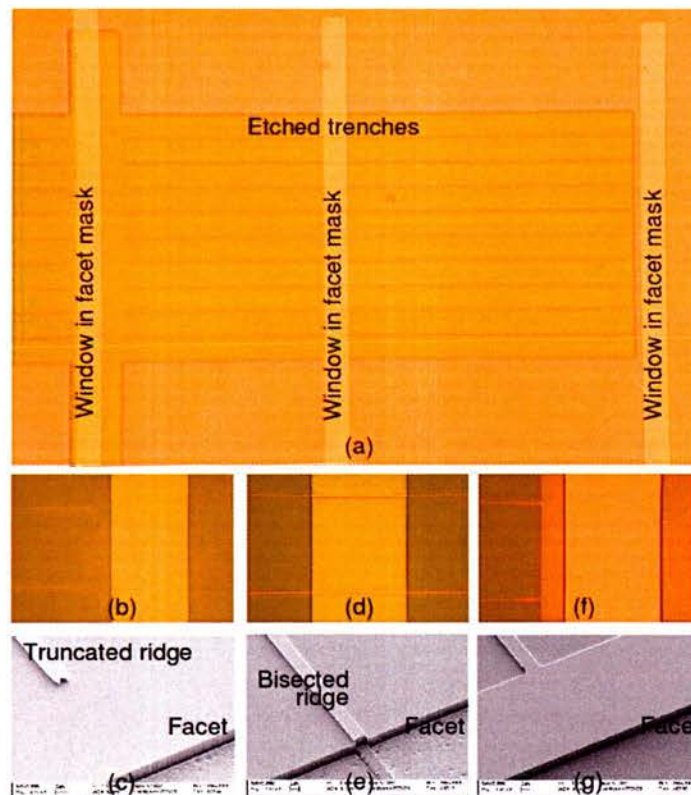


Figure 2.21: Three configurations of facets and ridges. (a) A photograph in which the ridges have already been defined using an SR1805 mask and a CAIBE process; the SR1818 mask has then been added. Photographs (b), (d) and (f) are close-up views of each configuration; (c), (e) and (g) are SEM images taken after the CAIBE etch. (b,c) Ridge truncated in a single-layer SR1805 mask; (d,e) facet etched through ridge; (f,g) ridge defined by two-layer SR1805 mask.

after exposure, which meant that it appeared in the SR1818 facet mask exactly where the etching should have occurred. When etched in the CAIBE, the scum gave horrible, shallow results that had to be avoided. It must have been due to the reaction of some polymer or solvent within the lower regions of the GaAs substrate, perhaps with elements such as aluminum or with traces of chlorine compounds. This hypothesis was supported by the fact that no such residue appeared when the facet mask was created on unetched GaAs. The scum was not seen in the samples that feature in Figure 2.21 because they were simple demonstration pieces on which only the two etches were conducted; no other processing occurred, offering less opportunity for the contamination to occur.

Rather than design a new optical mask it was decided to investigate another approach. After some investigation, including the discovery that soaking developed SR1805 in chlorobenzene does not make it resistant to subsequent U.V. exposure and development, the two layer method detailed earlier was perfected. This allowed the method in Figure 2.21(f) and (g) to be used, and the resulting devices were reliable.

### 2.6.2 Arrangement of Inter-Ridge Insulation and Facets

The SU8-2000 polymer that was used for insulation between the ridges also used to be exposed over the entire area of the sample. This removed the need for any mask alignment, but meant that the SU8-2000 had to be removed from those areas where the facets were to be etched, as defined by an SR1818 mask. Otherwise the SU8-2000 would protect the GaAs from the CAIBE process. The SU8-2000 could only be removed by an oxygen plasma etch in the Reactive Ion Etcher (RIE). This, however, also etched the SR1818 facet mask, reducing its thickness and sometimes damaging its edges, both of which made it less suitable as a CAIBE mask, so, generally, the SR1818 was removed in acetone after the RIE step, and a new SR1818 mask was created for the CAIBE step. However, this extra work could be avoided, along with the risks associated with using yet another machine, by accurately patterning the SU8-2000 in the first place so that it did not cover the facet region.

### 2.6.3 Patterning Inter-Ridge Insulation

This leads to the next issue, which was actually the thorniest of all: namely, how the SU8 polymer should be patterned in order to cover the GaAs between the ridges whilst leaving the ridges themselves clear and clean. All of the methods, bar the last one, were developed using the quantum well material that was used for the first two years of the project.

The generally accepted method was “etch-back”, in which the ridges were covered with a layer of SU8-2000 that was thick enough to be almost planar. It was then etched in the RIE and, as is shown in Figure 2.22, by the time the ridges had been cleared, there would still have been SU8-2000 between the ridges. There were two problems. Firstly, the SU8-2000 tended to etch non-uniformly, either because of unexplained variations in the RIE’s operation, or due to variations in the composition of the SU8-2000 layer. The latter was investigated to some extent, but changing the exposures, bakes and etch conditions did not improve the results. The second problem was that the electrical, and hence optical, performances of the lasers were inconsistent, and usually poor. The reason for this stemmed from the fact that, upon

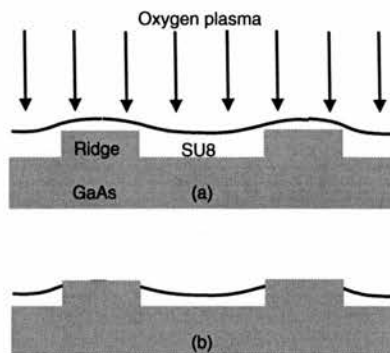


Figure 2.22: Etch-back method for defining inter-ridge insulation: (a) SU8-2000 is etched in an oxygen plasma; (b) the ridges are revealed, but SU8-2000 remains in between. The slower the etch rate, the less damage would occur to the GaAs; rates of 40 nm per minute were possible.

breaking through the SU8-2000, the oxygen will have affected the GaAs surface. The oxygen will have reacted with the GaAs to add to the native oxide layer, but the HCl soak prior to the evaporation of the top contacts should have removed all such material, both native and “RIE-induced”. But the physical impacts of the accelerated oxygen ions will have caused damage to the surface, damage that would not be fixed by the HCl, and so the electrical contact between the GaAs and the nickel will have been poor. As a result, the electrical resistance will have been high, and some regions of the ridge might have been completely insulated from the current, giving non-uniform pumping, and hence poor optical performance. If, in order to limit this damaging etching, the etch time was curtailed, patches of SU8-2000 would be left on the ridges and then trapped beneath the top contacts. When current passed through, it tended to vaporise the polymer, tearing the contacts, and sometimes leaving a crater in the GaAs. Clearly a better method was required.

The most obvious method was to align a mask of narrow ridges over the laser ridges, and to expose a thin layer of SU8-2000 on each side of the ridges. With the mask aligner’s resolution of  $\sim 2 \mu\text{m}$  it was virtually impossible to align  $3 \mu\text{m}$  wide mask features with  $3 \mu\text{m}$ -wide ridges, and the exposed SU8-2000 tended to cover at least part of the ridges. Using a wider mask feature kept the SU8-2000 away from the ridges, and increasing the exposure time moved the edges of the SU8-2000 closer to the ridges, but still the resolution was not good enough to allow consistent success, and the method was time-consuming and tiring.

Next, a method was attempted that started by depositing 20 nm of nickel and 200 nm of gold in narrow ridges, and using them as etch masks for the CAIBE process, in which the selectivity was  $\sim 5:1$  in favour of the gold, so some gold was left afterwards. It was important that some gold remained on top of the nickel, because nickel oxidises in air to give an insulating layer. It was hoped that the gold, being unreactive, would be unaffected by an RIE oxygen etch, allowing the etch-back method to be used. Unfortunately, an unforeseen issue scuppered this plan. As seen in Figure 2.23, the CAIBE process resulted in a series of unetched mesas in lines on each side of the ridges. They would stick through any layer of insulation, wasting current, and were therefore undesirable. They could have been due to material being sputtered by the ion impacts onto the GaAs to create little masked regions, but that would probably have given a more random distribution. In fact, it was noticed that the lines corresponded to the positions of the undercut on

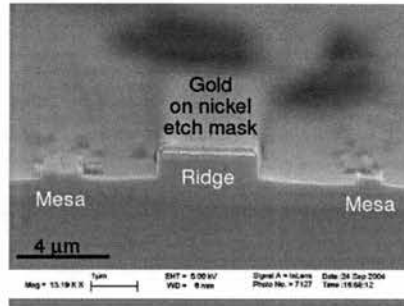


Figure 2.23: SEM image of mesas in cross section. These features resulted from using a gold ridge as an etch mask, and corresponded to the positions of undercuts in the lift-off masks.

the lift-off mask (see Figure 2.14) that had been used to define the metal ridges in the first place. Possibly, some residue from the LOR remained on the GaAs, but no cleaning method was successful in preventing the problem, so it was more likely to have been the case that some reaction occurred, toughening up the surface of the GaAs. Reducing the undercut of the lift off masks moved the lines of mesas right up to the edges of the ridges, but that gave the ridges a roughness that could affect the mode guiding.

Next, a method was developed in which the SR1805 mask was left on after the CAIBE process, and baked in a 180°C oven for 60 s. This hardened the surface enough to make it resistant to the solvent in SU8-2000, so that a layer of SU8-2000 could be applied without it removing the SR1805. The SU8-2000 was exposed along the length of the ridges, both between the ridges and over them, and then hard-baked in the 180°C oven for 5 minutes. This strengthened the inter-ridge SU8-2000 sufficiently to allow it to withstand the next step, which was to wipe the sample, parallel to the ridges, with an acetone-soaked cotton bud. This took the SR1805 off the ridges, along with any SU8-2000 that was on top of the SR1805, leaving the ridges clear and undamaged. It was noticed that the 180°C oven bake reduced the amount of SU8-2000 on top of the SR1805, but the significance was not appreciated until later. The one problem with this “tear-off” method was that some of the SU8 2000 that had previously been resting on the edges of the SR1805 was left sticking upwards or lying on the surface of the ridges, as is seen in Figure 2.24. This created undulations in the top contacts that increased their resistivities, and sometimes actually severed parts of the contacts.

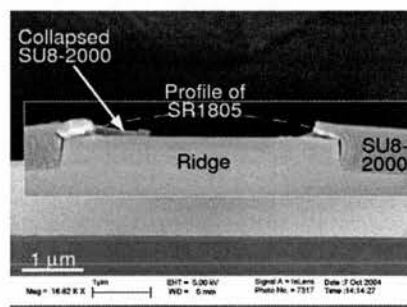


Figure 2.24: SEM image of “tear-off” method in cross-section. Rubbing of the SR1805 etch mask left the SU8-2000 sticking up at the edges of the ridges, and partially covering the top surface.

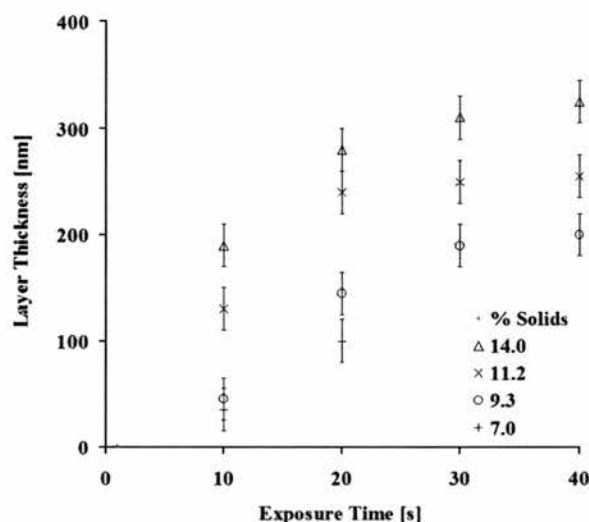


Figure 2.25: Thicknesses of diluted SU8-2000.5 for different exposure times; SU8-2000.5 has a concentration of 14% solids, by weight.

In order to reduce the heights of these undulations, the thickness of the SU8-2000 was tuned so that it only just reached the top of the GaAs ridges, leaving less resting on the SR1805. Increasing the spin speed from 5000 rpm to 9000 rpm did not help enough, so the SU8-2000.5 was then diluted using its solvent (cyclopentanone), from its initial concentration of 14% solids. Figure 2.25 shows the thicknesses of different dilutions that were spun at 5000 rpm, with the interesting addition that longer exposure times gave thicker layers. This method worked reasonably well, but then the quantum dot material replaced the quantum well material, and it was found that the thin layers of SU8-2000 did not coat the etched GaAs uniformly, tending to leave bald patches between the ridges. In despair, the etch-back method was about to be re-visited, and a sample was prepared with a thin layer of SU8-2000 that was heated in the 180°C oven. It was noticed that the heating caused the same reflow as had been seen on the SR1805, leaving only a few spots of brown residue in the ridges. It had always been assumed that what had allowed the ridges to come out clean from the tear-off method was the SR1805 keeping the SU8-2000 off the GaAs, but out of interest, this sample was rubbed with an acetone-soaked cotton bud. And, lo! the SU8-2000 residue came off, leaving the GaAs ridges completely clear. Lasers made in this manner worked extremely well, and with great consistency both across individual samples and between batches. This successful method was discovered by a rather circuitous route, and with hindsight could have been deduced much more quickly, but at least some interesting things were noticed along the way.

#### 2.6.4 SU8-2000 Polymer Processing

Originally, the use of SU8-2000 was more widespread in the fabrication of devices. For instance, it was used as an etch mask for the channel before the lift-off mask had been considered. A hard-baked layer was very strong, surviving in the CAIBE with a selectivity of  $\sim 15:1$  with respect to GaAs. The upper surface of the SU8-2000 emerged discoloured from the CAIBE, but the underside was shielded from the

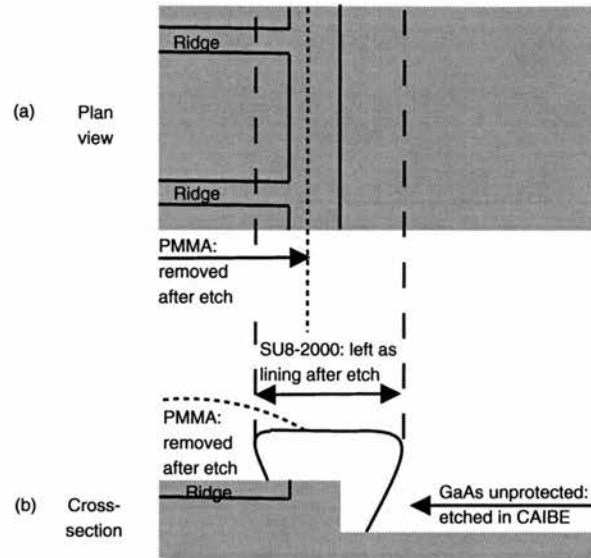


Figure 2.26: SU8-2000/PMMA mask for etching channel: (a) plan view; (b) cross-section. This method was unreliable because the PMMA was applied by hand, often making a mess. It was superseded by the lift-off mask of Section 2.4

worst of the etching. It was hoped that it remained optically clear, for it could not be removed and therefore remained in place over the facets; certainly enough laser power was transmitted to allow optical trapping. This SU8-2000 was required only around the channel; the other facets required neither an etched channel nor electrical insulation. To this end a temporary mask was placed over them. Unexposed SU8-2000 was unsuitable because it reflowed when under ion bombardment at high temperature, but little drops of viscous (partially dried) PMMA remained unmoved in the CAIBE and easily came off in acetone, thereafter. This mask is illustrated in Figure 2.26.

The purchased blends of SU8 2000 (2000.5 and 2050) gave certain ranges of thicknesses, but some applications required different thicknesses. To this end, mixtures were made. In the instance of the inter ridge insulation when the tear-off method was used, SU8-2000.5 was mixed with the solvent, cyclopentanone, as discussed previously. Originally, for the lining of the channel walls, a 1:1 mixture of the two blends was used, whose thickness range is shown, along with others, in Figure 2.27. Before the glass and wax chamber was thought of, the chamber walls were made of very thick layers of viscous SU8-2000, that was made by evaporating the solvent from SU8-2050 on a hotplate. Layers up to  $600\ \mu\text{m}$  thick were created by spin coating at 1000 rpm, but they had significant undulations. Also, these layers were unreliable, and often the lithography left residues that filled in the channels, so the method was abandoned in favour of the better scheme.

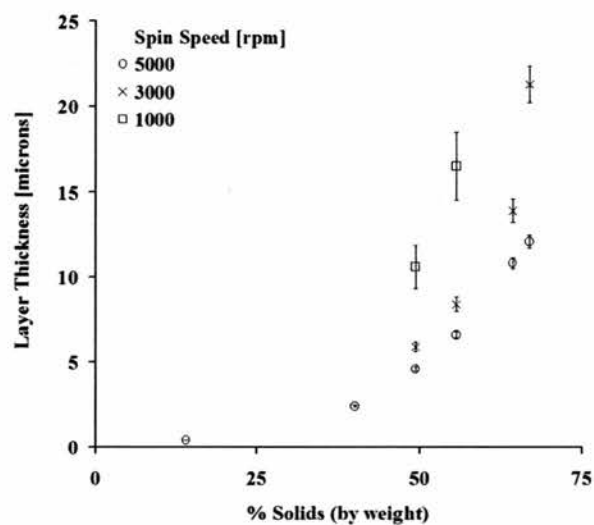


Figure 2.27: Thicknesses of blends of SU8-2000.5 and SU8-2050.

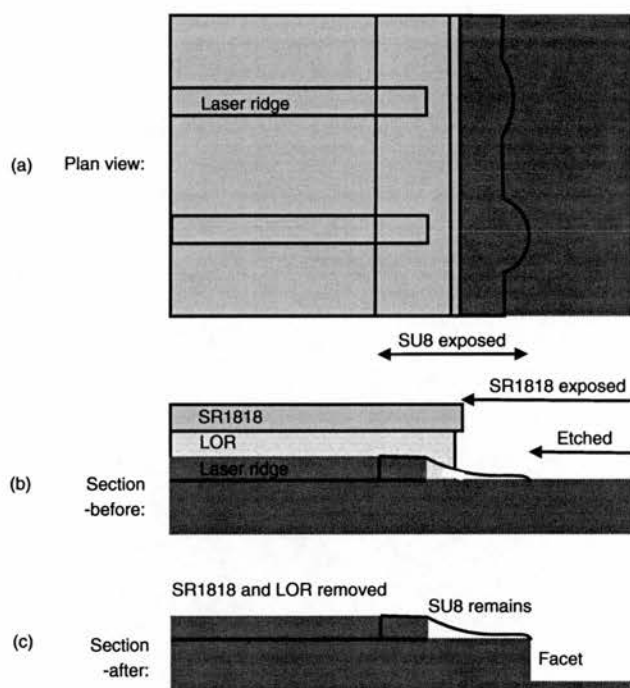


Figure 2.28: Scheme for etching curved facets. This method would exploit the good resolution of thin layers of strong SU8 2000, and the LOR 7B would allow for the removal of the SR1818 after the etch, thus revealing the laser contact pads for electrical probing. (a) plan view of composite mask; (b) cross-section of mask; (c) cross-section of sample after facets have been etched and mask has been removed, leaving only SU8-2000 polymer.

## 2.7 Further Work

Optically, the most important advance would be to increase the power density within the trapping channel. This could be accomplished by fabricating curved facets in order to give focused beams and, hence, higher trapping powers. This could be realised for horizontal beam-shaping by etching curved facets. SR1818 polymer had a limited resolution, so a novel etch mask was developed, using SU8-2000.5, which was thin enough to give the required resolution for small curved features. Illustrated in Figure 2.28, the scheme is under development. The LOR and SR1818 resist the etch and can be removed thereafter to allow access to the contact pads. Due to the higher beam divergence, vertical beam-shaping would have a larger impact upon trapping powers, but this would require a more complex scheme. One option is to vary the etch conditions during the process to give a curved profile; another is to grow a graded AlGaAs cladding layer that would give a graded refractive index when oxidised, and hence would produce lensing effects.

In terms of microfluidics, the most important advance would be the reduction of the chamber volume by removing the walls and moving the lid downwards until it met the trapping channel. This would ensure that all of the submerged particles would have to flow past the lasers, reducing the waste of samples, and permitting the accurate analysis and treatment of entire samples, not just those small proportions that happened to flow along the channel.

## Chapter 3

# Semiconductor Lasers

### 3.1 Design Considerations

stem from sthThis project made only small demands of the lasers, and so their design was simple. The most efficient use of the available power was in the zero-order mode, concentrating all of the power into a single spot; this was accomplished by creating a suitable ridge waveguide, as described in Section 1.7. The amount of power required for trapping was estimated to be about 5 mW; this was based on previous experience with dual-beam traps, and also on supportive examples in the literature. For example, although *Ashkin (1970)* used over 100 mW for some experiments, he did use 19 mW for one dual-beam experiment, and that was with a larger chamber where power densities in the diverging beams were therefore lower than in these integrated devices. The fibre trap of *Constable et al. (1993)* had fibre separations that varied from 20 to 280  $\mu\text{m}$ , which covers the range used in this work. In that paper a diode laser emitting 7 mW of power at a wavelength of 1.3  $\mu\text{m}$  was able to create one half of the trap, lending credence to the estimate of 5mW. This was an average value, but continuous wave operation was preferable to pulsed, because it required no complex electronics. But, for continuous operation, the lasers had to be thermally stable, and that required low electrical resistances and also heat sinking. In terms of spectral characteristics, the spectral quality was deemed to be unimportant, and the nominal wavelength was dictated by the structure of the GaAs based laser material, of which two were available.

The first to be available was grown at The National III-V Semiconductor Centre at Sheffield University; it had a double quantum well structure, and emitted at 980 nm. The second became available towards the end of the project; it was manufactured by Nanosemiconductor GmbH, Dortmund, Germany, and had InAs quantum dots that emit at 1290 nm. Both provided ample power, and could be fabricated to support only the fundamental mode, as was required. Neither material offered any significant advantage to this application. The infra-red region of the spectrum, in which both emit, is poorly absorbed by chromophores, such as haemoglobin and chlorophyll, within cells, whereas shorter wavelengths towards the ultra violet end of the spectrum are more strongly absorbed and can cause cell damage. This may be due to the actions of specific wavelengths of light, and it may or may not be due to the general heating that results from the addition of

optical energy to the molecules within the cells. Such heating tends to be small ( $\sim 1^\circ\text{C}$  per minute at 100 mW). However, the Ohmic heating within the diode lasers tended to raise the temperature of the immediate environment by  $\sim 2^\circ\text{C}$  per 100 mA of current, and the integrated nature of the device means that the liquid and any cells were heated by this route. Such an increase was not a problem, even when multiplied over several lasers, provided that the device was well heat-sunked or even actively cooled. Also, it is well known that higher energy ultra-violet light can cause damaging ionisation in chromosomes, leading to cancerous mutations. The only such issue with the use of infra red lasers is that the absorption by water increases with wavelength, although the so-called “telecoms windows” at  $1.3\ \mu\text{m}$  and  $1.55\ \mu\text{m}$  offer much lower absorption and hence less heating. So the quantum dot emission at 1290 nm was, in fact, a very good choice, offering sufficient power at a wavelength that causes little or no damage to cells.

The operation of such a laser has been outlined with reference to Figure 2.6. This Chapter expands upon that outline, but with the intention of explaining the basic principles, rather than delving deeply into the mathematics. The discussion begins by looking at the electronic processes that can lead to light emission in semiconductors, and it then moves on to predict the basic relationship between the laser parameters and the output power. The optimum cavity length is considered and then determined empirically. Thereafter, the power that enters the trapping channel is predicted and compared with measurements, which is the most important part of the Chapter. It concludes with a few observations concerning the operation of lasers in the devices.

## 3.2 Basic Semiconductor Processes

Semiconductor materials are those whose electrical conductivity is higher than that of an insulator, but lower than that of a conductor. In addition, it increases with temperature due to the promotion of electrons across forbidden energy bandgaps, analogous to the promotion of an electron between two of an atom's energy levels. This is in contrast to conductors, in which all of the available electrons are naturally present in the conduction bands, giving higher conductivities at any temperature. But any increase in temperature adds thermal agitation that serves to hinder motion of the conducting electrons, reducing the conductivity of the conductor.

The main processes that take place in a sample of intrinsic (pure) semiconductor are illustrated in sketch form and in an energy diagram in Figure 3.1; the values are for GaAs, which forms the basis of the laser materials. (i) The basic electronic arrangement shows the crystal's uppermost bandgap that separates the valence (bonding) states from the conduction (free) states, which all have energy and momentum values that are deduced from the nearly-free electron model. These quantities do not translate into actual particle motion, but they do affect which carriers can move under the influence of an applied electric field, as discussed later. In an intrinsic semiconductor each atom contributes an average of four bonding electrons to the tetrahedral bonds that give each atom its favoured configuration of a full outer shell of eight electrons. The bandgap represents the ionisation energy that is required to break such a bond, freeing an electron to move around the crystal in the conduction band. The novel aspect of semiconductors is that this promotion creates another charge carrier, a hole (denoted by  $h$ ), in the conduction band; it is not a real entity, but rather a convenient way of describing the behaviour of the surrounding electrons, that can now move around the

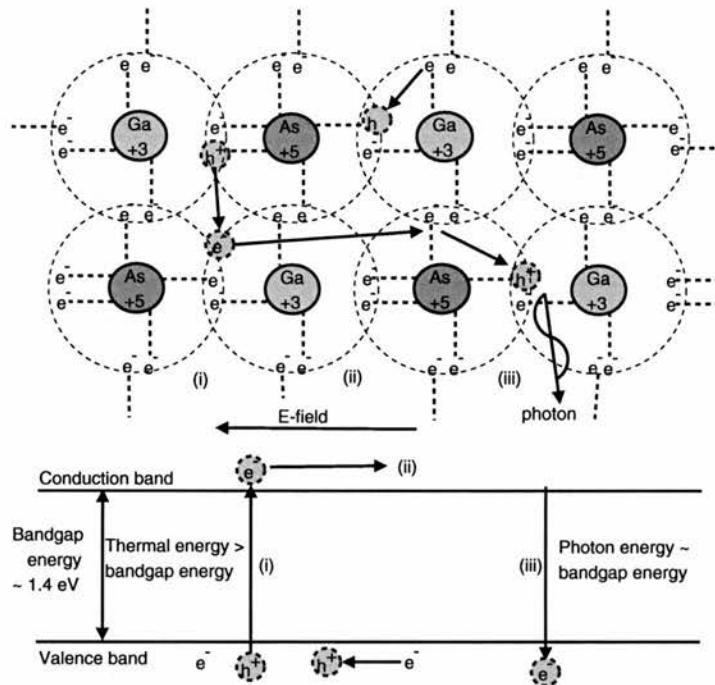


Figure 3.1: Electronic processes in intrinsic semiconductors in (top) sketch form, and (bottom) an energy diagram. Electrons in the outermost energy levels form bonds; (i) they can be removed by the addition of sufficient energy, leaving a hole behind; (ii) the electrons and the holes will travel in response to an applied electric field; (iii) the electrons can re-enter a bonding site (recombine with a hole) emitting a photon.

crystal, from one bond to another, with relative ease. The population distributions of the free electrons,  $n_e$ , and holes,  $p_h$ , are determined by the thermal energy,  $kT$ , of the system; the free charges move randomly between collisions with zero net charge transfer. (ii) The transfer of charge in the presence of an applied electric field,  $\mathbf{E}$ , is directed along the field lines, and the rate (expressed as the current density,  $\mathbf{j}$ ) is governed by the effective mass,  $m^*$ , which is lower than the rest mass,  $m_0$ , in order to account for the assistance given by the periodic potential to the moving charges, and the mean free time,  $\tau$ , which is the average time for which they can move at speed between collisions. The total conductivity is the sum of those of the electrons and holes, both of which act in the same direction; that is, both give a net flow of positive charge in the direction of the applied electric field. (iii) The electrons have finite upper-state lifetimes, after which they recombine with holes, losing the associated energy either in non-radiative phonon processes, or by the emission of a photon whose energy is roughly equal to that of the bandgap.

### 3.2.1 Increased Conduction by Doping

The intrinsic carrier density, and hence the conductivity, of a semiconductor are low. This is partly because the holes do not contribute as much as do the electrons; the mobility  $\nu = e\tau/m^*$  of holes is lower than that of electrons, essentially because it is more of an undertaking to re-arrange bound electrons in order to move a hole than it is to move a free electron. Even if the holes did contribute as much as the electrons do, the

total conductivity would still be low. Increasing the thermal energy does not help much. The only way to significantly increase the conductivity is to add dopants, creating an extrinsic (impure) semiconductor, as illustrated in Figure 3.2.

In the case of GaAs material, some of the gallium can be substituted with a group VI element such as selenium, to create an n-type semiconductor. Each selenium atom is a donor that brings five bonding electrons; the extra one is not needed for the creation of the stable outer shell of eight electrons, and is held only very loosely. A few meV of energy are sufficient to free it from the donor atom, promoting it into the conduction band. The remaining ion has a hole, but it is not a useful charge carrier: A hole in the valence band describes a gap in a sea of electrons that can move by changing places with the hole. But the “hole” in the donor ion is a “gap amongst gaps”; all of the donors are ionised, so they all have holes and there are no remaining electrons that can move via the holes. Hence, the population density of negative carriers increases in proportion to the dopant concentration, increasing the conductivity. It should be noted that the larger number of carriers leads to more collisions, reducing the mobility, but the increased carrier concentration dominates, giving the significant increase in conductivity that is required. In the same manner, the substitution of arsenic with a group II element such as zinc, each of which is an acceptor of electrons, creates a p-type semiconductor in which the holes are the majority carriers.

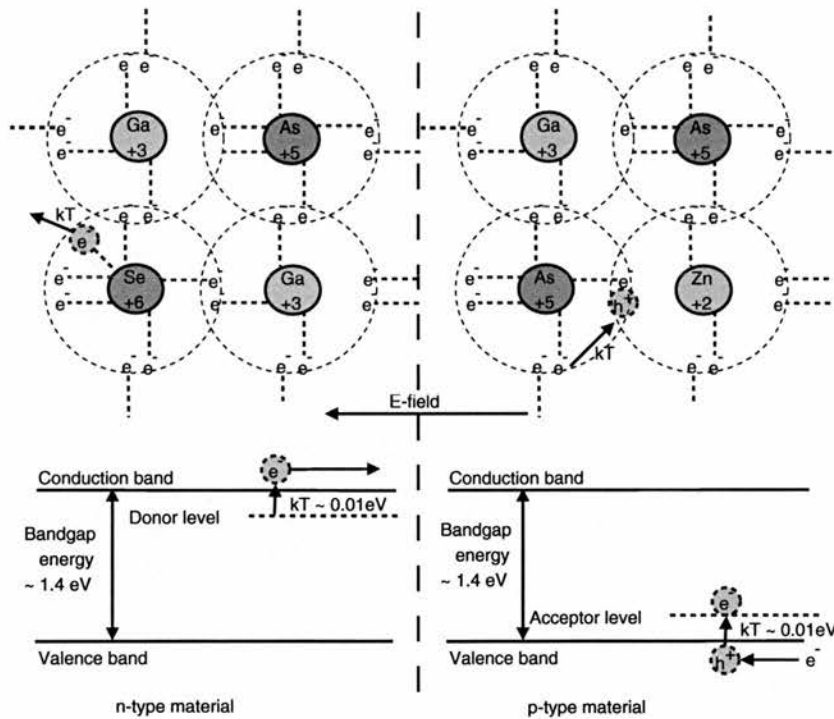


Figure 3.2: Electronic processes in extrinsic semiconductors: doping can form (left) n-type and (right) p-type semiconductors. The addition of dopant atoms provides a source of carriers that is more easily accessible (thermal energy is sufficient) than those in an intrinsic semiconductor, thus increasing the conductivity.

### 3.2.2 PN Junction and the Generation of Light

If a volume of n-type material is created in contact with one of p-type, the resulting pn junction displays useful characteristics. The example that is illustrated in Figure 3.3 is of a homojunction, one in which the two types are of the same material, differing only in their dopants. Some of the free carriers diffuse across the junction, and pairs of electrons and holes recombine to create a region of ions with no free charges. This so-called depletion region has a net electric field that roughly equals the bandgap; it repels any further carriers that drift towards the junction, but the barrier can be overcome with the aid of an applied electric field.

A forward-biased potential difference pushes electrons into the n type and attracts them out of the p-type. The original charges are repelled towards the junction, cancelling out some of the ions, reducing the width of the depletion region and hence the height of the potential barrier. So, the current density is determined by the applied voltage in the following two ways. Firstly, the larger the applied voltage, the greater the number of carriers that can surmount the barrier and flow across the junction. Secondly, the larger the applied voltage, the more energy each carrier retains after surmounting the barrier, and hence the more easily it travels around the rest of the circuit. Initially, the current density is limited by the proportion of each population that can surmount the barrier; so the current follows the roughly exponential increase of the “useful” population. Once the applied voltage is larger than the barrier, the entire populations can cross the junction, and so the current density is linearly proportional to the applied voltage. These two regimes are clearly distinguished on a plot of current,  $i$ , against applied voltage,  $V$ , and the boundary is known as the turn-on voltage,  $V_{on}$ . In the regime in which  $V > V_{on}$  a change in voltage,  $dV$ , induces a change in current,  $di$ , giving a linear gradient of  $di/dV$ , whose inverse is the diode’s dynamic series resistance. Throughout this procedure, the populations are being constantly replenished by injected charges.

Once electrons and holes have entered the junction, they remain separate for, on average, the upper state

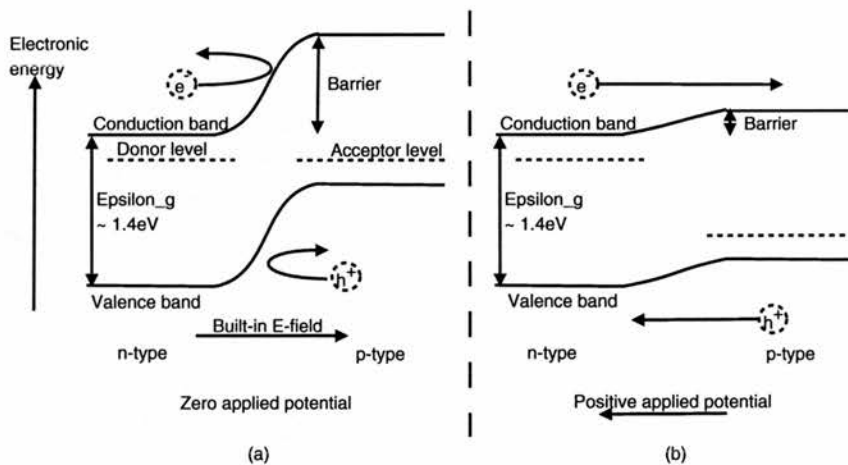


Figure 3.3: The operation of a pn junction: (a) The separation of charges at the boundary creates a built-in electric field that repels the carriers from the junction, preventing the flow of current. (b) The addition of a positive applied voltage lowers the barrier, allowing a current to flow across.

lifetime, before recombining to create energetically-favourable, full outer electron shells. In so doing the energy is either lost to the lattice through non-radiative processes, or is emitted as a photon whose energy is roughly equal to that of the bandgap.

Initially, all of these events are spontaneous emission events. The timing, direction and phase are all random, so that much of the light is lost into the material; and the lack of coherence means that the photons tend to cancel one another out by destructive interference, so the intensity is low. However, a photon that happens to be travelling along the direction of the junction passes amongst a large number of electron-hole pairs that have yet to recombine, and can trigger one of them to recombine in a stimulated emission event. The phase, energy and direction of the emitted photon are identical to those of the incident photon, so the intensities add together. These two photons can each repeat the process, and their number can grow to create an intense laser mode. That is, the pn junction provides the optical gain that is one of the requirements for laser action, as has been outlined earlier. The full story, including how the use of different layers improves upon the simple homojunction, is given shortly, but first it is worth considering a few issues.

### 3.3 Internal Laser Action

#### 3.3.1 Aspects of Particle and Wave Models

It should be noted that the mode's photon number density,  $N[\text{m}^{-3}]$ , the optical intensity,  $I[\text{J s}^{-1} \text{m}^{-2}]$ , and the optical power,  $P[\text{J s}^{-1}]$ , are all proportional to one another, and can be interchanged in discussions, depending upon which is most useful. Outwith the cavity the optical power is the most useful parameter, being easily measured. Inside the cavity it is difficult to make any measurements, so that is not a consideration, so either the photon number density or the intensity can be used. It is generally preferable to use the former because it is most closely linked to the particle photon model of laser action. However, it should be noted that this photon particle model suggests that stimulated emission occurs only at the location of the photon, and that only the small region around the initial photon contains any optical power, as illustrated in Figure 3.4 (left). The optical power would then be concentrated into one small burst that travels around the cavity. By contrast, the wave model of light, which is best described using the optical intensity, suggests that that light is actually a travelling wave that exists all along the length of the cavity and beyond. In the wave model, the importance of coherent phase becomes apparent, because each successive travelling wave overlaps with its predecessors; this occurs over the course of multiple round-trips, and so any phase mis-match would result in a reduction of the optical intensity.

This argument also tells us that there are constraints upon the wavelengths,  $\lambda$  (in a vacuum), of light that can contribute the laser mode. Only those that satisfy the condition  $m\lambda = 2nL$ , where  $m$  is an integer,  $L$  is the cavity length, and  $n$  is the effective refractive index of the medium, will return to their starting point with the same relative phase and thus perpetuate themselves. The energy,  $\epsilon$ , of a photon is given by  $\epsilon = h\nu$  where  $h$  is Planck's constant and  $\nu$  is the frequency of the oscillation. This frequency is equal to the velocity of the wave,  $v$ , divided by its wavelength,  $\lambda$ , and has the same value in every medium; so,  $\epsilon = hc/\lambda$ , which is independent of the refractive index. The finely-spaced energy levels within the semiconductor material

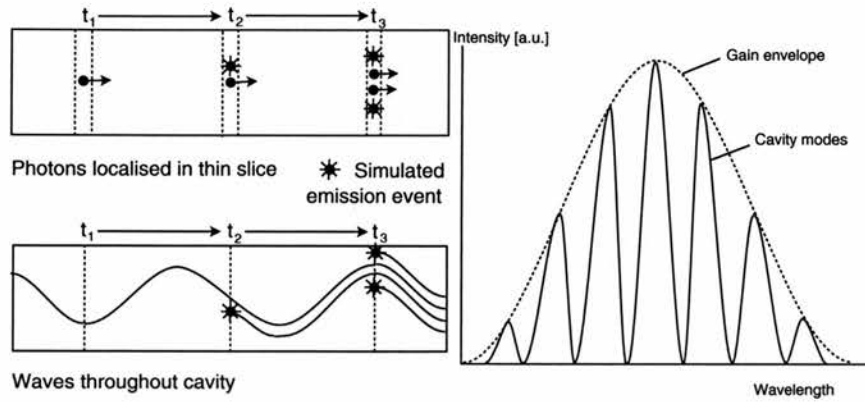


Figure 3.4: Issues concerning cavity modes: (left) The photon and wave models of light suggest different distributions of intensity within a laser cavity. (right) The gain medium provides gain across a continuum of states, but a cavity can only support laser action at discrete wavelengths within the gain envelope.

allow for a virtual continuum of these photon energies, represented by the gain envelope in Figure 3.4 (right), but only those that satisfy the cavity condition will actually propagate, giving the optical spectrum a series of fine peaks. The spacing between these peaks is found as follows. The frequency difference,  $\Delta\nu$ , between two adjacent cavity modes is

$$\Delta\nu = \nu_{m+1} - \nu_m = \frac{c}{2nL} \quad (3.1)$$

Then, the frequency relation can be differentiated to give

$$\frac{d\nu}{d\lambda} = -\frac{c}{\lambda^2} \quad (3.2)$$

which, for small peak separations that approximate to this differential limit, can be combined with the expression in Equation (3.1) to give

$$|\Delta\lambda| = \frac{\lambda^2}{2nL} \quad (3.3)$$

For example, the GaAs-based lasers used in this work had a refractive index of 3.4, were about 2 mm long and emitted at wavelengths around 1290 nm; the frequency and wavelength spacings for such a laser should be 22.1 GHz and 0.122 nm, respectively.

The average power per unit time is the same in both the particle and wave models, but the wave model gives a truer illustration of the situation, in which there is some power at every point in the cavity. The photon model allows for a more concise description of the processes that occur over a round trip, but it should be remembered that the photons represent the total energy condensed into a small region. With all of that in mind, the ensuing discussion uses electrical current,  $i$ , and photon number density,  $N$ .

### 3.3.2 Building up to a Laser Mode

In order to generate a laser mode, whose phase must be coherent from one round-trip to the next, the following sequence of events must occur, as illustrated in Figure 3.5. (i) Of all of the spontaneously-emitted photons, one must travel parallel to the axis of the cavity, and must have a wavelength that satisfies the conditions mentioned above. (ii) There must be an upper-state carrier population so that this photon can trigger the stimulated emission of an identical photon. (iii) The upper-state carrier population must exceed the lower-state carrier population so that the number of stimulated emission events exceeds the number of absorption events (for which the probabilities of an individual event of either type are equal) allowing the photons to trigger a cascade of stimulated emission. This condition is known as transparency; that is, a photon has a chance of getting through the material without being absorbed, whereas before it was certain to be absorbed. (iv) The excess must be larger still, because some of the upper-state carriers are used in non-radiative processes, such as bimolecular transitions and Auger transitions. (v) The carrier population inversion must be sufficiently large that the rate of generation of extra photons exceeds their rate of loss to material losses such as scattering. (vi) The carrier population must be larger still, because the cross-sectional area of the optical mode is larger than that of the gain region, so only a certain fraction of the photons in the mode is actually in the right place to interact with the upper-state population. This is described by the confinement factor,  $\Gamma$ . (vii) When the photons encounter a facet at an end of the cavity, only a certain proportion is reflected back into the cavity, and this proportion must be large enough to perpetuate the phase of the photon population through another length of the cavity, without any other spontaneously-emitted photon and its clones taking over. When the population inversion is sufficient to balance the losses, the laser is said to be at threshold. Above threshold there are insufficient pitfalls to catch all of the laser mode photons that are generated per unit time, and the mode's population grows until it extracts all of the gain that is available, per unit time, at which point it maintains a steady-state intensity. The photon population will circulate around the cavity with a constant phase, and the outputs from each successive round-trip will augment one another in perfect phase, giving a high intensity beam. This can be summarised by the following rate equation for the photon number density,  $N$ :

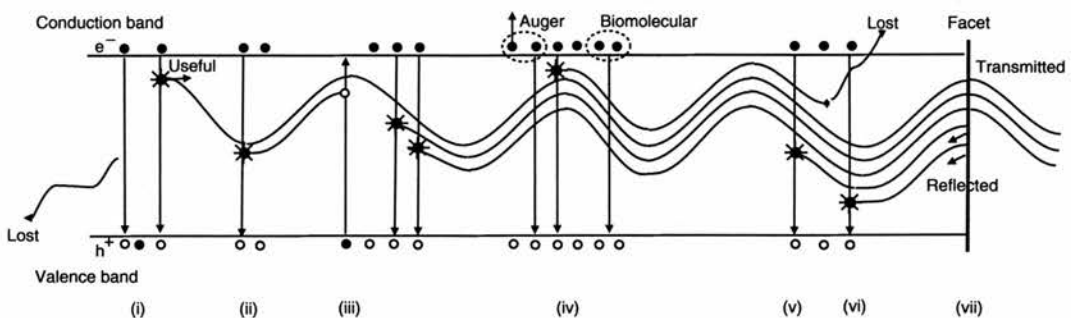


Figure 3.5: Sequence for laser action. The various steps that lead to the creation of a self-perpetuating laser mode are illustrated, and are described in the main text.

$$\frac{dN}{dt} = \Gamma g v_g N + \Gamma \beta_{sp} \frac{N_c}{\tau_{sp}} - \frac{N}{\tau_{cav}} \quad (3.4)$$

The first term on the right-hand side represents stimulated emission, the rate of which is proportional to  $N$ . It also depends upon the confinement factor,  $\Gamma$ , which is discussed later, the gain co-efficient,  $g$ , that describes the efficiency with which stimulated emission occurs, and the group velocity of the mode,  $v_g$ , that determines how quickly the photons move through the gain volume. The second term on the right-hand side represents spontaneous emission, whose rate is proportional to the carrier number density,  $N_c$ , and also to  $\Gamma$ , as well as  $\beta_{sp}$ , the small fraction of the spontaneously-emitted photons that contributes to the mode. It is generally small, but it is this that initiates the laser mode. The second term is also inversely proportional to the spontaneous emission lifetime,  $\tau_{sp}$ , which is the average time for which carriers will remain excited before spontaneously recombining to emit a photon. The final term on the right-hand side represents the losses; the cavity lifetime,  $\tau_{cav}$ , is the average lifetime of a photon within the cavity, and is a combination of the loss factors; that is, the absorption and the facet transmission. A similar, coupled equation describes the upper state carrier population; together, these two equations allow modelling of dynamic laser effects, but this work deals with steady-state conditions.

### 3.3.3 Benefits of Heterostructures

The simple homojunction illustrated in Figure 3.3 was first demonstrated by *Goucher et al. (1950)*. However, it has several disadvantages that limit its efficiency. Firstly, recombination only occurs within the thin ( $\sim 10$  nm) region where the populations overlap; the number of carriers in so small a region is low, so the gain is also low. Secondly, once the light has been generated, the only way in which it is confined to the junction is by the slight increase in refractive index that is caused by the extra carriers: so-called gain guiding. It is, however, a weak effect, and therefore many of the photons will be lost into the material, neither contributing to the mode themselves, nor extracting gain to boost the intensity. The high currents that were required to overcome these issues meant that the lasers had to be cooled to very low temperatures.

As early as 1963, *Kromer (1963)* first suggested that a heterostructure of different layers could provide better charge confinement and hence more efficient operation. The development of epitaxial chemical vapour deposition (CVD) by *Sheftal et al. (1957)* allowed the creation of such structures. The first operation of a heterostructure laser at room temperature was by *Kressel and Nelson (1969)*, but that was with pulsed current to prevent overheating. CW operation was shown by *Hayashi et al. (1970)*. The development by *Cho (1971)* of molecular beam epitaxy (MBE) allowed the deposition of single atomic layers for even greater control of the material properties.

These structures are all based upon the properties that are plotted in Figure 3.6. The lattice constant determines the mechanical stability of the layers, and so only certain combinations of materials whose lattice constants match can be used together. The bandgap and the refractive indices then determine the electrical and optical properties of the junctions. The benefits of heterostructures can be understood by considering the structure of the quantum well material in terms of the refractive indices and the bandgap energies, as shown in Figure 3.7.

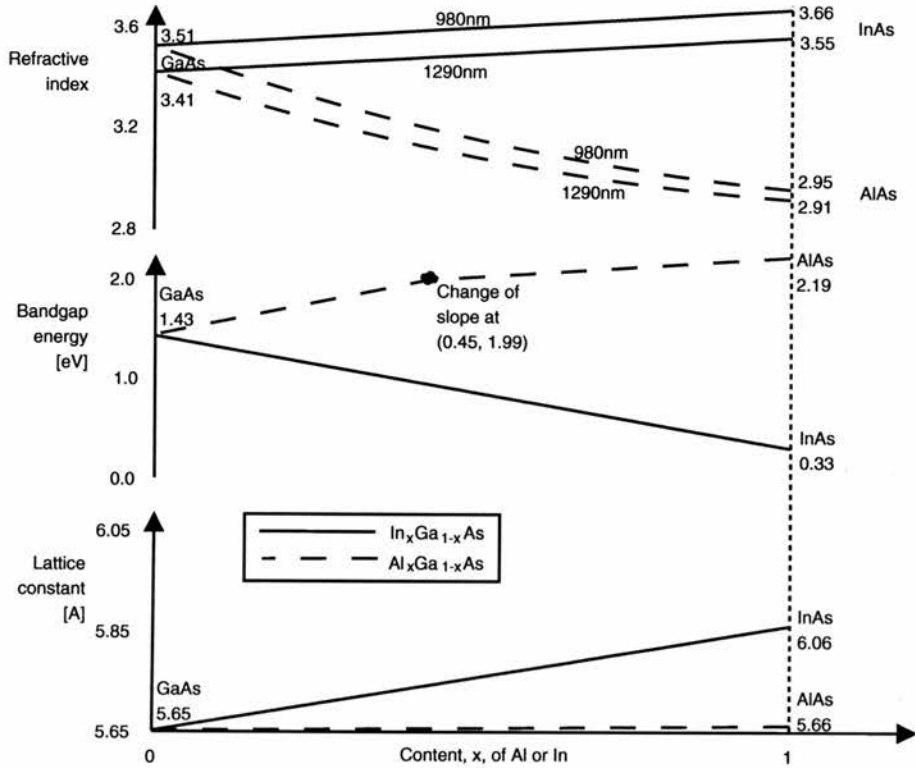


Figure 3.6: Properties of GaAs-based compounds. The horizontal axis represents the fraction,  $x$ , of gallium that has been replaced, by either indium or aluminium.  $x$  ranges from 0 (pure GaAs) to 1 (all gallium replaced). (top) Refractive index at wavelengths of 980 nm and 1290 nm; (middle) bandgap energy; (bottom) lattice constant. The first two parameters are used to tailor the optical and electrical properties of heterostructures, and the lattice constant determines the stability of the multilayers.

The carrier populations are provided by the n- and p-type GaAs, as in the simple homojunction, but it is the thin layers in between that address the problems. Firstly, the larger bandgap of the AlGaAs, as seen in Figure 3.7, acts as a potential barrier. Carriers must possess extra energy to overcome that barrier, but any that do manage this feat (from either the p- or the n-type material) end up in the lower bandgap GaAs with the AlGaAs barriers on either side. They find it hard to get back out again, leading to a build up of carrier density, and hence of the gain per unit volume that is available to the laser mode. Heterojunctions have been created with just those layers shown in Figure 3.7 (top), but the InGaAs layers that are shown in Figure 3.7 (bottom) add an extra advantage, creating one-dimensional potential wells that are narrow enough (5–40 nm, in general) to place quantum mechanical limitations upon the energy levels therein, reducing the number of permissible energy states. This reduces the number of possible electronic transitions, allowing the output wavelength to be tuned via the thickness and refractive indices of the layers (*Dingle et al. (1974)*); in this case, the two 7.5 nm-thick wells emit at 980 nm. But, more importantly, with fewer states a smaller upper-state population constitutes a population inversion, so a much smaller current density is required in order to reach threshold. This size resolution is only possible with MBE techniques.

Used in isolation a single quantum well (SQW) is not much better than a homojunction, for the size

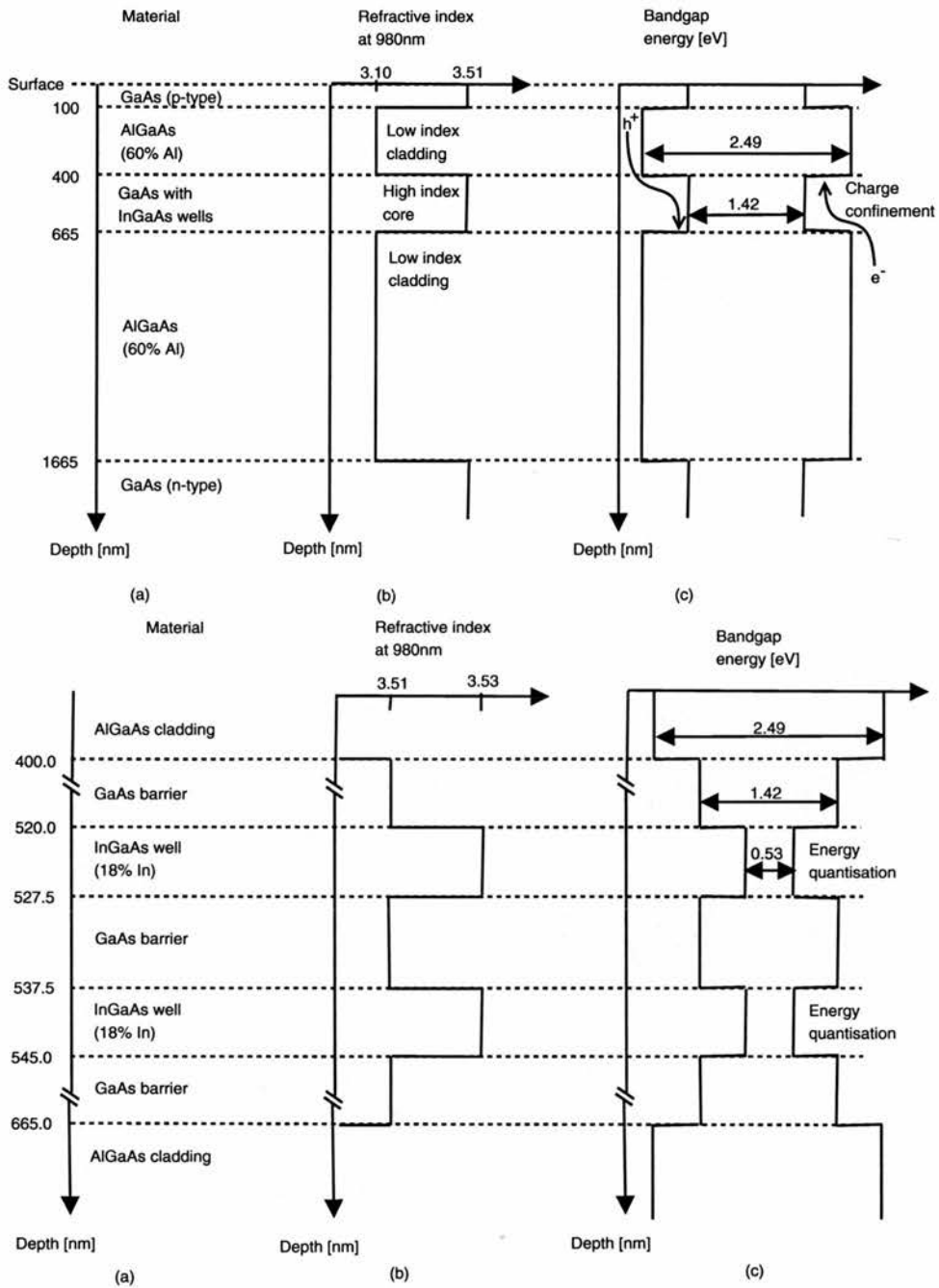


Figure 3.7: Structure of QT1841 quantum well material. Top (overview): (a) The composition and thickness of the layers determine the waveguiding and electrical properties; (b) the high index GaAs creates the core of the waveguide in the AlGaAs cladding; (c) the AlGaAs has a higher bandgap, and therefore traps carriers in the low bandgap core, providing more gain for the optical mode. Bottom (details of core): (a) the layers of material maintain the (b) high index of the core; (c) but they modify the bandgap energies to quantise the energy levels.

of the gain region is so small, giving a tiny confinement factor ( $\sim 0.001-0.01$ ), and the carriers can only be confined within that small region. It is, therefore, important that the wells are fabricated within a heterojunction such as the one in Figure 3.7, because, as described above, it confines the carriers, providing a constant supply of carriers for the wells. Multiple quantum wells (MQW) are better still, for the larger the number of wells (two in this project) separated by barrier layers, the better, for more of the light in the mode experiences the wells' gain; in fact, confinement factors of  $\sim 0.2$  are typical for MQW structures.

The simplest MQW structures use the cladding material for the barrier layers. However, the cladding material necessarily has a large bandgap which has the effect of inhibiting the flow of electrons within the core, so that the only confinement is provided by the layers of InGaAs. It is essentially no better than a series of homojunctions in close succession.

The material used in this project has a modified MQW (MMQW) structure, which is a combination of MQW and heterostructures. The quantum wells are imbedded in the core of the waveguide, so that the barrier layers are formed of the core material, in this case GaAs. The bandgap is larger than that of the wells, thus maintaining the quantum confinement; and it is smaller than that of the cladding, thus permitting the easier flow of carriers around the potential trap and into the quantum wells, whilst the charges are still confined by the cladding layers, maintaining the high carrier concentration.

The second advantage that the design shown in Figure 3.7 has over the homojunction is that the refractive index difference between the lower index AlGaAs and the higher index GaAs creates a waveguide. Photons that travel at small enough angles to the layers will be reflected back by the boundary, preventing them from being lost into the material. The tighter the confinement, the more of the mode that overlaps with the quantum wells, and thus the higher the gain. Indeed, this argument also helps when designing MQW structures: AlGaAs would reduce the index contrast, but the use of GaAs as the barrier material maintains a higher index contrast, giving a good confinement factor.

The other material that was used in this project uses a further refinement of the quantum confinement: namely, quantum dots. Rather than thin layers of material with a smaller bandgap, these are little islands of such material into which carriers move and in which they are confined. The even more stringent limitations that this three-dimensional confinement places upon the permitted energy levels reduce still further the number of possible states that are available to carriers, thus reducing the value of the upper state population that is required in order to constitute an inversion. Again, the size of the dots is a means by which the emission wavelength can be tuned, and the InAs dots used in this project emitted at 1290 nm. They are grown upon layers of GaAs by molecular beam epitaxy, and by taking advantage of the tendency to self-assemble, which also limits their maximum size. Each dot starts from one atom that adsorbs to a bonding site on the surface, with no lattice mismatch. The dot grows when other atoms land next to the first one; the mismatch means that these later atoms cannot settle on binding sites, but are off set slightly, by  $\sim 6\%$  in the case of InAs on GaAs, as seen in Figure 3.6(c), and so on, until the ninth atom is off-set by  $\sim 48\%$ . The tenth is then at  $\sim 54\%$ , but that is over half of an atomic spacing so it would rather move to the next bonding site, marking the end of the growth of the dot. Also, this tenth atom cannot start another dot in such close proximity to its large neighbour, so dots form separately, maintaining the small size and the resulting quantum restrictions. The vertical growth is limited by the strain that is induced by the lattice mismatch, to about 3 or 4 atoms thick. GaAs is then added to give a capping layer that planarises the surface within about

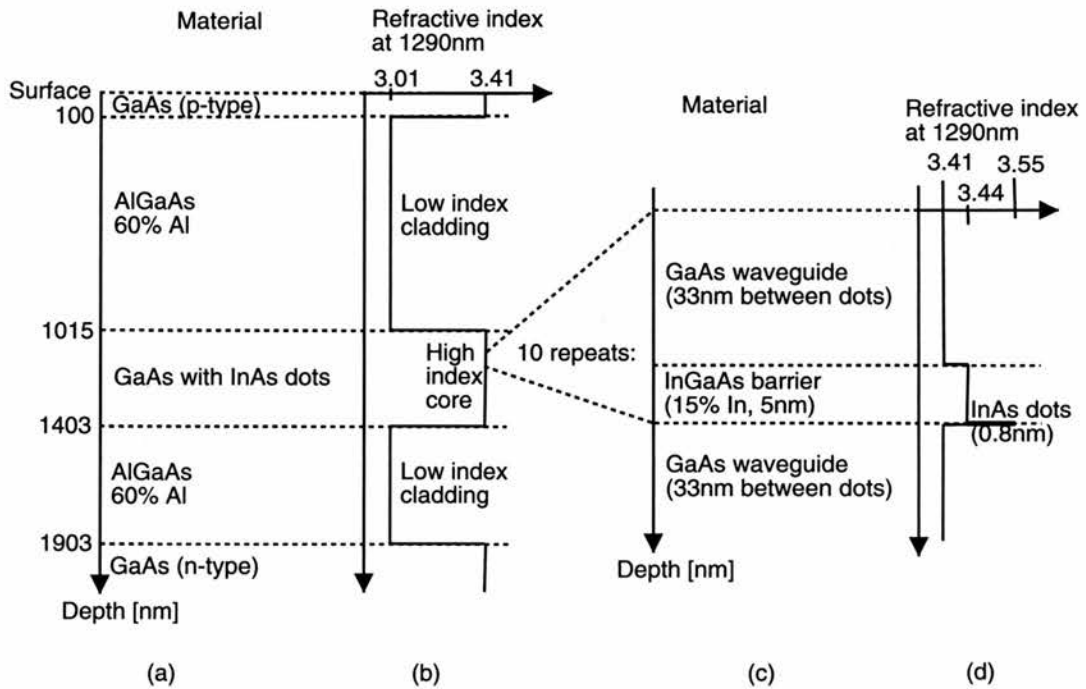


Figure 3.8: Structure of DO451 quantum dot material. For simplicity the bandgap energies are omitted, and only the refractive indices are shown. (a,b) The waveguiding structure is similar to that in the quantum well material in Figure 3.7. (c,d) A close-up of one layer of quantum dots shows that they do not reduce the refractive index of the core.

ten atomic layers. Generally, multiple layers of dots are built up to give higher gain; the material used in this work had ten such layers. Incidentally, the residual strain in each GaAs capping layer leaves a “marker” on top of the GaAs at which a dot on the next layer will preferentially grow, so the dots in different layers tend to be neatly arranged on top of one another. This structure is illustrated in Figure 3.8. Because the dots do not form a continuous layer as the wells do, there are gaps in between them through which carriers can pass without contributing anything to the optical mode. This leads to a lower confinement factor, but this is more than compensated for by the beneficial effects of the energy quantisation. The waveguiding and electrical confinement are provided in much the same way as for the quantum well material.

### 3.3.4 Ridges

Once the material has been grown, the vertical carrier confinement and waveguiding cannot be modified, but there is still scope to control the electrical and optical performance of the junction via the dimensions of the waveguiding ridge. These are created by etching away material on each side, and, as illustrated in Figure 3.9, they can be either deeply etched right through the active layer, or shallow etched to a depth just above the active layer (*Kaminow et al. (1979)*). The two main functions of the ridge are transverse confinement of the injected charges, and transverse confinement of the optical mode, and both of these are performed more effectively by deeply-etched ridges.

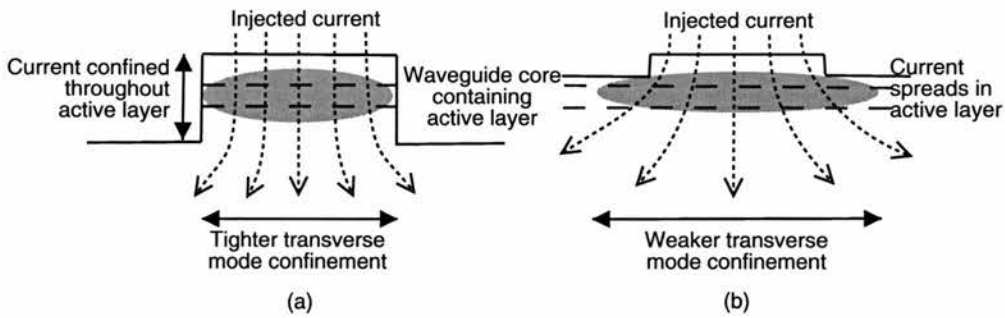


Figure 3.9: Electrical and optical effects of deep and shallow etches. (a) A deep etch confines the mode to a smaller volume, and it ensures that all of the injected current passes through that mode, giving a high intensity. (b) A shallow etch provides less optical, and less electrical, confinement, but does not risk disrupting the gain material.

The mutual repulsion of like charges causes the injected currents to spread within the available volume. The deeply-etched ridges provide no opportunity for such spreading at the active layer, maintaining high current densities across a small area, giving low threshold currents and wasting little current in sub-threshold regions. In contrast, shallow ridges allow the currents to spread, resulting in lower current densities that cover a larger region; a higher total threshold current is required, and more current is wasted in the wings that do not reach threshold. The ridge should therefore be etched as deeply as possible without reaching the active layer, but that places stringent stipulations upon the etch depth. In addition to electrical confinement the horizontal waveguiding should be considered. A deep ridge provides strong index-guiding (and once the width that will support only the zero-order mode has been determined, then the depth has no deeper limit, so the etching requires little accuracy), whereas a shallow etch provides weak index guiding. This all begs the question why shallow etching should ever be used.

Deep etching causes problems because it can lead to a phenomenon known as surface recombination. Around the etches the “quantum neighbourhood” is disrupted, reducing the quantum confinement in wells and dots, and hence increasing the number of permissible energy levels. This changes the emission wavelengths of those dots, and the photons will therefore not contribute constructively to the mode, and will in fact act to partially cancel its intensity, whilst also stealing gain from it. In addition, the reduction of the quantum confinement also increases the current density that is required in order to reach threshold, further degrading the performance. The effects are much worse in quantum well lasers because the wells are dissected right along each etch, giving a large area over which surface recombination can occur. That is why the quantum well material required shallow etching. Quantum dot material suffers rather less because a deep etch interferes with only the small proportion of dots that lie along the line of the etch, and so deep etching, with its benefits of lower threshold currents and less stringent etch depth, is possible. However, two issues led to its rejection. The first was purely practical, namely the etch had to be very smooth because rough patches would scatter light out of the ridge, and such smoothness was only possible with electron-beam lithography, which had been discounted on various grounds. The second reason was that the tighter the optical confinement, the larger the angle at which the mode will diverge when it is finally released from its waveguide; this project required as low a divergence as possible in order to maximise the intensity in the traps. So, shallow etching was used for both the quantum well and the quantum dot material; in fact, it

was actually quite convenient to be able to use virtually the same fabrication technique for both materials. The actual widths and depths of the ridges have already been mentioned in the Fabrication Chapter, and the justification for these values is now given.

### 3.3.5 Ridge Width and Depth

The quantum well material was used for the first demonstrations of optical manipulation, but only the length was optimised. The ridges' width and depth were based upon computer simulations that had been conducted (*Whelan-Curtin (2002)*); they supported a single transverse, horizontal mode, although occasionally faint side modes would be seen, suggesting that some of the ridges were slightly too deep. However, once the decision was made to use the quantum dot material for the foreseeable future, it was decided to optimise the ridge parameters for that material. This optimisation is best done numerically, but the simpler argument that applies to a deeply etched rectangular waveguide gives the guidelines that are necessary for a trial-and-error route to optimisation. Figure 3.10 illustrates the factors that determine the transverse waveguiding. The ray illustrates the routes of optical wave trains that constitute transverse optical modes. Each mode can be described by a propagation angle,  $\theta$ ; the zero-order mode, with a single intensity peak, propagates at an angle of roughly  $90^\circ$  to the normal axis on the edges of the core. Snell's law shows that only rays whose angles are above the critical angle,

$$\theta_c = \arcsin \left( \frac{n_{\text{clad}}}{n_{\text{core}}} \right) \tag{3.5}$$

where  $n_{\text{clad}}$  and  $n_{\text{core}}$  are the refractive indices of the cladding and core, respectively, will undergo total internal reflection and remain in the waveguide; rays at larger angles will be partially transmitted each time they reach the interface, diminishing their intensity and hence preventing optical growth. Of the rays

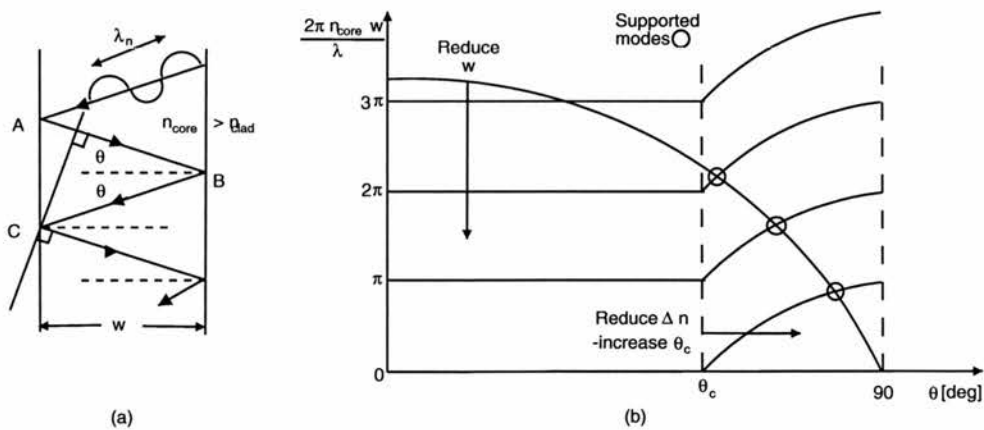


Figure 3.10: Propagation of light in a rectangular waveguide. (a) Light that travels at large enough angles of  $\theta$  (small enough angles to the long axis of the waveguide) can undergo total internal reflection at the boundary between the core and the cladding. But only those that allow for constructive interference will propagate. (b) A graphical method of solving Equation 3.6

that travel above  $\theta_c$ , the only ones that can propagate in the waveguide are those that maintain a coherent wavefront even after multiple reflections; that is, the relative phase of waves passing the same plane that is normal to the direction of propagation must be zero. From Figure 3.10 this is expressed as

$$\frac{2\pi n_{\text{core}} w \cos \theta}{\lambda} - \phi(\theta) = m\pi \quad (3.6)$$

where  $\phi(\theta)$  is the phase change caused by each reflection, which rises from zero at  $\theta_c$  to  $\pi$  at  $90^\circ$ ,  $w$  is the width of the core, and  $m$  is an integer. Re-arranging this expression and plotting both sides as two separate functions on the same graph gives a series of intersections. As shown in Figure 3.10, those that occur at angles larger than  $\theta_c$  give the “cut-off angle” for each mode.

All combinations have at least one intersection, and certain combinations have only one, the zero-order mode that propagates at close to  $\theta = 90^\circ$  and has a single central intensity peak, as required for simple optical trapping. The number of useful intersections on the graphical solution can be reduced by two methods: making the ridge narrower lowers the amplitude of the cosine curve, and reducing the refractive index contrast,  $n_{\text{core}} - n_{\text{clad}}$ , increases the critical angle. The combination of these two effects means that the narrower the ridge, the larger the range of refractive index contrasts that will support only a single mode.

Although the optical interactions in ridge waveguides are more complex than those in rectangular waveguides, they obey the same basic rules. In order to support only a single transverse mode the ridge should be narrow and the refractive index contrast should be low. In this case, though, there is an “effective index contrast”. In terms of the horizontal waveguiding the “core” is the the ridge of GaAs / AlGaAs heterostructure, but the “cladding” is the lower-index material on either side of the ridge. Therefore, the cladding index is determined by the depth to which the upper AlGaAs layer is etched away and replaced by lower index polymer that forms that inter-ridge insulation. A deeper etch allows more of the AlGaAs to be replaced by polymer, thus reducing the cladding index and increasing  $\Delta n$ , which is bad because the waveguide is then more likely to support multiple modes. In contrast, by making the the ridge shallow,  $\Delta n$  is made smaller; this will give single mode operation, provided that the ridge is narrow enough. Expressed in a slightly different manner, reducing the ridge depth reduces the extent of the interactions between the light and the low index material, thus reducing the effective index and increasing the “effective critical angle”. The narrower the ridge, the larger the range of depths that will support only a single mode. Because the CAIBE process had a reproducibility of  $\sim 5\text{-}10\%$ , the ridge depth could vary by that amount, so it was important to have as narrow a ridge as possible in order to guarantee a single transverse mode.

However, the narrower the ridge the higher the resistance and thus the lower the current tolerance and maximum output power. And, anyway, for the reasons discussed in Section 2.5, the narrowest ridges that could be reliably defined across a 6 mm sample by a single lithographic exposure were  $3 \mu\text{m}$  wide, which is a suitable compromise. The ridge depth also requires a compromise, this time between the waveguiding and the electrical confinement. If the ridge is too deep then the index contrast is too high and multiple modes are supported that steal gain from the useful zero order mode; and as the etch approaches the active layer it distorts the mode profile. If the ridge is too shallow then the injected current spreads out by electron-electron repulsion to cover a larger area, so the mode is larger and therefore less intense per unit current.

To determine the optimum depth, a series of 2 mm-long quantum dot lasers was made, each with a different ridge depth. Not even the deeper ridges showed any signs of higher-order modes, suggesting that the narrow ridges do indeed provide a large range of depths over which only the zero-order mode is supported. Ridges that were deeper than  $\sim 800$  nm displayed a degraded mode quality, spoiling the nice, clean profile, and making it “fuzzy” and larger, and presumably less effective for trapping. This optical argument suggests that the shallowest ridges should be used, but that is without the electrical data which is shown in Figure 3.11. There was no clear evidence of the deeper ridges having higher slope efficiencies (total power per unit current from both facets), but they did give lower threshold currents. A compromise was struck, therefore, between shallow etching for mode quality and deep etching for threshold current, and a depth of 750 nm was chosen, with 50 nm tolerance in the CAIBE etching.

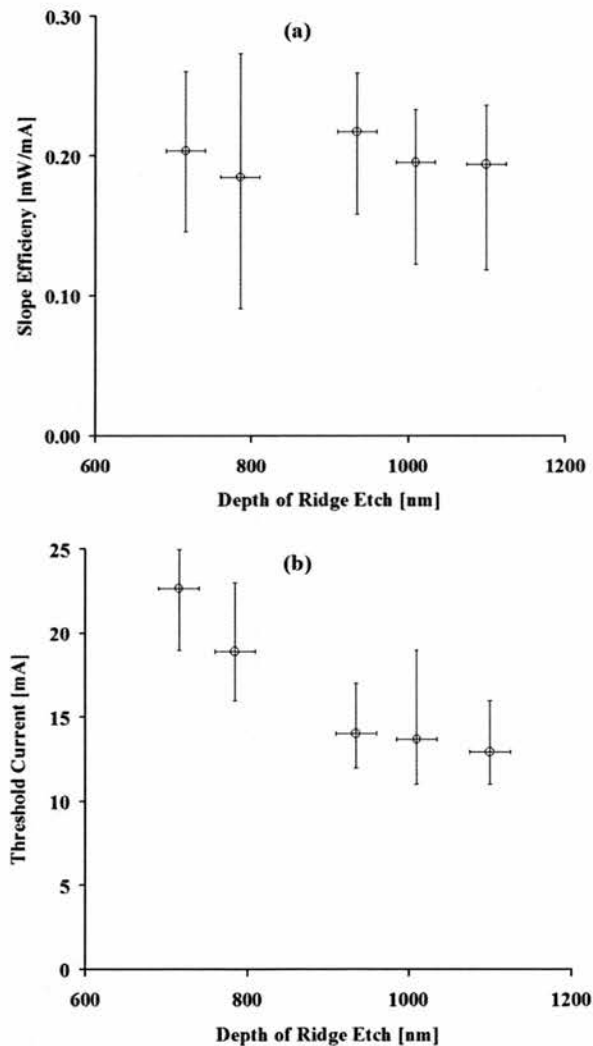


Figure 3.11: Effects of ridge depth upon (a) slope efficiency and (b) threshold current in quantum dot lasers.

## 3.4 Laser Performance

Having dealt with the ridge dimensions, it was necessary to optimise the length of the lasers, for which a background review is instructive. It considers four questions: Firstly, what is the relationship between the injected current and total optical power within the cavity? Secondly, what proportion of this power actually exits through either one of the facets to constitute either one of the two useful output beams? Thirdly, what cavity length gives the optimum performance? And, fourthly, into what proportions is the output power divided when it is emitted from facets of different reflectivities, as is the case with the device lasers? Questions two, three and four are answered with reference to experimental data, but question one is considered now from a simplified theoretical point of view.

### 3.4.1 Total Power within a Laser Cavity

The injected charges are most simply measured as a current,  $i$  [C s<sup>-1</sup>], which gives the total number of charges entering the laser per second. However, of these injected charges, only a fraction  $\eta_i i/e$ , where  $\eta_i$  is the internal quantum efficiency and  $e$  is the electronic charge, contributes to the upper state population each second. Of that, a certain amount is used up by processes that do not contribute to the laser mode; that is, non-radiative processes. The three main routes are spontaneous emission (in which a carrier falls across the bandgap without being stimulated to do so, and is hence not coherent with the beam), bimolecular recombination and Auger recombination. The cumulative effect of these processes is to drain a fraction of the upper-state carrier population. This is usually expressed as the radiative recombination time, which acts like a time constant in an exponential decay, giving the population after one second of decay. For simplicity in this discussion, these non-radiative processes are lumped in with the internal quantum efficiency, which now defines the fraction of injected carriers that both contribute to the upper state population, and then contribute one photon each to the laser mode. Absorption, scattering and other material losses act upon the laser mode all along the length of the laser, and facet losses act at each end of the cavity. The total number of photons that is used in the process of overcoming the losses, that is, in reaching threshold, is  $\eta_i i_{th}/e$ , where  $i_{th}$  is the current at threshold. If this number of carriers is sacrificed every second, then any excess carriers are free to constitute a useful laser mode. The average energy of the photons is  $h\nu$ , where  $\nu$  is the nominal emission frequency, giving the total optical power that is generated within the cavity as

$$P = \left( \frac{i - i_{th}}{e} \right) \eta_i h\nu \quad (3.7)$$

This is simply a mathematical version of the above discussion that tells of a linear variation of optical power with injected current, once threshold has been reached. It can be assumed that the output power from each facet will follow the same trend, and this is considered now using a model of a single round-trip of the cavity.

### 3.4.2 Model of a Single Round-Trip to Determine the Output Power

In determining the output power, the first step is to consider the population density as it moves through one round-trip of the cavity. At any point in the cavity, the various material losses and the gain are all proportional to the photon number density at that point. That is,

$$\frac{dN}{dz} = \text{gain} - \text{loss} = \Gamma g N(z) - \alpha N(z) \quad (3.8)$$

where the confinement factor,  $\Gamma$ , accounts for the fact that only part of the optical mode overlaps with, and extracts gain from, the active region. The gain and the material loss coefficients are  $g$  and  $\alpha$ , respectively, giving the fractional changes per unit length. It should be noted that these two coefficients vary with the carrier number density. More injected charges allow for more emission, and the variation can be approximated to a logarithmic relation, as shown in Figure 3.12(a), where  $N_c$  is the upper-state carrier concentration, and  $g_0$  and  $N_{cth}$  are the gain coefficient and upper state carrier concentration at threshold. Also, increasing the carrier number density affects the spectrum, as illustrated in Figure 3.12(b). Additional charges necessarily occupy higher energy levels, so their downward transitions across the bandgap are of higher energies, and the emitted photons have correspondingly shorter wavelengths, thus shifting the spectrum to shorter wavelengths, as shown.

Integration of Equation 3.8 over a distance  $\Delta z$  yields a new photon population of

$$N(z + \Delta z) = N(z) \exp((\Gamma g - \alpha) \Delta z) \quad (3.9)$$

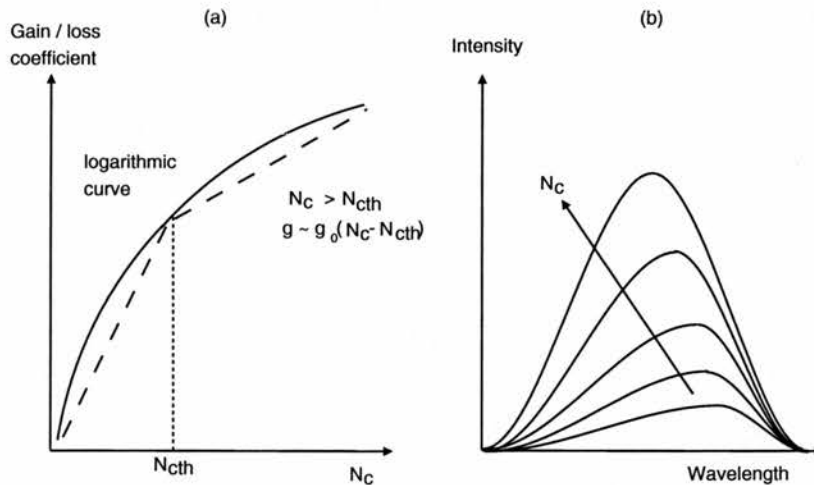


Figure 3.12: Effects of carrier concentration: (a) gain and loss coefficients both increase as more charges are injected; (b) the emission spectrum shifts to shorter wavelengths (higher energies) because the additional carriers occupy higher energy states and thus emit at higher energies.

This growth of the thin slice of photons as it travels through the material is illustrated in Figure 3.5. Such a slice, travelling from the left facet through a length  $L$  to the right facet, experiences a fractional growth in photon number density of  $\exp((\Gamma g - \alpha)L)$ . At the right end of the cavity only a fraction  $R_1$ , the facet reflectivity, is sent back into the cavity, and it then grows exponentially as it travels back towards the left end, where a fraction  $R_2$  is reflected back into the cavity. This sequence is shown in Figure 3.13 for the case of identical facets and for the general case of two different facets, with the actual values being those of the lasers used in the devices. The sequence is expressed mathematically as

$$\begin{aligned} \vec{N}(2L) &= \vec{N}(0) \exp((\Gamma g - \alpha)L) R_1 \exp((\Gamma g - \alpha)L) R_2 \\ &= \vec{N} R_1 R_2 \exp((\Gamma g - \alpha) 2L) \end{aligned} \tag{3.10}$$

A similar expression can be used to compare the number densities within the cavity just before each facet:

$$\vec{N}(L) = \vec{N}(2L) R_1 \exp((\Gamma g - \alpha)L) \tag{3.11}$$

Since the photons in the zero-order mode travel at close to normal incidence to the facets, the reflectivities follow the rule

$$R_{a \rightarrow b} = \left( \frac{n_a - n_b}{n_a + n_b} \right)^2 \tag{3.12}$$

where  $n_a$  and  $n_b$  are the refractive indices of media a and b, respectively. Under steady state operation

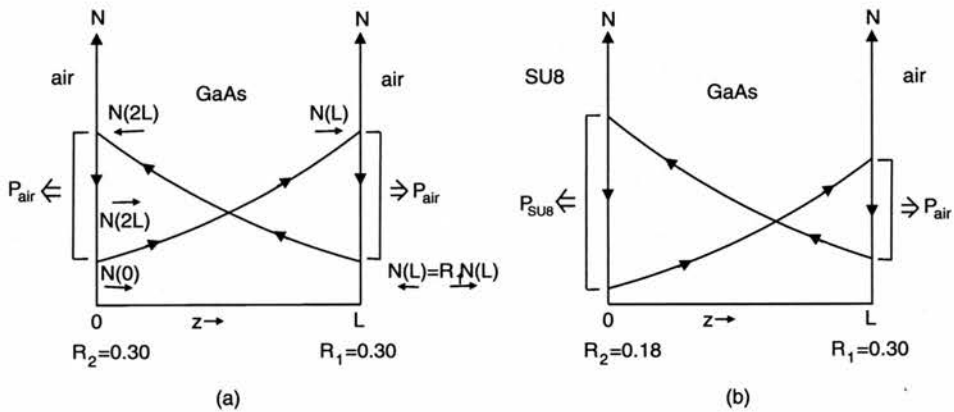


Figure 3.13: Photon population throughout a round trip of a laser cavity. The medium beyond a facet determines its reflectivity; that affects the amount of light that remains in the cavity, which in turn affects the population at the opposite facet. (a) Facets of equal reflectivities (air) have equal outputs; (b) facets of unequal reflectivities (air and SU8-2000) have unequal outputs.

the number density does not vary from one round-trip to the next, so  $\vec{N}(2L) = \vec{N}(0)$ , and Equation 3.10 can be re-arranged to give

$$\exp((\Gamma g - \alpha)L) = \frac{1}{\sqrt{R_1 R_2}} \quad (3.13)$$

which, in turn, can be re-arranged to give an expression that equates the total gain and total losses for one round-trip of the cavity:

$$\Gamma g L = \alpha L - \ln R \quad (3.14)$$

where  $R = \sqrt{R_1 R_2}$  is the combined facet reflectivity over one complete round-trip. It is conventional, and neater, to write the facet term as shown, although it is important to note that the term  $-\ln R$  is in fact positive, so it adds to the material loss, rather than subtracting from it. This equation has separated the losses into the two components, the material losses and the facet losses. It is only applicable over an integral number of round-trips, but it does show that the fraction of the number of photons that exits the cavity through either of the two facets in each round trip is

$$\frac{N_{\text{out}}}{N_{\text{total loss}}} = \frac{-\ln R}{\alpha L - \ln R} \quad (3.15)$$

which is a constant for any particular laser. These photon number densities can be translated into optical powers by multiplying by the volume of the optical mode and the energy of each photon,  $h\nu$ , so the ratio in Equation (3.15) is applicable to ratios of powers. So, combining Equations (3.7) and (3.15) the total power that exits from the cavity, via either facet, is

$$P_{\text{out}} = \left( \frac{i - i_{th}}{e} \right) \eta_i h\nu \left( \frac{-\ln R}{\alpha L - \ln R} \right) \quad (3.16)$$

The basic form of this equation was expected. The optical power only increases once the current has exceeded the threshold value, and it increases linearly thereafter, with a gradient known as the slope efficiency. This form is seen in data presented later in Figure 3.18. The power also depends upon the length, but in more than just the inverse proportion seen in Equation (3.16). Because the threshold current is also dependent upon the length, the optimisation of the length is more easily done empirically, but the theory is considered, briefly, first.

### 3.4.3 Optimum Cavity Length

Although a thorough derivation is not provided, it is instructive to consider the factors that affect the optimum length. This is determined by a combination of three factors: the threshold current, the slope efficiency and the maximum sustainable current. To start with, the maximum limit upon the current is a

consequence of Ohmic heating, so a longer laser has a higher tolerance and could be expected to give more power, but that alone is not sufficient to answer the question. To understand the role of the slope efficiency (that is, the useful optical output per unit current above threshold) and of threshold current, it is necessary to consider losses. Equation (3.14) shows that the material and facet losses are equal in a laser of length

$$L = -\frac{\ln R}{\alpha}. \quad (3.17)$$

The total material losses, which are proportional to the length, dominate in longer lasers, whilst the facet losses, which are independent of the length, dominate in shorter lasers. Figure 3.14 shows the relationships between cavity length and two parameters, and also the product of the two parameters. Under steady state operation, the intensity is the same after each round trip, so the gain and loss must be equal. That is, the net gain provided by the cavity per round-trip is

$$g_{\text{round trip}} = (\Gamma g - \alpha) 2L - \ln R \quad (3.18)$$

which is also proportional to the total power that is generated within the cavity; and the fraction of that power that exits the cavity as a useful output beam is given in Equation (3.15). That is, the total power in the cavity is proportional to the length, while the fraction that exits varies inversely with length. That is, short lasers emit a large fraction of their power into the useful output, but this is drawn from a small total power within the cavity. Conversely, long lasers emit a small fraction of their power into the useful output, but this is drawn from a larger total power. The optimum length is that which balances the two, generating a large amount of power within the cavity, whilst emitting a large fraction of it out through the facets, to give the largest total emitted power per unit current. This total emitted power is shown graphically in Figure 3.14 as the product of the two functions, which logically will have a clear maximum at a particular length called the optimum length. Unfortunately, this cannot be found without knowing the values of  $\alpha$ ,  $g$  and

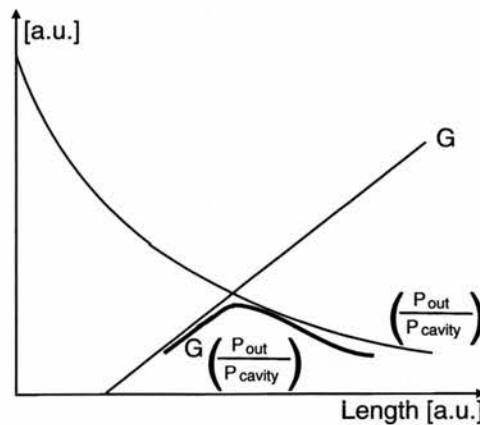


Figure 3.14: Reasons for the existence of an optimum cavity length. The round-trip gain varies linearly (above a certain point) with length, but the fraction that exits as a useful output beam varies inversely with length. The product (the total emitted power) therefore has a maximum at a certain length.

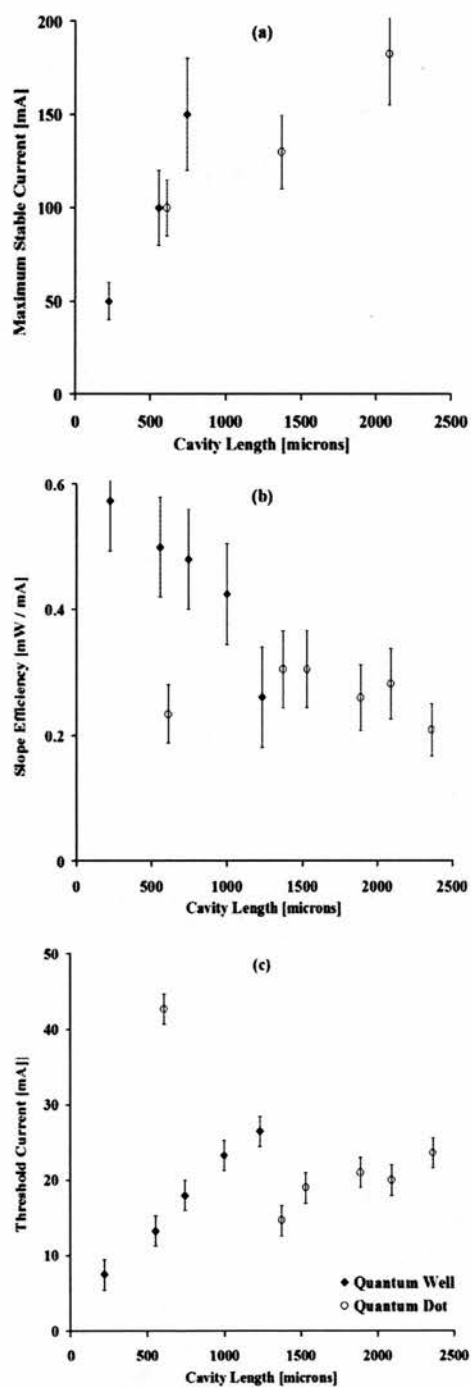


Figure 3.15: Effects of cavity length upon performance of quantum well and quantum dot lasers: (a) the maximum stable current increases with cavity length; (b) the slope efficiency seems to fall with increasing length, but peaks at a length of  $1500\ \mu\text{m}$  for the quantum dot material; (c) the threshold current for the quantum dot material has a minimum at  $1400\ \mu\text{m}$ .

$g_{\text{round trip}}$ , but it does show that the product has a maximum, and that there is therefore an optimum cavity length to be found. This trend is applicable both above, and at, threshold, so it is a valid guide to the effects of length upon both the slope efficiency and the threshold current.

The plots shown in Figure 3.15 were obtained from measurements of output power from one facet, for different lengths of lasers of double quantum well material and quantum dot material. The materials emitted at 980 nm and 1280 nm respectively, and had ridges of 5  $\mu\text{m}$  and 3  $\mu\text{m}$  width, respectively, and 500 nm and 750 nm depth, respectively, that both supported only a single transverse mode. As has been stated before, the main objective of these investigations was to maximise the available power, and this was affected by the three parameters that are seen in Figure 3.15: the threshold current, the slope efficiency and the maximum sustainable current. Looking at all three parameters, the optimum length was  $\sim 0.8$  mm for the quantum well material, and  $\sim 1.5$  mm for the quantum dot material.

#### 3.4.4 Additional Electrical Considerations

Whilst on the topic of length, it was assumed that the top contact pad provided an equipotential; that is, that it offered virtually no electrical resistance, allowing current to spread out uniformly along its length, starting from the probe. Figure 3.16 displays typical data for a quantum well laser that was probed at different points along its length. If the gold offered significant resistance then the current density would have been lower further from the probe, giving less gain at those points, and hence less overall output power from the laser. The larger the distance between the probe and the “measured facet”, the greater this effect would have been, and the lasers were generally probed at their mid points, so that any effects would cancel at each end, giving equal output powers. However, Figure 3.16 shows no such effect, confirming the

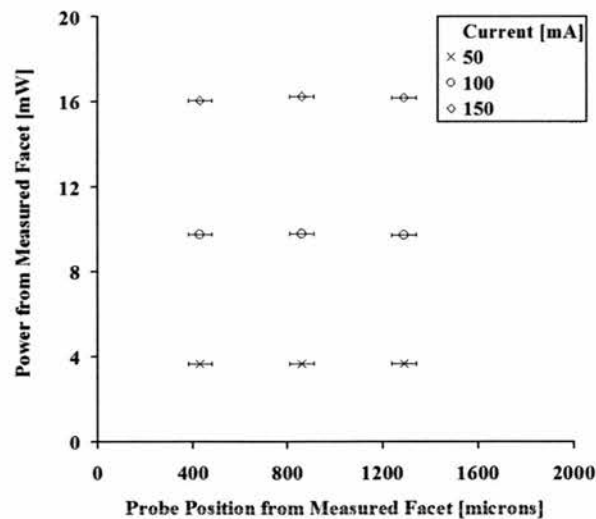


Figure 3.16: Effects of probe position upon output power for a 1700  $\mu\text{m}$ -long quantum dot laser. The power emitted from one facet does not depend upon the position of the electrical probe, suggesting that the gold contact pads do indeed provide equipotential surfaces.

assumption that the gold contacts had negligible resistances. It meant that the lasers could be probed at any point, which was useful when the fluidic chambers were in place, sometimes covering more than half of each laser.

The actual resistance of an entire laser was determined, as described in Section 3.2.2, by taking the inverse gradient of the sloped section of  $i - V$  graphs. The resistance varied with length, but was typically  $\sim 10 \Omega$  for 2 mm-long quantum dot lasers. The voltage at which meaningful current started to flow,  $V_{\text{on}}$ , was 0.9 V for quantum dot lasers of any length. These are good values for these electrical properties, but were only obtained by careful fabrication of lasers. Cleaning the GaAs surface with HCl before the evaporation and maintaining a low evaporation pressure made the most significant contributions. Also important was following the recipes, keeping the higher resistance materials (nickel and germanium) to a minimum, whilst depositing enough to allow each to perform its purpose.

Finally, there were optical interactions between facing lasers; these were generally small, having only a small effect upon the  $P - i$  performance of each laser, and they are discussed more in Section 4.8. However, there were electrical interactions within the GaAs via which lasers affected the  $i - V$  relationships of each other. The back contact of the device was earthed, and the substrate was highly doped (n type), so it conducted well and acted as an equipotential; a positive potential was applied to one point on the gold contact pad, which was so highly conductive that it was essentially an equipotential. In an individual laser, of the applied voltage, about 0.9-1.0 V was used up in overcoming the diode's bandgap, and most of any excess was used up in driving current through the diode to generate light. A little was dropped across the n-type substrate, giving a non zero potential beneath the diode. If however, another laser was switched on, the potential beneath it would create an equipotential in the n type material that would add to that beneath the first, reducing the potential difference that was dropped across that first diode, thus reducing the current that flowed through it. The same happened to the second laser, so both of them under-performed. In order to maintain a steady current, the voltage for each laser had to be increased by  $\sim 10\%$  for each additional laser that was operating at a comparable current. The interactions were found to be less significant for lasers that were separated by the deep trapping channel than for neighbours that were separated by only the shallow etch; this is because some more of the potential had been used up in the extra depth of GaAs, leaving less to affect the other diodes.

## 3.5 Power Estimation

### 3.5.1 Reductions in Measured Power

In order to insulate the electrical components from the water in the trapping channel, the channel was lined with SU8-2000 polymer. Therefore, the facing facets were coated, but the outer facets were not, giving them different reflectivities, and hence different output powers. In order to estimate how much power actually entered the trapping channel, it was necessary to determine the relationship between the powers emitted from the bare facet and from the facet that was coated with SU8-2000 polymer. But, it was important to first of all consider how all of the power measurements were affected by the factors that are illustrated in

Figure 3.17. It was found that, for lasers that had the same ridge dimensions and the same lengths, the power characteristics (threshold current and slope efficiency) were the same whether the facets had been cleaved or etched. Obviously the facets that faced into the channel had to be etched, but it was decided that the outer facets should also be etched, because it was more reliable than cleaving, which could easily go wrong, giving poor facets with low reflectivity, and sometimes virtually turning samples to dust. Etching the facets also kept them away from the edges of the device, offering them some protection from accidental touching and dropping. However, over this distance to the edge, the lower parts of the beam interacted with the excess GaAs, reducing the amount of power that was actually measured by the meter. The correction factor was determined by measuring the powers at certain currents from lasers that had 1.8 mm of excess GaAs beyond the cleaved facets, and then repeating the measurements once all but 45  $\mu\text{m}$  of the excess GaAs had been cleaved off. The results from nine lasers on a sample showed that the first set of readings (with more excess GaAs) were  $0.99 \pm 0.02$  times that of the second set of readings, giving a correction factor of  $1.01 \pm 0.02$ . That is, about 1% of the power is lost into the GaAs or scattered out of the beam. A collection lens was used to gather the light, and it was found that a x20 lens was much easier to align than were the higher power lenses. The power collected by higher power lenses tended towards a certain value,

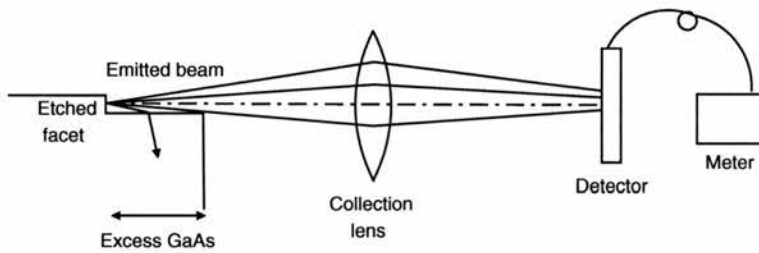


Figure 3.17: Reductions of measured power. Some of the power that is emitted from a facet does not reach the detector. The main losses occur at the edge of the GaAs and at the collection lens.

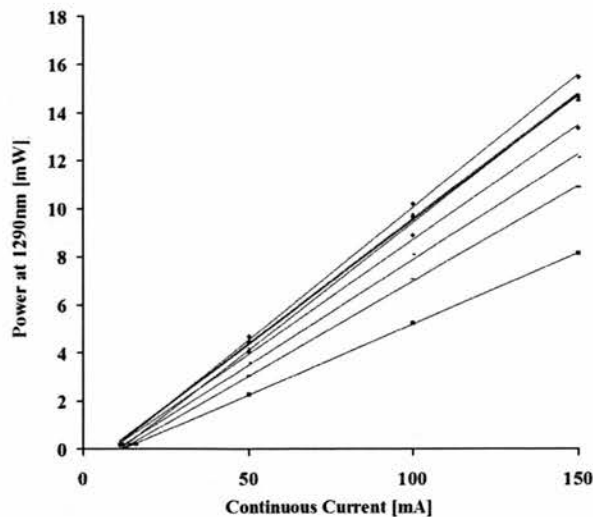


Figure 3.18: Power-current performance of nine quantum dot lasers. The majority of the lasers perform in roughly the same manner, with only one being especially poor.

and the x20 collection lens was found to collect  $87 \pm 1\%$  of that value, so a correction factor of  $1.15 \pm 0.01$  was included. The actual power meter was calibrated to give accurate readings, and the reading error was only  $\pm 0.005$  mW, which was insignificant compared to the uncertainties in the correction factors. Using these correction factors, the data shown in Figure 3.18 were obtained. They show the output powers of nine quantum well lasers of length 1.8 mm on a single chip, which follow the basic form predicted by Equation (3.16). The linear relationships were so reliable that they could be plotted from just three or four points. In terms of their  $P - i$  characteristics, four of the lasers are virtually indistinguishable from one another; two more are within  $\sim 5\%$  of them; only one is significantly poorer. This variation does mean, however, that the output power should be determined for each laser, individually.

When testing devices, the ideal arrangement was to use one power meter for each laser, giving continuous values for the power coming from the bare, outer facets. However, usually only one meter was available, so the next best method was to measure the  $P - i$  relationship for each laser's bare, outer facet, and then monitor the currents during the tests, from which the powers could be read via each laser's graph.

### 3.5.2 Power Emitted from Opposite Facets

In the case of a laser whose facets have the same reflectivities, the total output power in Equation (3.16) is split equally between the two output beams, but where the reflectivities differ from one another the output powers will differ also. Such is the case with the device lasers, for the facing facets were covered with electrically-insulating SU8-2000 polymer, whilst the outer facets were bare. The proportion that was emitted from each facet can be predicted by returning to Figure 3.13 and considering the ratio of the population densities that approach the facets, just before reflection, obtained using Equations (3.11) and (3.13):

$$\begin{aligned} \frac{\overleftarrow{N}(2L)}{\overrightarrow{N}(L)} &= R_1 \exp((\Gamma g - \alpha)L) \\ &= \frac{R_1}{\sqrt{R_1 R_2}} \\ &= \sqrt{\frac{R_1}{R_2}} \end{aligned} \quad (3.19)$$

The fraction of the population density that exits through one facet is simply  $1 - R_{a \rightarrow b}$  and the output power is proportional to that. So, the ratio of exiting powers is

$$\begin{aligned} \frac{P_2}{P_1} &= \frac{(1 - R_2) \overleftarrow{N}(2L)}{(1 - R_1) \overrightarrow{N}(L)} \\ &= \left( \frac{1 - R_2}{1 - R_1} \right) \sqrt{\frac{R_1}{R_2}} \end{aligned} \quad (3.20)$$

In the case of a laser in which one facet is coated with SU8-2000 polymer and the other has no coating, the values are found in the following manner. The refractive indices of SU8-2000 polymer and air are 1.55 and 1.00, respectively. The value for the laser material is less obvious, because it depends upon the proportions of the mode that reside in the GaAs core and the AlGaAs (60% Al) cladding; their refractive indices at 1290 nm are, respectively, 3.412 and 3.092 (according to luxpop.com). Putting these two different refractive indices into Equation (3.20) gives ratios of 1.79 and 1.85 for the GaAs and the AlGaAs (60% Al), respectively. If it is assumed that the majority of the mode's power resides in the core, then the value of 1.79 can be used, on the understanding that it might be slightly low.

To test this empirically, Figure 3.19 (a) shows typical examples of the  $P - i$  curves of the two different types of laser: one with two bare facets, and the other with one bare and one polymer-coated facet. Figure 3.19 (b) is a plot that compares such data for nine different lasers; it shows the powers measured from both facets of each laser both before and after a coating of SU8-2000 polymer was added to one facet (labelled "Facet 2") of each laser. The powers were measured for currents of 50 mA and 100 mA.

Of most interest is the comparison between the powers that are emitted from the opposite facets of lasers that have one bare and one coated facet; that is the case in the devices. As expected, an SU8-2000 coating on one facet created an imbalance in the output powers from the two facets; the coated facet emitted more power than its bare counterpart did. The data gives a ratio of  $1.63 \pm 0.09$  which is close to the predicted value of 1.79, and the discrepancy can be accounted for. Of the light that enters the SU8-2000 coating, a certain fraction is reflected at the polymer-fluid interface and therefore does not enter the trapping channel. However, the non-vertical slope of the SU8 2000 wall means that this reflected fraction does not efficiently feed back into the laser but is lost from the system. At near-normal incidence this fraction is 4.7% for air and 0.6% for water of refractive index 1.33, and the corrected ratios are 1.71 and 1.78, respectively. The experimental value of  $1.63 \pm 0.09$  agrees, within the margin of error, with the value of 1.71 for air, in which

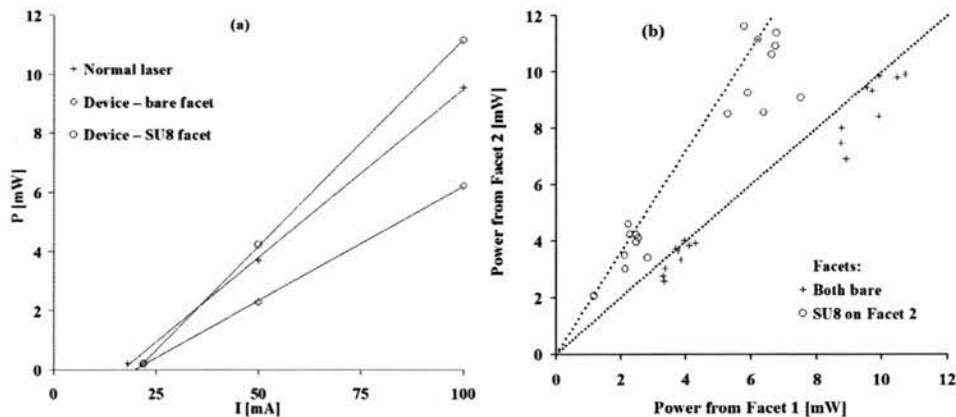


Figure 3.19: Comparison of powers emitted through opposite facets with and without SU8-2000 on Facet 2. (a)  $P - i$  curves for one facet of a typical laser before, and both facets after the addition of an SU8-2000 coating to Facet 2; clearly the polymer couples more light out of the cavity, but the total output power is reduced. (b) A plot of data for nine lasers comparing the power emitted from the opposite facets before and after the addition of the polymer to Facet 2. The dotted lines show the theoretical trends as predicted by Equation 3.20; that is, a slope of 1 for the identical facets, and a slope of 1.79 for the different facets.

the measurements were made. It is not possible to make accurate measurements with water beyond the SU8-2000, but the agreement in the case of air suggests a logical scheme. That is, the ratio of the measured and estimated values in air is  $1.63 / 1.71 = 0.953$ ; assuming that the same discrepancy exists for the case of water, then the measured value would be  $1.79 \times 0.953 = 1.67$ . The same percentage error ( $\pm 6\%$ ) is applied, giving the same actual error ( $\pm 0.09$ ). It is fortuitous that the powers are split in this manner, with the majority entering into the channel to contribute to the trapping. So, the overall correction factor combines the effects of the excess GaAs, the  $\times 20$  collection lens and the unequal reflectivities, to translate the power that is measured from the bare facet into the power that actually enters the trapping channel via the coated facet; its value is 1.94 and the cumulative percentage error is 8.3%.

In this work the lasers have been considered in isolation, but this was not the case in active devices, in which the dual-beam traps were generated by pairs of facing lasers. Some of the light from each laser would, inevitably, enter into the facing laser. This could cause destructive interference, reducing its output power, or it could assist the laser by adding constructively to the intensity of the mode. As will be seen in Section 4.8, the effect was found to be constructive, slightly increasing the output powers. For simplicity, though, that effect is not considered when estimating the optical power that enters the trapping channel, and the factor is left at 1.94.

Two other studies can be made using the data in Figure 3.19. Firstly, looking at all nine lasers when there was no polymer coating on either facet, the ratio of the power emitted from the opposite facets was  $1.00 \pm 0.10$ , which is in re-assuring agreement with preceding assumptions. Secondly, another useful comparison is that of the total powers (from both facets) from a laser that has one bare and one coated facet, and another laser that has two bare facets. If the two lasers are operating at the same current, then the ratio of the emitted powers is the same as the ratio of the slope efficiencies:

$$\frac{P_{s/a}}{P_{a/a}} = \left( \frac{i - i_{th(s/a)}}{i - i_{th(a/a)}} \right) \left( \frac{-\ln R_{s/a}}{-\ln R_{a/a}} \right) \left( \frac{\alpha L - R_{a/a}}{\alpha L - R_{s/a}} \right) \quad (3.21)$$

where the subscript  $a/a$  refers to a laser with air at both facets, and  $s/a$  denotes a laser that has air at one facet and SU8-2000 at the other. Clearly, for a useful comparison, the currents should be the same for any two data points that are compared. In this case, data is available for currents of 50 mA and 100 mA. The reflectivities are  $R_{s/a} = 0.20$  and  $R_{a/a} = 0.30$ , but the values of threshold currents must be determined empirically, and  $\alpha$  is still unknown, so the exact ratio cannot be predicted. The lower total reflectivities of the device lasers give them higher threshold currents, so the first term is less than one, as is the third term; the second is greater than one, so the overall ratio depends upon the exact values. The data that yielded Figure 3.19 was re-analysed to yield a ratio of  $0.88 \pm 0.05$ . So, at least for 1.8 mm-long quantum dot lasers, the addition of SU8-2000 polymer to one facet reduces the total output power. But the important fact about the polymer coating is that the majority of the available power enters into the channel, with only the minority exiting from the opposite end where it does not help with trapping. In fact, as is seen in Figure 3.19(a), the power that enters the coated channel is higher than it would have been for an uncoated channel; the ratio of the two is roughly  $1.09 \pm 0.08$ , yet another advantage of the polymer coating.

## 3.6 Final Considerations

### 3.6.1 Additional Effects of SU8-2000 Channel Lining

It has already been mentioned that the SU8-2000 lining has the effect of reflecting some of the light, preventing it from entering the channel, whilst also not sending it back into the laser. This avoids the risk of destructive interference within the cavity that would reduce its output power. Evidence of the truth of this assumption was seen by testing a set of lasers in which each had a different length of SU8-2000 beyond one facet. Although the lengths were not controlled on the wavelength scale, it was assumed that any destructive interference would be seen by the chance fabrication of a suitable length of SU8-2000. No such effects were seen, and so it was accepted that destructive interference need not be considered.

Another benefit of the SU8-2000 slope was that the transmitted light was refracted upwards (see Figure 3.20), lifting the position of the trap up slightly out of the channel, moving trapped particles away from the base, and hence reducing the chances of things adhering to the base. Also, the angled SU8-2000 slopes on facing lasers were likely to reduce the amount of light that entered each from the other, again reducing the chance of destructive interference. This was assumed to be approximately true, but some power did enter the facing lasers, as will be mentioned later on in the section about detection methods.

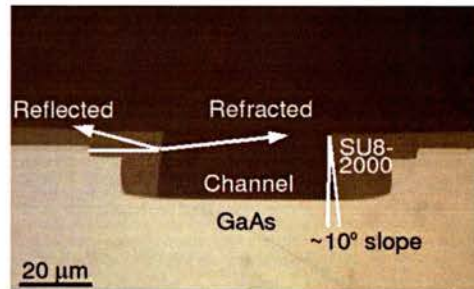


Figure 3.20: Additional optical effects of SU8-2000 lining. This cross-section through a channel shows that the angle of the SU8-2000 means that laser light is not reflected directly back into the laser and so probably does not affect the performance. It also means that the transmitted light is lifted slightly out of the channel, raising the position of the dual-beam trap.

### 3.6.2 Beam Divergence

Upon emerging from the tight confinement of the heterostructure of refractive index  $n$ , the maximum angle to the  $z$ -axis at which the mode diverges is

$$\theta_{\text{half}} = \frac{\lambda}{n\pi w_0} \quad (3.22)$$

where  $\theta_{\text{half}}$  is measured in radians, which is different for the horizontal and vertical directions. It requires estimates of the mode dimensions to the half maximum intensity points, which are based upon

computer simulations (*Whelan-Curtin (2002)*). A little refraction then occurs at the interface between the SU8-2000 and the water according to Snell's law. It can be shown that the change at the interface does not change the divergence angles by much. The main point is that divergence, especially in the vertical direction, serves to drastically reduce the intensity of the beam in the channel, reducing the power that is available for trapping.

## Chapter 4

# Optical Trapping Results

This Chapter presents the results that were obtained using integrated optical manipulation devices. They fall into two broad categories: physical properties and useful demonstrations. The physical responses show how the optical forces interact with submerged polymer spheres in the channel. The data analysis uses two pieces of information from elsewhere in the Thesis: firstly, the output power conversion factor from Chapter 3; and secondly, the intensity profile along the axis of a laser beam which is considered in the Appendix. The useful demonstrations show how the devices can be used to perform a number of the functions of conventional optical trapping systems. The combination of the two sets of results gives a broad picture of the reliability and usefulness of the devices. The Chapter begins by detailing how the system was set up, and also how measurements were made and uncertainties assessed. It then looks briefly at the drag forces that oppose the relative motion of particles and fluid, which is important for the analysis of the physical data. Thereafter comes said physical data, and the Chapter concludes with a discussion of the useful demonstrations.

### 4.1 Set-up, Measurements and Uncertainties

The device was mounted as shown in Figure 1.14, with micro manipulation probes providing the electrical connections to d.c. power supplies, and the capillaries and tubing providing the fluidic connections to the reservoir and the pump. The liquid was usually de-ionised water, in which polymer spheres were dispersed. The spheres were purchased from Duke Scientific, CA, U.S.A. Most were various sizes from the Certified Size Standard series (e.g. 4205A 5  $\mu\text{m}$  diameter), but some fluorescent spheres (e.g. G0300 3  $\mu\text{m}$ -diameter, green fluorescent) were used. Buffer solutions were used on the rare occasions on which biological cells were put into a device. For example, when SA2 cells (a mouse leukaemic cell line that was grown in the School of Biology at the University of St Andrews) were used, the buffer solution was RPMI 1640 supplemented with 10% foetal calf serum (FCS), penicillin (50  $\mu\text{g}$  / ml), streptomycin (50  $\mu\text{g}$  / ml) and glutamine (2 mM). After such events, the device was rinsed out with a 70% solution of ethanol in water in order to kill any remaining cells.

The fluid flow was initiated by an external peristaltic pump. The settings were not easily calibrated to flow speeds within the channel, so the particle flow speeds were calculated from plots of position against time, and the uncertainties in the speeds were taken to be the sum of the percentage uncertainties in the distance travelled and the time interval, as discussed later in this section.

All of the events were imaged through a long working distance objective, of magnification 20 or 50, depending upon what was available. The images were detected by a monochrome CCD camera, viewed on a 15" television monitor and recorded onto DVDs. The events were analysed by reviewing the DVD footage, moving through it frame by frame; there were 25 frames per second, corresponding to 0.04 s per frame, and giving an uncertainty of  $\pm 0.02$  s in each time measurement, and  $\pm 0.03$  s for each time interval. Positions were measured with a ruler taped to the monitor, giving an uncertainty of  $\pm 0.5$  mm in each measurement, and  $\pm 0.7$  mm in each distance between two positions. It was calibrated by measuring the on-screen sizes of the period of the laser ridges which had been precisely defined by the electron beam lithography that defined the optical mask, and was therefore reliable.

As discussed in Chapter 3, the powers entering the channel were calculated by monitoring the power emitted from the opposite facet and multiplying it by 1.94 to account for the measurement losses and the effects of the SU8 2000 polymer in the channel; the uncertainty in this factor was  $\pm 8.3\%$ . On the occasions on which the power was not measured directly, but rather the current was measured and converted to a power reading via a previously-plotted  $P - i$  graph, then other uncertainties had to be accounted for. The current was measured to the nearest 1 mA, giving an uncertainty of  $\pm 0.5$  mA for each value, and  $\pm 0.7$  mA for the useful current above threshold, which had to be converted to a percentage, and then added to the percentage uncertainty in the gradient of the  $P - i$  graph, and added to the  $\pm 8.3\%$  uncertainty in the conversion factor.

Uncertainties in the gradients of graphs were taken to be the averages of steepest and shallowest gradients; that is, the most extreme gradients that could be plotted through the error bars. The uncertainty was taken to be half of the difference between the extreme values. The best-fit gradients were also estimated, and they were generally close to these average values.

## 4.2 Drag Force

It is important to consider the drag forces that oppose the motion of the particles in fluids. Drag forces arise from the relative motion of the fluid and the particle. It is they that allow particles to be transported by fluid flows, the pressure and viscous forces between the fluid and the particle dragging the particles along. However, when motion is instigated by some other force, such as that from a laser beam, the drag forces oppose the motion of the particle. They are proportional to, and act in the opposite direction to, the velocity of the particle. The background is very complex, and no derivation is attempted here, but the basic story is as follows. If all of the forces that act within a fluid are taken into account, a set of nine equations are created. Assuming constant density and viscosity reduces them to the Navier-Stokes equation, which equates the inertial forces with the forces due to gravity, pressure and viscosity. It, however, is generally insoluble, but does have a solution when the inertial forces are neglected; that is, when the velocities are very small, which is the case in this work. Then, integrating the forces that act over the surface of a sphere

in a fluid gives the Stoke's force

$$F_D = 6\pi\eta r_s v \quad (4.1)$$

where  $r_s$  is the radius of the sphere,  $v$  is the relative velocity of the sphere with respect to the fluid, and  $\eta$  is the viscosity, which has a value of  $10^{-3} \text{ kg m}^{-1} \text{ s}^{-1}$  for water at room temperature. Two-thirds of this force is due to viscous shear drag as the fluid passes parallel to the surface of the sphere, and the remaining one-third is due to the pressure and is called the form drag. This total drag force is zero when a particle is at rest, but increases with the velocity. This significantly increases the complexity of some of the differential force equations, making it difficult to study some effects.

It should be noted that, in all of this work, the effects of fluid boundaries at the edges of the channels were ignored. This is acceptable because data was collected for particles that were in the open sea; had they flowed alongside solid features, then the attractive forces and subsequent reductions in flow speed would have required consideration.

### 4.3 Motion in a Single Beam

The simplest effect that could be studied was the motion of a sphere in a single laser beam, although the analysis was not the simplest. Having been brought close to the beam by means of an externally-generated fluid flow, the particle moved rapidly to the central axis of the beam under the influence of the radial gradient force. It did not oscillate around the central maximum of the beam, showing that the damping drag force is large compared to the radial restoring force. The motion to the centre was rapid and covered a distance of only a few microns; neither the spatial resolution nor the temporal resolution were sufficient to permit an accurate study of the radial forces.

The axial forces were more easily studied, having effects over much larger distances and longer time-scales. Once a test particle had been trapped, the fluid flow was switched off, so the particle remained on the beam's axis, held by the gradient force. The net axial force acting at any particular time was the difference between the axial force exerted by the laser and the drag force that opposes the motion, given in Equation (4.1). The work in the Appendix led to the approximation of the laser's axial force to the inverse square law, so that the net force acting on a sphere is

$$m \frac{d^2z}{dt^2} = \frac{A_s P B_z}{A_0(z + z_0)^2} - 6\pi\eta r_s \frac{dz}{dt} \quad (4.2)$$

where  $m$  is the mass of the sphere,  $z$  is the position of its centre with respect to the laser's facet, and  $P$  is the power in the beam. As defined in the Appendix,  $B_z$  is the conversion factor that relates the power to an axial force,  $A_s$  is the cross-sectional area of the sphere, and  $A_0$  and  $z_0$  are constants. This differential equation has no obvious analytical solution, but a few features of the solution can be deduced. Firstly, when the laser first acts upon the sphere immediately in front of the SU8-2000 coating of the laser's facet, the

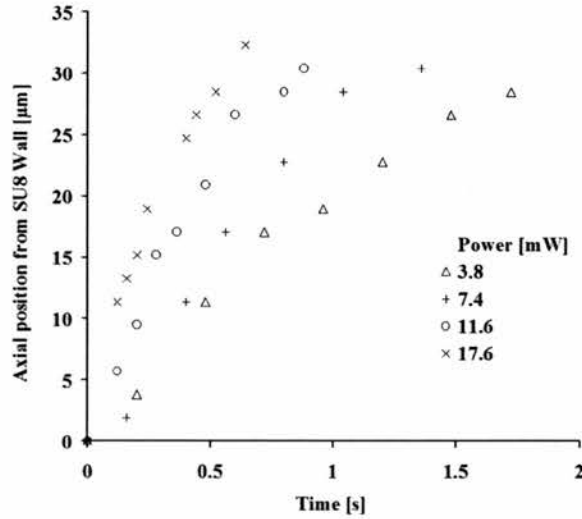


Figure 4.1: Data of motion of a polymer sphere in a single beam. The position of a  $5\ \mu\text{m}$  diameter polymer sphere from the SU8 2000 wall was plotted against time; higher beam powers give higher velocities. The velocity falls because the beams diverge and because of the opposing viscous drag.

velocity is small and the drag force is small; if it is assumed that the laser force is roughly constant over a short distance then the motion should follow a roughly parabolic form. Then, as the velocity and hence the drag force increase, the acceleration due to the laser is gradually cancelled until the net acceleration equals zero and the particle carries on at a terminal velocity. However, because the laser beam diverges, the force that it exerts wanes as the particle moves away from the facet, eventually being so weak that the drag force is unopposed and the sphere comes to rest. The higher the beam power, the faster the initial acceleration, the further the particle travels in a certain time, and the longer the particle's range. Figure 4.1 shows such data for a quantum dot laser that was used to push a  $5.010 \pm 0.035\ \mu\text{m}$ -diameter polymer sphere across a channel. The laser facets were spaced by  $73\ \mu\text{m}$ , with the SU8-2000 extending  $16\ \mu\text{m}$  from each facet, leaving a  $41\ \mu\text{m}$ -wide channel.

The data clearly demonstrate the effects that were expected. However, the velocities and the distances covered are insufficient to facilitate meaningful transport in a device. This could be addressed by using lensed facets to produce focused beams with higher intensities, but in the meantime this optical transport is suitable only for movement over a few tens of microns, such as in the case of sorting, where it was used to shunt particles into side channels as shown later in Figure 4.16.

#### 4.4 Equilibrium Position in a Dual-Beam Trap

A single divergent beam provides no axial confinement, but two such facing beams do, by simply providing an equilibrium point at which the opposing axial forces balance. Figure 4.2 shows images of two  $20\ \mu\text{m}$ -diameter polymer spheres moving across a channel as the relative powers in each of the beams of the dual-beam trap are varied, thus moving the equilibrium position. The situation is illustrated in Figure 4.3,

from which the net axial force acting upon a particle is

$$F_z = \frac{A_s B_z P_1}{A_0 \left(\frac{d}{2} - \bar{z} + z_0\right)^2} - \frac{A_s B_z P_2}{A_0 \left(\frac{d}{2} + \bar{z} + z_0\right)^2} \quad (4.3)$$

where  $P_1$  and  $P_2$  are the powers emitted by the two facing lasers,  $d$  is the separation of the lasers and  $\bar{z}$  is the displacement from the centre of the channel such that  $\bar{z} = z - d/2$ . The effects of the divergence angles are ignored. This net force is zero at the point

$$\bar{z} = \left(\frac{d}{2} + z_0\right) \left[ \frac{1 - \sqrt{\frac{P_1}{P_2}}}{1 + \sqrt{\frac{P_1}{P_2}}} \right] \quad (4.4)$$

which claims that the equilibrium position varies around the midpoint between the facets, which makes sense, and also that it is dependent upon the relative magnitudes of the laser powers, but not upon the

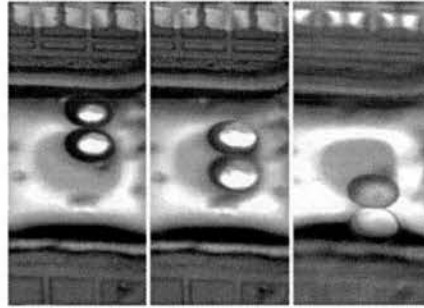


Figure 4.2: Stills from footage of motion in a dual beam trap. (left to right) Two  $20 \mu\text{m}$  diameter polymer spheres were held in a dual beam trap and moved across the channel by varying the relative beam powers.

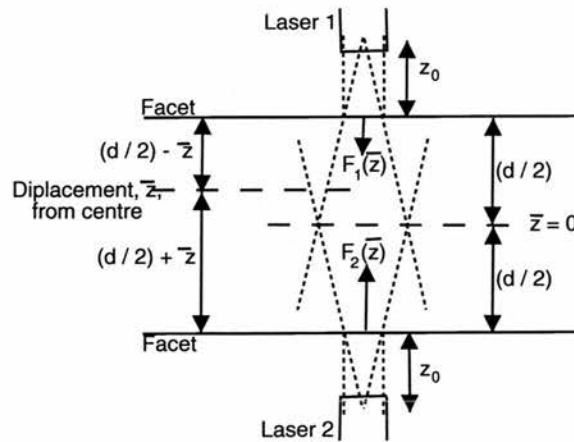


Figure 4.3: Forces that determine the equilibrium position in a dual-beam trap. The two laser beams exert opposing forces across the channel; the point at which the forces are equal is determined by the relative beam powers and the width of the channel.

absolute values. It also claims that the equilibrium position, as measured from the centre of the channel, is scaled by the separation of the lasers. That is, the greater the facet separation, the greater will be the displacement induced by a set change in the ratio of the beam powers. The data in Figure 4.4(a) show the variation of equilibrium position with the difference between the beam powers. The measurements were made in the same device in which the data for the single beam was collected. For each data point, the powers were set and the sphere was allowed to move and then come to rest before the position was measured. Two data sets are included, one for a  $2.013 \pm 0.025 \mu\text{m}$ -diameter polymer sphere for which the right laser was set to  $7.5 \pm 0.5 \text{ mW}$  and the left laser's power was varied; and the other data set is for a  $3 \mu\text{m}$ -diameter polymer sphere for which the left laser was set to  $14.5 \pm 0.5 \text{ mW}$  and the right laser's power was varied. The data are arranged such that the directions of the motion follow the definitions in Figure 4.3; that is, if  $P_1 < P_2$ , and hence  $P_1 - P_2 < 0$ , then the equilibrium position is negative.

Logically, the size of the test particle can have no effect upon the equilibrium position that exists even in the absence of the particle. Therefore, these two data sets can be used to compare other parameters, namely the absolute beam powers. Clearly, the equilibrium position is indeed independent of the absolute powers, but is affected by the relative powers. Analysing the data shows, for instance, power ratios of  $2/3$  and  $3/2$  give identical, but opposite, equilibrium positions.

The plot in Figure 4.4(b) allows comparison between the data and the theory of Equation (4.4). The horizontal axis uses the simplification  $P^* = \sqrt{P_1/P_2}$ . Having taken absolute values for both variables, all of the data falls in one quadrant of a graph, as shown in Figure 4.4(b), allowing an overall comparison of data, no matter from which side of the channel it came. The data compares well with the theoretical model of Equation (4.4). Different values of  $z_0$  show the effect of different possible beam profiles, as discussed in the Appendix. The plot would seem to suggest that a variety of possible beam profiles all give good predictions of the results, and that it is not necessary to deduce the precise form of the beam profile.

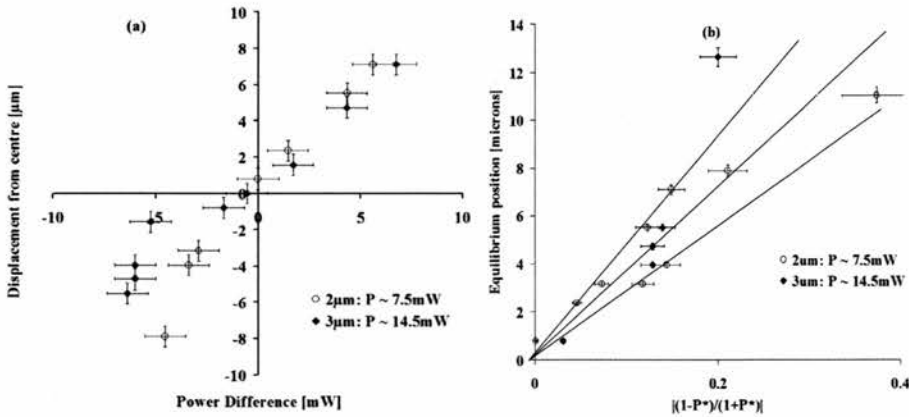


Figure 4.4: Data for the equilibrium position in a dual-beam trap. (a) The equilibrium position was plotted against the difference between the beam powers for two different power regimes. (b) The data compares favourably with the predictions of Equation 4.4. The different lines ( $z_0 = +10$  (top),  $0$  (middle) and  $-10$  (bottom)) show that varying the beam spreading model still gives realistic predictions.

## 4.5 Axial Restoring Force in a Dual-Beam Trap: Recoil

Whereas in the previous section, the interest was in the equilibrium position of the sphere, the interest is now in the motion of the sphere between equilibrium positions, and follows the work of *Constable et al. (1993)* on the Fibre Optic Trap. If a particle is held in a dual-beam trap, as in the previous section, at position  $\bar{z}_1$  and the power from one laser is reduced, the particle will move to the new equilibrium position,  $\bar{z}_2$ . If the power is suddenly restored to its original value, then the particle will move back to  $\bar{z}_1$  under the influence of the newly-restored laser beam. The other beam will oppose that motion; if that was the entire story then simple harmonic motion would result, with oscillations about  $\bar{z}_1$ , as if the particle was attached to a spring that was anchored at  $\bar{z}_1$  whose strength was a combination of the two laser powers. However, the Stoke's drag serves to damp the oscillations to the extent that none occur, and the particle comes to rest the first time that it reaches  $\bar{z}_1$ . This damped simple harmonic motion can be modelled by using Equation (4.3), and setting  $\bar{z}_1$  to be at the centre of the channel; that is, at  $\bar{z} = 0$ . The denominator of each force term can be re-written as

$$\left(\frac{d+2z_0}{2}\right)^{-2} \left(1 - \frac{2\bar{z}}{d+2z_0}\right)^{-2} \quad (4.5)$$

and, when the condition

$$\left|\frac{2\bar{z}}{d+2z_0}\right| \ll 1 \quad (4.6)$$

is satisfied, the binomial expansion can be applied to give

$$\left(\frac{d+2z_0}{2}\right)^{-2} \left(1 - \frac{2\bar{z}}{d+2z_0}\right)^{-2} \approx \left(\frac{d+2z_0}{2}\right)^{-2} \left(1 - 2\left(-\frac{2\bar{z}}{d+2z_0}\right)\right) \quad (4.7)$$

When these expressions are inserted into Equation (4.3) for the net force, and the powers are set to  $P_1 = P_2 = P$ , then the constant terms cancel, yielding a linear relationship between the restoring force and the displacement from the equilibrium position

$$F_z \approx \left(\frac{4PA_sB_z}{A_0(d+2z_0)^3}\right) \bar{z} \quad (4.8)$$

This linear relationship is the basis of simple harmonic motion, so the analogy can be continued by trying to obtain experimental values for the spring constant,  $k$ , where  $F = -k\bar{z}$ . Equating this expression with Equation (4.8) gives a relationship between  $k$  and the parameters in the model:

$$k = \frac{4B_zA_sP}{A_0\left(\frac{d}{2} + z_0\right)^3} \quad (4.9)$$

Substituting in the values from the Appendix yields a prediction of  $k = 5.19 \times 10^{-9}$  N/m per 1 mW in each beam of the device for a  $2.1 \mu\text{m}$  diameter sphere, which was used in the experiments. This compares favourably with experimental  $k$ -values obtained below, as will be seen in Figure 4.6, shortly.

Figure 4.5 shows an example of the motion of  $2.400 \pm 0.030 \mu\text{m}$ -diameter polymer spheres during their return to the midpoint between the facets. In this device, the facets were spaced by  $75 \mu\text{m}$ ; the SU8-2000 coating was asymmetric, with  $24 \mu\text{m}$  beyond the left facet and  $20 \mu\text{m}$  beyond the right facet, leaving a channel of width  $31 \mu\text{m}$ . The measurements were made with respect to the midpoint between the GaAs facets, not the midpoint of the SU8 2000 channel. The laser powers were balanced, then one was switched off completely, allowing the sphere to move to the edge, touching the SU8-2000 wall, whereupon the laser power was instantaneously restored to its original level, which occurs at time  $t=0$  s on the graph in Figure 4.5. Now, in order to extract a value for the spring constant, a little logical sleight of hand is required. If the damping force was small then the particle would retain some velocity upon reaching the equilibrium position, and the restoring force would carry it beyond that point. However, the particle was not carried beyond the equilibrium position, which means that the damping force had completely removed all of its velocity by the time it reached that point. For the forces to be so perfectly matched, the damping force must have matched the restoring force at each point in the motion, constantly cancelling out any additional acceleration that the restoring force imparted to the sphere; that is

$$-k\bar{z} = 6\pi\eta r_s \frac{d\bar{z}}{dt} \quad (4.10)$$

which can be integrated to yield

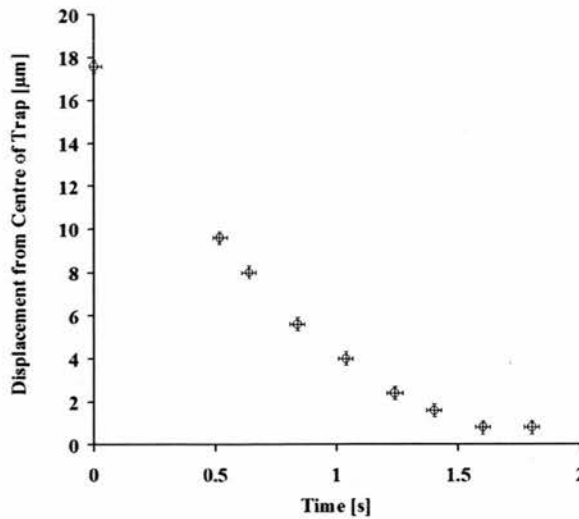


Figure 4.5: Particle motion due to axial restoring force of a dual beam trap. A  $2.1 \mu\text{m}$  diameter polymer sphere was displaced to one side of the trap by reducing the power in that laser. The original power was then restored, instantaneously, causing the sphere to re-coil back to the centre of the trap.

$$\bar{z} = \bar{z}_0 \exp\left(-\frac{kt}{6\pi\eta r_s}\right) \quad (4.11)$$

where  $\bar{z}_0$  is the position of the SU8 wall. This exponential form is reflected in the form of the data in Figure 4.5. However, the two should only be compared with certain caveats in mind. Firstly, the motion is only simple harmonic when the condition in Equation (4.6) is satisfied; that is, for displacements of less than  $\sim 0.1d/2$ . And, secondly, the assumption that the drag force exactly cancels the restoring force at all points is obviously not the case early on in the motion when the sphere is accelerated rapidly from rest. However, the exponential form of the data suggests that the simple harmonic approximation is appropriate, even towards the edges of the channel. Equation (4.11) can be re-arranged to give

$$k = -\frac{6\pi\eta r_s}{t} \ln\left(\frac{\bar{z}}{\bar{z}_0}\right) \quad (4.12)$$

where  $\bar{z}_0$  is the displacement at  $t = 0$ . This prediction can then be compared with the data by plotting  $\ln(\bar{z}/\bar{z}_0)$  against  $t/(6\pi\eta r_s)$ , and using the gradient to determine the spring constant,  $k$ .

Figure 4.6 summarises the data for different beam powers; in each case, the equilibrium position was at the centre of the channel, showing that the beam powers were equal. The data show a general increase in spring constant with beam power, which makes sense, and which fall within the range predicted by Equation (4.9). In addition, the values can be compared with the work of *Constable et al. (1993)* which gave a value of  $k = 1.72 \times 10^{-8} \text{ N m}^{-1}$  for a  $2.98 \mu\text{m}$  diameter polymer sphere in a fibre trap with 7 mW per beam and a fibre separation of  $200 \mu\text{m}$ .

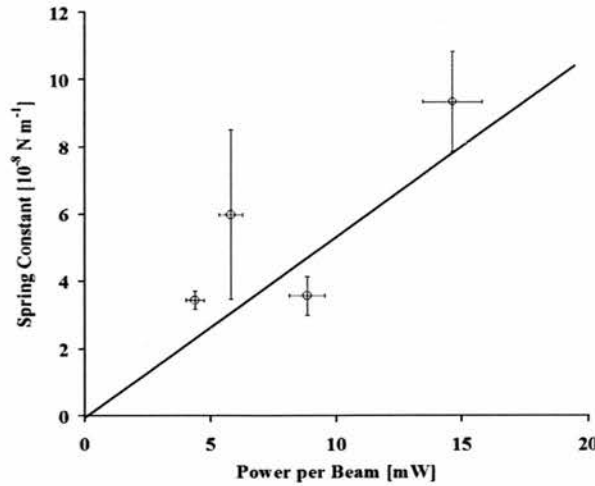


Figure 4.6: Values of spring constant for different beam powers acting upon a  $2.4 \mu\text{m}$  polymer sphere in a dual-beam trap. The strength of the spring constant increases with beam power, as expected. The solid line is the prediction from the model, which is a good fit.

## 4.6 Transverse Q-value

The final mechanical property to be investigated was the so called Q factor of the trap. As was discussed earlier, it is the proportion of the available photon momentum in the laser beam that is actually translated, per second, into a force upon the particle. It can be defined for various different configurations. For instance, in a single-beam tweezer trap, the symmetric radial trapping force has an associated Q-factor, and the axial trapping force has a different Q-factor. They represent the fact that different amounts of momentum are transferred to the different directions of motion. In the case of a dual-beam trap, there is no axial Q-factor, because the facets obstruct motion out of the optical field, but there is a radial Q factor. The most relevant Q-factor is that for motion along the channel in the direction of the fluid flow; this transverse Q-factor shows how effectively the trap can hold particles against the flow.

Following from the definitions in Equations (1.2) and (4.1), the forces are considered in Figure 4.7. The drag force,  $F_D(v)$ , is the result of the relative motion of the fluid and the particle, so a fluid flow will tend to accelerate a submerged particle until its speed equals that of the fluid, at which point the net force is zero, no more acceleration occurs and the particle continues at the fluid's flow speed. However, as in the situation that is illustrated in Figure 4.7, if superior optical forces,  $F_L(x)$ , are acting against the fluid flow, then the said flow will only serve to displace the particle to the point at which the drag force balances the restoring force. The flow will manage to dislodge the particle from the optical trap only if the drag force exceeds the restoring force; and the drag force can be easily controlled by simply varying the flow speed via the external pump. When the flow speed reaches the critical escape velocity,  $v_{esc}$ , the drag force slightly exceeds the opposing trapping force; that is, to a very close approximation,

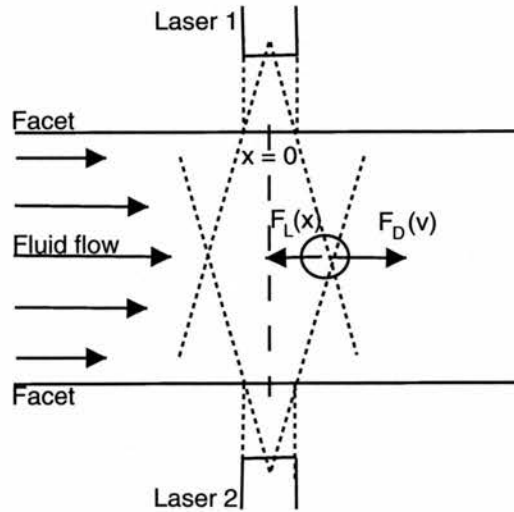


Figure 4.7: Forces that determine transverse Q-factor of a dual-beam trap. The gradient forces tend to draw particles towards the beams' axes, but this is opposed by the viscous drag force of the fluid that flows along the channel, perpendicular to the beams' axes.

$$\frac{Q_r P n_f}{c} = 6\pi\eta r_s v_{esc} \quad (4.13)$$

Re-arranging this gives a value for the radial (or transverse) Q-factor,  $Q_r$ , of

$$Q_r = \frac{6\pi\eta c}{n_f} \left(\frac{v_{esc}}{P}\right) r_s = 4.252 \times 10^{-3} \left(\frac{v_{esc}}{P}\right) r_s \quad (4.14)$$

where the value  $4.252 \times 10^{-3}$  translates powers in mW, speeds in  $\mu\text{m s}^{-1}$  and radii in  $\mu\text{m}$  into the transverse Q-factor. The power that was in both beams added together, and the sphere radii were given in the manufacturer's data sheets. The escape speeds were determined by moving frame-by-frame through DVD footage of the escape events. Examples of the motion of spheres after escaping from a trap are shown in Figure 4.8, from which a few things can be noted. First of all, some of the spheres were clearly not on the trap's axis when they began to accelerate; this illustrates the radial extent of the trap, but the resolution of the footage was insufficient to allow accurate measurements of this with respect to beam power or other parameters with which it is likely to vary. Secondly, once it had escaped, the acceleration of a sphere was rapid, but it decreased as its speed increased, as was to be expected with the effects of the opposing drag force. Thirdly, once the acceleration had ended, the particles flowed at constant speeds, which were measured and taken to be the fluid speeds that had facilitated the escapes.

A variety of experiments was conducted, the results of which are shown in Figure 4.9 as plots of escape speed versus the power in each beam, which must be doubled for use in Equation 4.14. Firstly, polymer spheres of three different sizes were used in a channel of a certain width, in order to see if there was indeed any variation of Q-factor with particle radius. Secondly, the separation of the laser facets was reduced, in

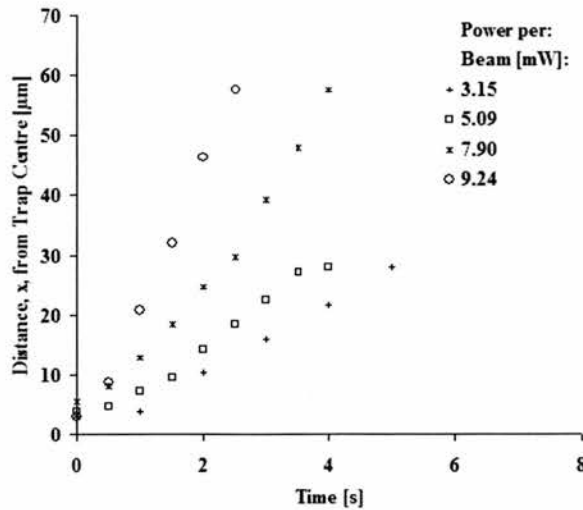


Figure 4.8: Data for motion of a  $2 \mu\text{m}$  polymer sphere as it escapes from a dual-beam trap of facet separation  $73 \mu\text{m}$ . After an initial burst of acceleration, the speed settles to the constant value of the fluid that dragged it out of the trap. Clearly, higher beam powers create stronger traps that can resist higher flow speeds.

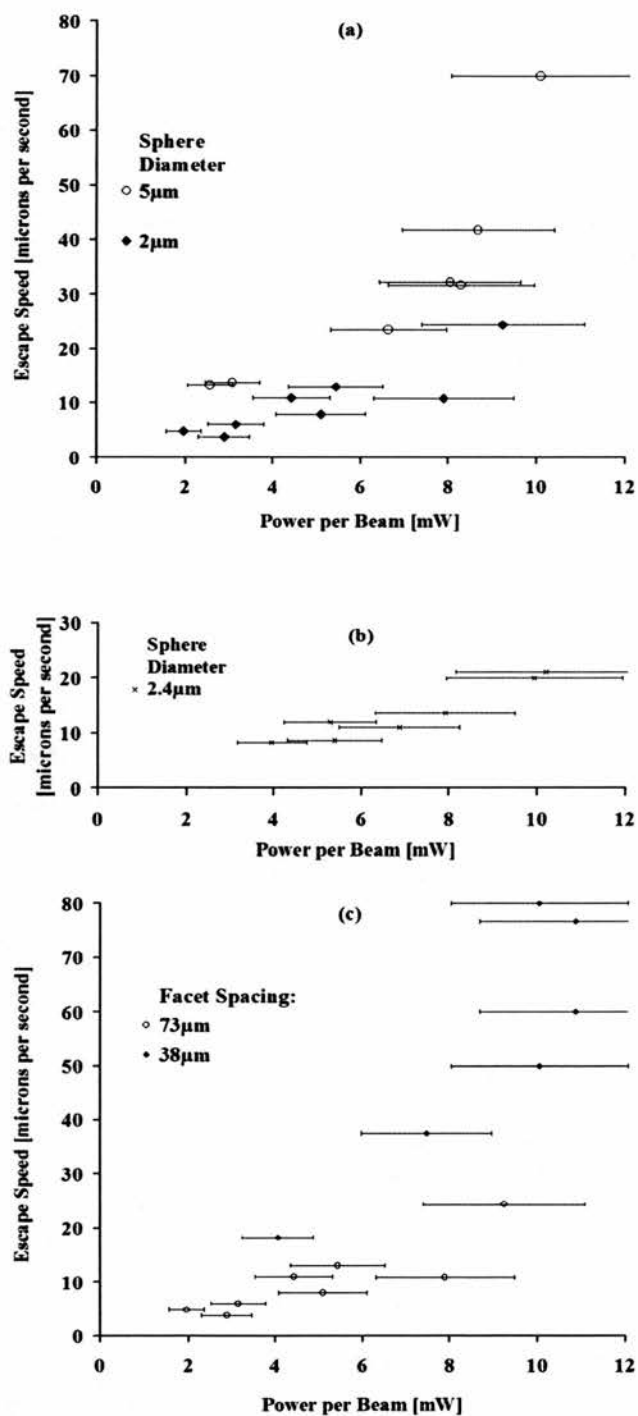


Figure 4.9: Data for escape speeds of spheres from dual-beam traps: (a) 73  $\mu\text{m}$  facet spacing, 2  $\mu\text{m}$  and 5  $\mu\text{m}$ -diameter polymer spheres; (b) 75  $\mu\text{m}$  facet separation, 2.4  $\mu\text{m}$ -diameter polymer spheres; (c) 38  $\mu\text{m}$  and 73  $\mu\text{m}$  facet separation, 2  $\mu\text{m}$ -diameter polymer spheres.

the assumption that the reduction in the distance over which the beams diverge would increase the intensity at the mid-point between the facets, and thus increase the power that was harnessed by the spheres. In each case, the beam powers were balanced so that the trapped sphere was located at the midpoint; sometimes a sphere moved a small distance towards one laser before escaping, and this might have led to some of the scatter in the data points. Also, in each case, the pump's flow speed was increased in small increments, and the increase was stopped immediately when the particle escaped, so that the measured speed and the actual critical escape speed were as close to one another as possible. There may have been some lag between the flow speed reaching the critical escape value and the sphere actually escaping, but the rate was increased slowly, so it was assumed that any lag was small, and that the measured flow speed gave a reliable value for the escape speed.

Although the scatter and the error bars are large, there are clear trends in the data. Firstly, the escape speed is indeed proportional to the optical power, and the gradient can be used in Equation (4.14) to calculate the Q-factors, remembering to double the power per beam to account for both lasers. Spheres of diameters  $5.010 \pm 0.035 \mu\text{m}$  and  $2.013 \pm 0.025 \mu\text{m}$  were used in the device that featured in Sections 4.3 and 4.4, which had a facet separation of  $73 \pm 1 \mu\text{m}$ . The Q-factors of the two spheres were  $0.0303 \pm 0.0148$  and  $0.0046 \pm 0.0022$  respectively. This shows that larger spheres do indeed have higher Q-values, because their larger cross-sectional areas gather more of the beam's power. Spheres of diameter  $2.400 \pm 0.0030 \mu\text{m}$  were used in the device that featured in Section 4.5, which had a facet separation of  $75 \pm 1 \mu\text{m}$ . The Q-value was  $0.0051 \pm 0.0015$ . Assuming that the effects of the small difference in facet separation were unimportant, then comparison with the data for the  $2.013 \pm 0.025 \mu\text{m}$  spheres in the  $73 \pm 1 \mu\text{m}$  trap shows that there is a subtle difference between the Q-factors for spheres of slightly different sizes. The second main experiment was conducted using polymer spheres of diameter  $2.013 \pm 0.025 \mu\text{m}$  in a device whose facet separation was  $38 \pm 1 \mu\text{m}$ . The Q-value for the narrower channel was  $0.0176 \pm 0.0069$ . So, a narrower channel does indeed increase the Q-factor, because the particles are closer to both facets, where the intensities are higher, so they gather more power over their surfaces.

## 4.7 Conclusions of Physical Data

The above studies are useful starting points when designing integrated devices for practical applications. If such an application uses polymer spheres, then the work is especially useful. Indeed, some biological testing procedures begin with the chemical bonding of polymer spheres to biological matter, such as cells or chromosomes. These spheres can be fluorescently labelled, for the purposes of tracking the position of the biological material, or they can be used as handles for holding otherwise tricky objects. The above data gives information about the flow speeds that can be resisted by traps, which would determine the throughput of any device. It also shows how quickly particles can be ejected from the main channel by a single beam, which might place another limitation upon the flow speed. For applications in which objects other than spheres are trapped, further studies will be required; but it can be predicted that reliably trapping and moving cells (with their low refractive index contrasts) will require higher intensities than are currently available. That said, mammalian cells have been manipulated, as will be discussed shortly, but only after a review of the various detection methods that have been employed in the devices.

## 4.8 Detection

The data in the preceding sections were collected via an external microscope, which is the simplest and most versatile means of extracting information from the devices. As an example of its versatility, by simply coupling the output of a blue laser diode emitting at 411 nm into the microscope objective, and then, in reverse, coupling the light collected by the objective into a spectrometer, the emitted 485 nm light from a trapped fluorescent polymer sphere was detected, as seen in Figure 4.10(a). This is directly applicable to the afore mentioned work in which spheres are used to tag biological objects. It could be used as a means of counting particles, and even of counting the populations of a number of species bearing different fluorescent tags, before triggering a trap to hold a desired particle or a single laser to push it into a collection chamber. The issues of bleaching and damage should be kept in mind, as out-lined in Chapter 1.

Fluorescence can also be used for positioning particles within a trap, as illustrated in Figure 4.10(b) which shows both the fluorescence signal and the variation of its peak value with distance from the centre of the trap, where the objective was positioned, as the relative beam powers were altered. This could be used to position desirable particles for further analysis or treatment, such as Raman spectroscopy or

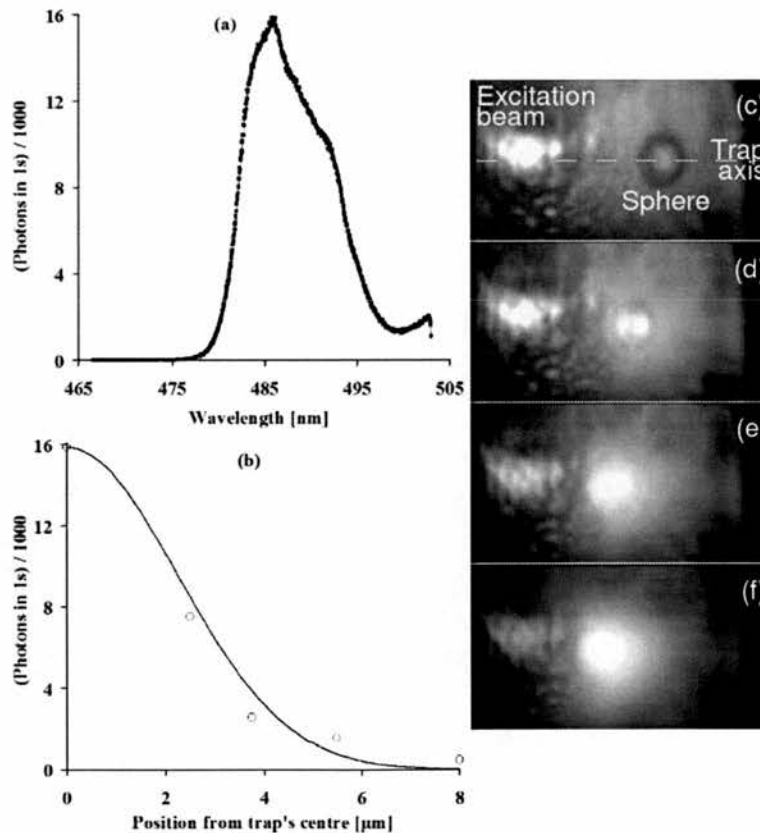


Figure 4.10: Fluorescence signal from a sphere in a dual beam trap: (a) emission spectra; (b) intensity at 485 nm at different transverse displacements; (c,d,e,f) images of the sphere at different transverse positions.

photoporation. And all of this could be done without the need for any “visual” monitoring, or even human control.

Two other methods of detection were successfully demonstrated, and they had the advantage of utilising the very lasers that are on the device. Both were conducted using the device from previous sections, whose facets were spaced by  $38\ \mu\text{m}$ . The first method involved monitoring the power in one laser as particles were passed between two facing, operating lasers. It was found that the power emitted from the outer facet of the laser fell when spheres were held in the trap, and rose again when the spheres were released. This suggests that the facing lasers do actually feed power into one another, thus increasing their mode powers, and that the presence of a trapped particle blocks or diverts some or all of that power away from the opposite laser. The size of the power drop seemed to depend upon the sizes of the currents, as seen in Figure 4.11(a); higher currents gave smaller power drops. It is plausible that the higher optical intensities that were generated by higher currents meant that there was more power at the edges of the beams where it was not obstructed by the particles, and so the particles had less of an influence upon the interaction of the lasers. The power drops did depend upon the size of the obstacle: over a series of events with both lasers set to  $60 \pm 1\ \text{mA}$ , a single  $2\ \mu\text{m}$ -diameter polymer sphere caused the power to drop by  $0.31 \pm 0.11\ \text{mW}$ , whilst a pair of such spheres caused a reduction of  $0.55 \pm 0.03\ \text{mW}$ . An accurate study of the power changes caused by particles of different sizes, shapes or compositions could allow the selection of particles based upon some such physical property. This would require only an external power meter.

The second integrated detection technique was the use of a reverse biased laser diode as a photodetector. Rather than using a forward bias to inject carriers into the junction where they recombine to emit light, this arrangement draws carriers away from the junction, setting up a stronger potential. Any photons incident upon the junction can be absorbed, promoting an electron over the bandgap and into the conduction band, where it is immediately drawn away by the increased potential, as its corresponding hole goes in the opposite direction, both of them constituting an electrical current. Because of the high beam divergence

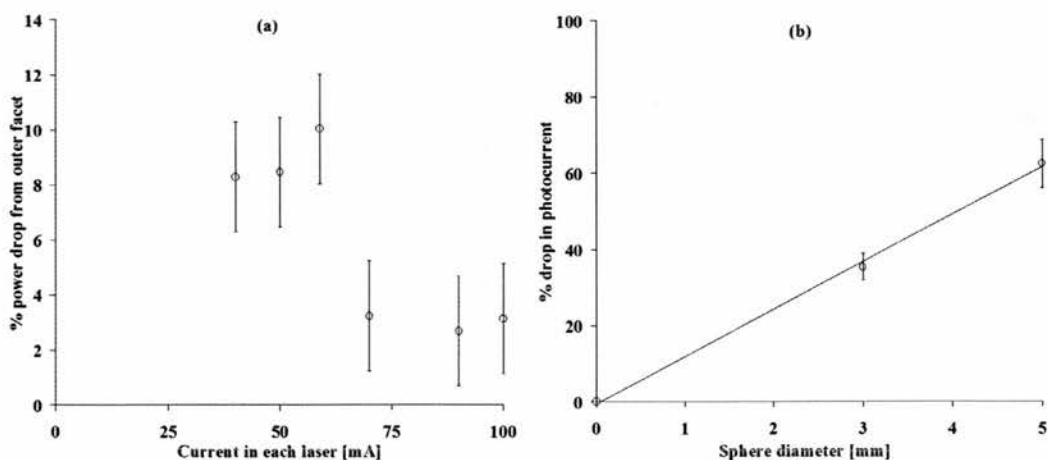


Figure 4.11: Data for integrated detection methods: (a) the power emitted by a laser falls when a particle blocks the beam from the facing laser; (b) the photocurrent created in a reverse bias laser falls when a particle blocks the beam from the facing laser.

and the resulting low intensities at the far side of the channel, these photocurrents were small, and care was required when measuring them, especially because of all of the other larger currents that flowed through the same piece of GaAs material. The data is shown in Figure 4.11(b). It was found that a laser that emitted  $2.63 \pm 0.21$  mW into the channel generated a photocurrent of  $160 \pm 10$   $\mu$ A in the facing, reverse-biased diode. The intervention of a 5  $\mu$ m-diameter polymer sphere into the beam, which pushed the sphere to the opposite side of the channel, reduced this to  $60 \pm 10$   $\mu$ A, a reduction of about 63%. The current into the lasing diode then dropped slightly, so that the photocurrent in the facing laser was only  $147 \pm 5$   $\mu$ A for an empty trap, and the intervention of a 3  $\mu$ m-diameter polymer sphere reduced it to  $95 \pm 10$   $\mu$ A, a reduction of only 35%. There is a clear relationship between the size of the obstacle and the resulting photocurrent, a correlation that could be used to characterise particles for trapping, analysis and sorting without the need of any external apparatus. This data was obtained with one diode permanently reverse-biased, but the insertion of a switch would allow the diode to be quickly switched between laser and photodetector modes so that particles could be trapped and then identified during a brief fraction of a second of reverse bias, before switching back to laser operation before the particle had been lost from the trap.

This second method, the photodetector, is the most useful for on chip analysis, removing the need for any external apparatus beyond that which is already required for the operation of the device; that is, the power supply, with perhaps the addition of an ammeter. The main point, though, is that the method requires no external optical components, and therefore allows the device to be small and compact, and removes the need for any optical alignment.

## 4.9 Demonstrations

In addition to detecting particles, a number of practical functions were demonstrated and certain qualitative demonstrations were conducted. As shown in Figure 4.12, asymmetric conglomerates (essentially a one-dimensional object)) rotated naturally by up to  $180^\circ$  in the horizontal plane in order to minimise their energy within the optical field. This presents the possibility of optically-actuated valves (*Terray et al. (2002)*), and movable optical components. Laser configurations were fabricated that should, with care, be able to generate sustained rotation for powering micro-gears, most notable for pumping. This was extended to three dimensional alignment when a planar crystal of adhered polymer spheres (essentially a

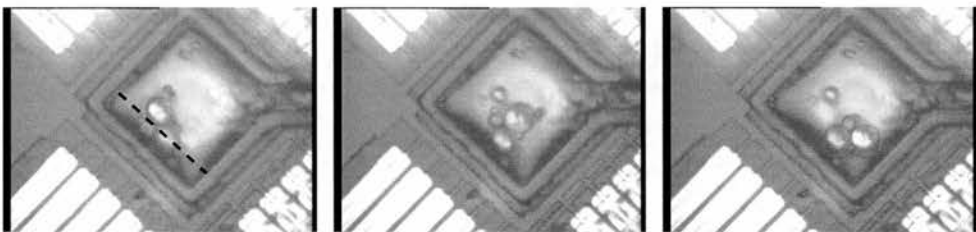


Figure 4.12: Alignment of asymmetric particles within a dual-beam trap. The spheres moved around in order to align themselves with the beams. The large spheres have diameters of 20  $\mu$ m. Incidentally, the grid system shown in these images could be used to generate an asymmetric force that would induce continuous rotation, not just alignment.

two-dimensional object) rotated from the horizontal plane into the vertical plane, as seen in Figure 4.13. This effect was a result of the high vertical beam divergence that caused the beams to effectively form a “sheet” of light in the vertical plane, within which a planar structure could minimise its free energy by aligning with the optical field. This ability to move objects in three dimensions, rather than just two, would allow the fabrication of a simple throttle valve, for example, by which the flow within a channel could be regulated. In a separate experiment individual spheres were collected into groups in traps, demonstrating the large catchment volume of the dual-beam trap.

The potential use of this system in biological applications was demonstrated by the trapping of mammalian cells, such as the SA2 cell shown in Figure 4.14. Due to the lower refractive index contrast and the subsequently weaker optical forces, cells responded more slowly than the spheres did to any given beam power, and were more easily washed out by a fluid flow. With care, though, the cells could be trapped, translated across the channel by varying the relative beam powers and even pushed into a side channel by a single beam.

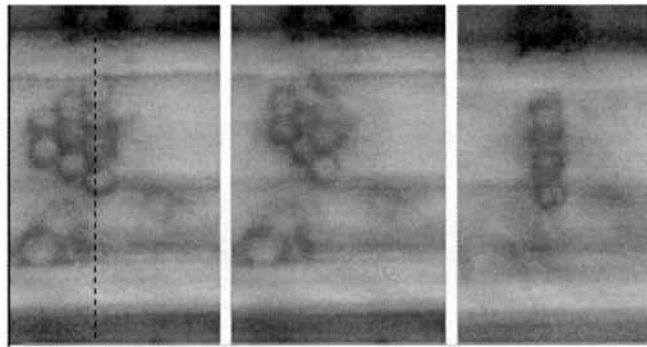


Figure 4.13: Vertical alignment of a planar crystal within a dual-beam trap. The conglomerate of  $5\ \mu\text{m}$ -diameter polymer spheres lies horizontally in the channel, until the forces exerted by the beams cause it to rotate to align itself in the vertical plane of the highly-divergent beams, thus minimising the crystal's energy within the vertically-divergent beams.



Figure 4.14: Image of an SA2 cell in a dual-beam trap. The low refractive index contrast between the cell and the medium makes both trapping and imaging difficult.

Primary amongst the demonstrations was a simple sorting device, a photograph of which is shown in Figure 4.15(a); its operation is illustrated in Figure 4.16. A  $5\ \mu\text{m}$ -diameter polymer sphere was first of all held against the fluid flow (left to right) by the trap at the left of the stills; its trapped status was proven by the motion across the channel that resulted from varying the relative beam powers. It was then released into the fluid flow by switching off the lasers, and then carried to the right by said flow, where it was held in the trap at the right. The direction of the fluid flow was reversed (right to left), and the sphere was released again. The middle (unpaired) laser was then switched on, the force of whose beam pushed the sphere into the side channel, where several other spheres had already been collected after similar journeys. This process took about a minute for each sphere; that was mainly because the laser powers were controlled manually, and the time could be significantly reduced (to a few seconds) by more reliable control of the lasers. However, once the human response time had been eliminated, the operational speed would still be limited by the time taken for the pushing laser to push a particle into the side channel. The fluid flow has to be slow enough to allow sufficient time for the pushing laser to get the particle into the side-channel before it passes by the junction. This constraint can be removed by stopping the fluid flow when the particle is at the junction, but that makes the operation very “stop-start”. It would also interfere with other processes elsewhere within the device, preventing parallel processing, which is one of the potential benefits of the miniaturised technology. A better design that is under construction at present replaces the T-junction with a Y-junction, as shown in Figure 4.15(b), so that the flow splits naturally into two equal halves. A particle in one half of the channel will flow into the associated output channel; switching between the two would be achieved by simply pushing a particle over the mid-point of the channel. This is much faster than pushing particles right across the channel, allowing a higher throughput.

The combination of this manipulation with fluorescence detection is the basis by which a micro-fluorescently activated cell sorter ( $\mu\text{FACS}$ ) device operates *Fu et al. (1999)*, sorting one fluorescent species from another. The use of two traps allows for second chances, or for the application of different tests at each trap. Any of the afore-mentioned detection schemes could play a useful role in such a sorting system. A realistic aim would be to optimise the system to the level of (*Fu et al. (1999)*); that is, 20 cells per second. Commercial cell sorters operate at much higher throughputs; for example, the B.D. Biosciences FACS Cell Sorting System can deal with 70,000 events per second, and uses 15 different fluorescence signals. Those machines are expensive and are used to sort out entire samples to give pure “lines” of different cells, but the device of *Fu et al. (1999)* and this integrated device could have applications in separating out small

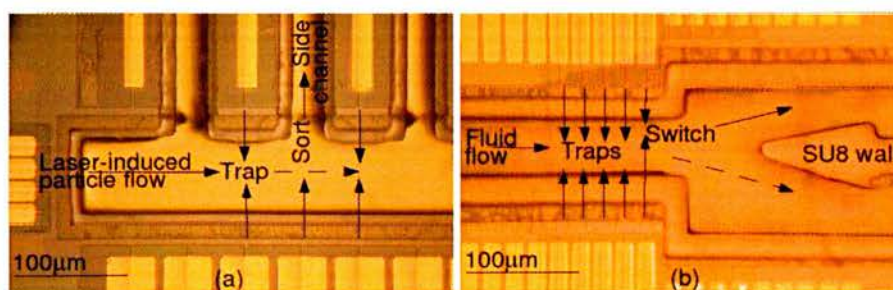


Figure 4.15: Configurations for simple sorting devices: (a) the T-junction as used in this project; (b) the Y-junction that would provide faster operation.

numbers of cells for analysis. It could also be useful for manipulating entire, small populations, such as in some gene therapy experiments in which only a small number of cells are treated. A major advantage of this technology would be its low cost and ease of use.

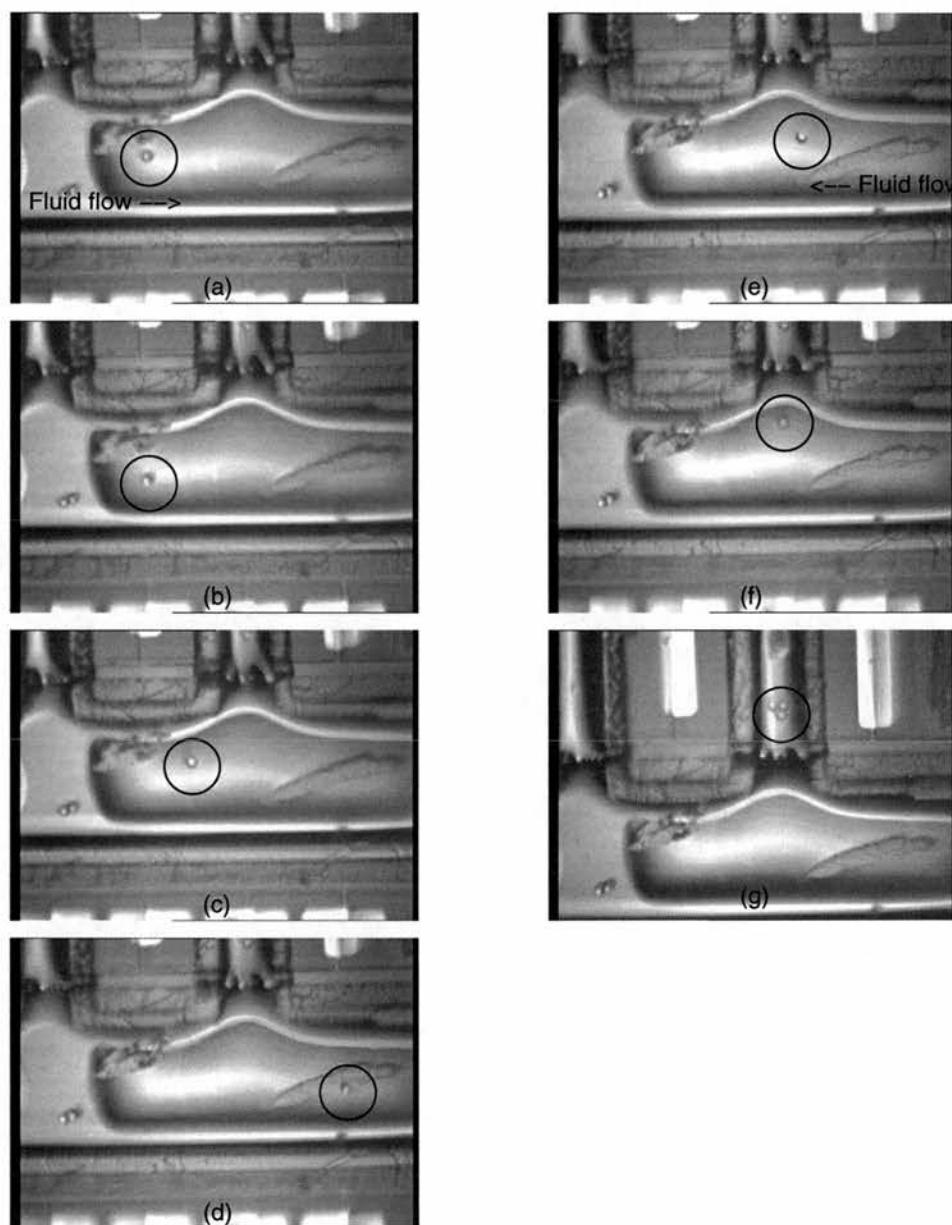


Figure 4.16: Sequence of stills showing the motion of a  $5\ \mu\text{m}$ -diameter polymer sphere (circled) in a simple sorting device. The particle is held in a dual-beam trap (a), moved within the trap (b), released into the flow (c), and then held in another dual-beam trap (d). It is then released into the (reversed) flow (e), pushed by a single beam (f) into the side channel, where other spheres have previously been collected (g) by the same process.

## Chapter 5

# Conclusions

This Thesis documents the original development of an entirely new technology for use in optical manipulation. As such, its conclusions can be divided into three categories: the practical development, the demonstrations, and the potential future impact. Firstly, there are the fabrication issues. The investigation of the laser manufacture resulted in fairly reliable devices, whilst the development of novel techniques allowed planar semiconductor processing techniques to be adapted for this quasi-three-dimensional application. The limitations of the current method have highlighted the need for further work to improve and diversify the performance. Secondly, there are the results. The physical data obtained from the devices illustrate that they reliably follow some basic predicted trends, offering the hope of successful studies of physical phenomena. The useful demonstrations of certain simple functions show that the technology is of practical use in microfluidic manipulation. Thirdly, there is the impact upon the world of optical manipulation. This technology overcomes many of the inherent limitations of all other optical manipulation systems, offering the real possibility of miniaturised, automated optical devices for use in studies of biology, colloidal science and atomic condensates.

### 5.1 Fabrication

The fabrication of semiconductor lasers made use of techniques that have been established and finely-tuned by the electronics industry, specifically the optoelectronics industry, but matching industrial standards is not possible at this stage; even the optimisation of the processes for the available combinations of materials and equipment took time and care. Beyond that, the integration of microfluidic channels had no prior work to use as a starting point. Imagination and lateral thinking were essential in the improvement of existing processes and in the development of new techniques. However, these efforts would have been wasted had the following basic principles not been followed.

The single most important aspect of any fabrication process is cleanliness, and the best approach is to prevent dirt and stains from touching the surface in the first place; removing them usually damages some

part of the device, and is often impossible. The next most important aspect is consistency, investigating the effect of the variables to identify those that had the biggest influence upon the results, and then ensuring that they are kept constant over each sample, and from one sample to the next, even over a period of months. To this end, it is important to monitor the performance of the materials and equipment in order that any variations should be noticed and compensated for. The third most important aspect of the fabrication is the need to think of the possible consequences of each step. This involves foresight, trying to avoid conflicts between the large number of processes, each involving numerous individual steps, that go into each device. More often, though, it has to work retrospectively, working out what has gone wrong, deciding whether it is due to random chance or a conflict that could occur again. In the latter case decisions have to be made about how to adjust either the processes or their order in the fabrication sequence.

The development of the novel laser fabrication process is a case in point. The original method yielded lasers whose performance was inconsistent and usually poor; the most likely source of the problem was identified as damage to the surface of the GaAs. Some logical thought, mixed with a bit of imagination, presented a few different options that could solve the problem. They were then investigated carefully, but in the end the solution was discovered not by design, but by lateral thinking. This solution was the “reflow and rub” method, which, although the very manual intervention is unorthodox, produced very reliable lasers.

Once the details of reliable laser fabrication had been resolved, the biggest challenge was the creation of the microfluidic channels. Rarely do other applications require that GaAs be etched to a depth of 15  $\mu\text{m}$ , and rarely must photolithography be conducted on such a distorted surface as results from so deep an etch. The utilisation of a lift-off-style mask for the deep etching, allowing the removal of the charred photoresist, was an example of lateral thinking. The lining of the channel with electrically-insulating SU8-2000 polymer was, at the outset, predicted to be the most challenging design feature, and did require an understanding of thin film processes, and the intellectual leap of applying them to very thick “thin films”. In amongst all of the other trials and breakthroughs, it remained perhaps the most quintessential feature of the device, forming the interface between the mutually-exclusive electricity and water.

The interplay between the fabrication of the laser ridges, the facets, and the deeply-etched channel was a case in which the consequences of processes involved in each step were of great significance. The simplest method had detrimental effects upon the performance of the lasers, and, although the successful method added extra time and effort into the fabrication of each device, it was worthwhile. Now that the point has been proven, some of the extra effort could be removed by designing specific photomasks for each type of device, which leads to another important conclusion that came from the fabrication, and that is the need for processes to be versatile. The optimum performance of each part of the devices - lasers, channels, imaging, detection, etc. - could not be accurately predicted in advance, so, rather than design photomasks with dozens of different iterations of the same features, very general masks were created that could be used in combination to create features with widely-ranging parameters, such as facet separation and laser length. On a similar note, it was important that each device or each set of test lasers was designed with a specific purpose in mind. Often there was a strong temptation to make each item as versatile as possible, but that often led to over-complication and uncertainty about which factors actually affected the results. Until the effect of each parameter is known, it is best to investigate each one separately, as far as is possible.

## 5.2 Results

The key factor in determining the physical effects of the devices upon colloidal particles was the ability to deduce how much power was entering the trapping channel. The relationship between that power and the power exiting through the outer, accessible facet was modelled theoretically, and empirical data agreed very well indeed, providing a reliable relationship. The measurement was simplified further by monitoring the currents that flowed into the lasers, and reading the correlated power from a pre prepared graph. This was only possible because the lasers behaved consistently over the several days of testing.

The devices were used to manipulate various sizes of polymer spheres in solution. Four quantitative studies were conducted, each of which agreed well with theoretical predictions of either specific values or general trends. The motion of spheres in a single beam allowed the transport of particles over short ranges, with higher beam powers giving larger ranges. The high beam divergence and associated reduction in intensity with distance from the laser limited the range to  $\sim 100 \mu\text{m}$  for typical beam powers. The equilibrium position of a dual beam trap was varied by altering the relative beam powers, and was found to agree very well with the predicted relationship. The recoil motion of a sphere from a displacement position to the equilibrium position was monitored, and yielded trends that were consistent with the case of a linear restoring force, which was modelled theoretically, allowing estimates of the spring constant, which increased with beam power. Finally, the Q factor of the trap in the direction of fluid flow perpendicular to the beams was measured for polymer spheres of a variety of sizes. As expected, the values increased with increasing particle size, and with reduced laser separation.

The first three studies that looked at motion along the axis of the laser beams took into account the reduction in intensity as the beams diverged. However, the effects of the actual divergence angles of rays as they hit the sphere were less obvious. The ray optics model of the axial forces exerted by a laser beam predicted that the divergence angle did have an effect upon the axial forces. The studies of the equilibrium position of a dual beam trap, and of the recoil back to that position, both assumed that the effects of the divergence angle upon the axial forces were constant along the z-axis. The agreement of the predictions and the results would seem to have justified this assumption.

Certain qualitative demonstrations were conducted. Spheres were used to demonstrate the basic function of a micro-fluorescence-activated cell sorter ( $\mu\text{FACS}$ ), utilising trapping with two beams and shunting with one beam. These functions were also demonstrated with biological cells, but their very low refractive index contrast resulted in much weaker forces and hence much slower speeds. Asymmetric particles were aligned in the horizontal plane and also vertically, and individual particles were grouped together in the traps. Various detection methods were demonstrated, including two that made use of the on-chip lasers to give truly integrated operations.

## 5.3 Impact

The impact of this new technology upon the world of optical manipulation could be huge. This technology negates many of the challenging problems that affect other optical manipulation systems. Where they

use discrete, macroscopic optical components to couple light from an external laser into a test chamber, this technology couples the light from diode lasers directly into the integrated microfluidic channel. This provides two major benefits. Firstly, it reduces the size of the apparatus from a bench-full to a thumb-nail, requiring only a low-voltage power supply, thus making the device convenient and portable. Secondly, the alignment is intrinsically perfect and robust, removing the need for time-consuming preparations and alterations, and even for any optical expertise whatsoever. Added to these primary benefits are several other advantages. The low voltages and simple electrical connections lend the technology to computer interfacing and automation. The direct coupling of light into the test chamber reduces the coupling losses. Although the beam paths cannot be altered once the laser positions have been defined, the small size of each laser gives plenty of space for multiple functions to be permitted on a single device, giving instantly-accessible versatility that, with macroscopic optics, would require reconfiguration of the system. A topical application of microfluidics is in the lab-on-a-chip world, and this technology would allow some of the power of optical manipulation to be brought to bear on medical testing, both in research and in point-of-care tests. The devices would be portable and automated, and so could be used in doctors' surgeries and in the field.

All of these advantages apply not just to microfluidic manipulation, but also to other potential applications that could benefit from this technology. The direct coupling into the channel may reduce the beam instability that is introduced by travel through larger distances, offering the possibility of highly accurate position sensing techniques for the study of molecular motion. The trapping and transport of Bose-Einstein condensates (BECs) could be conducted on such a chip. The necessary resolution of the channel could be provided by electron-beam lithography, and the operation in a vacuum would actually remove some complications, such as the need for lining the channel with electrical insulation. Both of these areas of work presently use complex optical set-ups, but transferring the functions to a simple chip would make them compact, robust and portable. Certain features would greatly improve the chances of success in each of the fields. The most significant advance would be the etching of cylindrical lenses to give horizontally-shaped beams, that would increase the intensities and hence the forces. The creation of vertical lenses would have a greater impact upon increasing the intensity, but would be more difficult. Once achieved, though, additional shaping or etching of the facets could be added to allow the generation of complex beam geometries, such as Bessel beams for guiding. And this work is not limited to the 980 nm and 1290 nm wavelengths used in this project. GaAs-based heterostructures can be fabricated to emit anywhere in the range 700 nm to 1300 nm, and other materials can go even further. For instance, GaN materials emit in the violet part of the spectrum, and could therefore be used to excite fluorescence in green fluorescent protein (GFP), which is a commonly-used biological dye, but this time on an integrated chip.

Key to all of these potential applications are the advantages of small size, intrinsic alignment and simplicity of operation that are offered by this new technology. It will allow experiments to be conducted automatically and in parallel, and by operators who possess no optical expertise. For these reasons the technology presented in this Thesis takes the power of optical manipulation and makes it available to a wider scientific audience. Perhaps, indeed hopefully, it will find a useful role in systems that aid us in our research and that work for the benefit of humanity.

## Chapter 6

# Appendix

### 6.1 Ray Optics Regime

The ray optics approach is appropriate for modelling the Mie regime in which the wavelength of the light (1290 nm in this case) is much smaller than the size of the particles. The particles used in this work had diameters of 2-20  $\mu\text{m}$ , the smallest of which are comparable to the 1290 nm wavelength and so, strictly speaking, are in the Rayleigh regime, and should be modelled using electromagnetic fields. However, the ray optics model is applicable for most of the particles and is instructive for this discussion.

The following discussion outlines a mathematical model that was created and solved numerically in order to estimate the axial forces that act upon spherical particles in a laser beam. It was motivated partly by curiosity about such a model, and partly by a desire to compare the experimental results of Chapter 4 with some simple theoretical predictions. The data was generated numerically, using a spreadsheet on Open Office; the files were generally 200 - 400 kB in size. Only the axial forces were considered, and they were modelled by considering the effects of a beam of uniform intensity, the validity of which is discussed in Section 6.8. The model was developed without reference to, but is comparable to, that of *Liebert and Prieve (1995)*. It is more complicated to consider the radial forces, which require the analysis of a non-uniform optical intensity over the surface of a sphere; such a model is presented in *Sidick et al. (1997)*, but not in this Thesis.

### 6.2 Direction of Photon Propagation

The optical forces are primarily the result of the changes in direction of photon propagation that occur at the boundaries of optical media. This has already been introduced in Chapter 1. The cross-section in Figure 6.1 illustrates more fully the situation that arises when a ray impinges upon a sphere of radius  $r_s$  and refractive index  $n_s$  in a fluid of refractive index  $n_f$ . The  $z$ -axis represents the axis of the laser beam and  $\theta_d$ , the divergence angle, is the angle at which a ray travels within said beam. The angles of propagation

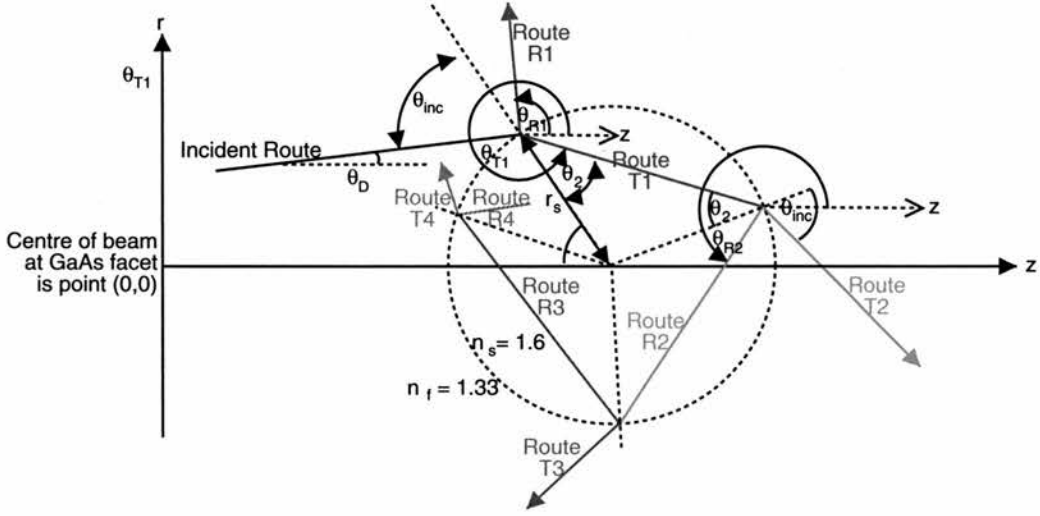


Figure 6.1: Paths of rays as they travel through a sphere. The definitions are discussed in the main text.

are all measured anti-clockwise from the positive  $z$ -axis; but the angle  $\theta_r$  is measured from the negative  $z$ -axis to the point at which the incident ray touches the first interface. In addition the angles of incidence ( $\theta_{inc}$ ), reflection and refraction ( $\theta_2$ ) are measured with respect to the normal to the boundary. The circular symmetry of the situation means that the angles  $\theta_{inc}$  and  $\theta_2$  recur; they are given by

$$\theta_{inc} = \theta_r + \theta_d \quad (6.1)$$

$$\theta_2 = \arcsin \left( \sin \theta_{inc} \frac{n_f}{n_s} \right) \quad (6.2)$$

Unless otherwise stated, the refractive indices take the same values as in Chapter 1; that is,  $n_f = 1.33$  and  $n_s = n_p = 1.6$ . The definition of the angle  $\theta_r$  stems from the numerical integration method that is used to evaluate the forces. The sphere is divided into  $N_r$  rings, each of angular width  $\Delta\theta$ , such that  $N_r \Delta\theta = 90^\circ$ .  $\theta_r$  is taken to be the midpoint of a ring, so that

$$\theta_r = \left( N_r - \frac{1}{2} \right) \Delta\theta_r \quad (6.3)$$

The situation is broken down into events at successive interfaces. The incident ray interacts with the first interface, resulting in the first reflected ray, R1, and the first transmitted ray, T1. T1 strikes the second interface, at which point some is transmitted, T2, back out of the sphere, and the rest, R2, remains within the sphere. The same process is repeated at each boundary, leading to the names of the other propagation routes that are shown in Figure 6.1. Geometry can be invoked to show that the angles of propagation are as follows:

$$\theta_{T1} = 360 - \theta_r + \theta_2 \quad (6.4)$$

$$\theta_{R1} = 180 - 2\theta_r - \theta_d \quad (6.5)$$

$$\theta_{T2} = 360 - 2\theta_r + 2\theta_2 - \theta_d \quad (6.6)$$

$$\theta_{R2} = 180 + 3\theta_2 - \theta_r \quad (6.7)$$

$$\theta_{T3} = \theta_{R2} + \theta_2 - \theta_{inc} \quad (6.8)$$

$$\theta_{R3} = \theta_{R2} - 180 + 2\theta_2 \quad (6.9)$$

$$\theta_{T4} = \theta_{R3} + 180 - 2\theta_2 \quad (6.10)$$

$$\theta_{R4} = \theta_{R3} + \theta_2 - \theta_{inc} \quad (6.11)$$

Justification for considering only these four interfaces is given in Section 6.7. For now it should be noted that only some of these rays need be considered. For example, if only the first and second interfaces are used, then only rays R1, R2 and T2 are relevant; or if four interfaces are considered then the rays R1, T2, T3, R4 and T4 are relevant.

### 6.3 Photon Momentum

Using the above convention of measuring all propagation angles anticlockwise from the positive  $z$  axis, the axial and radial components of a photon's momentum are given by

$$p_z = p_0 \cos \theta \quad (6.12)$$

and

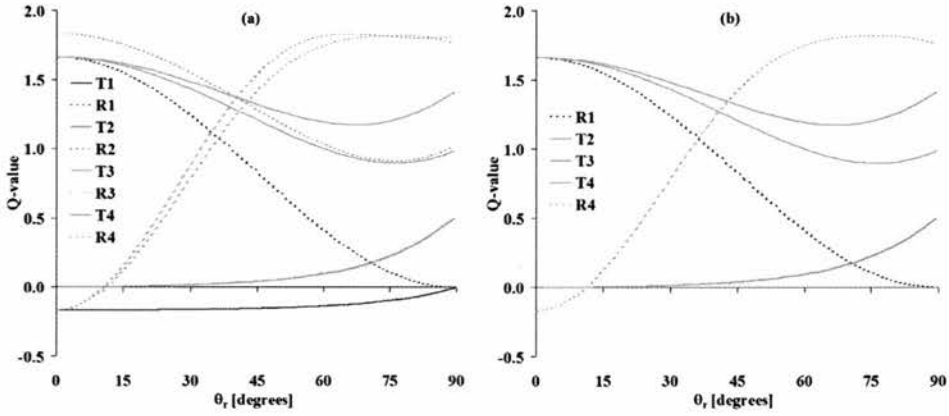


Figure 6.2: Axial Q-values for various routes within a sphere. At specific angles  $\theta_r$ , with no reference to ring width: (a) all 8 routes illustrated in Figure 6.1; (b) those 5 routes that are relevant to force calculations.

$$p_r = p_0 \sin \theta \tag{6.13}$$

respectively, where  $\theta$  can take any of the values corresponding to ray R1, T2, etc, and  $p_0$  depends upon the refractive index, according to Equation (1.1). Changes in the radial components contribute to the transverse trapping, but are not considered in this Thesis. The change in the axial momentum with respect to the incident photons in simply

$$\Delta p_z = p_z - p_{z_0} \tag{6.14}$$

where  $p_{z_0}$  is the magnitude of the momentum of a photon in water before entering the sphere. By assigning a value to  $\theta_{inc}$  the changes that occur on each route can be calculated. Setting  $\theta_d = 0$  and  $\Delta\theta = 1^\circ$  (so that  $\theta_r$  is 0.5, 1.5, ..., 89.5°) the data plotted in Figure 6.2 can be calculated. For each route it shows the ratio of the axial momentum component to that of the incident ray, which is zero in this case of  $\theta_d = 0^\circ$ . This is the axial Q-value for a photon on that route. The photons on the routes that remain inside the sphere (T1, R2, R3 and R4) have larger total momenta (due to the higher refractive index in the sphere) than do the incident photons, and so can have  $Q > 2$ .

### 6.4 Power Striking a Three-dimensional Ring

The interactions that occur within a sphere are simply a three-dimensional extension of the circular case. Figure 6.3(a) illustrates how the circular cross-section of Figure 6.1 can be rotated around the  $z$ -axis, through an angle  $\phi = 0$  to  $360^\circ$ , so that a ray at angle  $\theta_{inc}$  is translated around a circle. The angular width of the ring is called  $\Delta\theta$ , and it can be shown that a ring's area on the surface of the sphere is

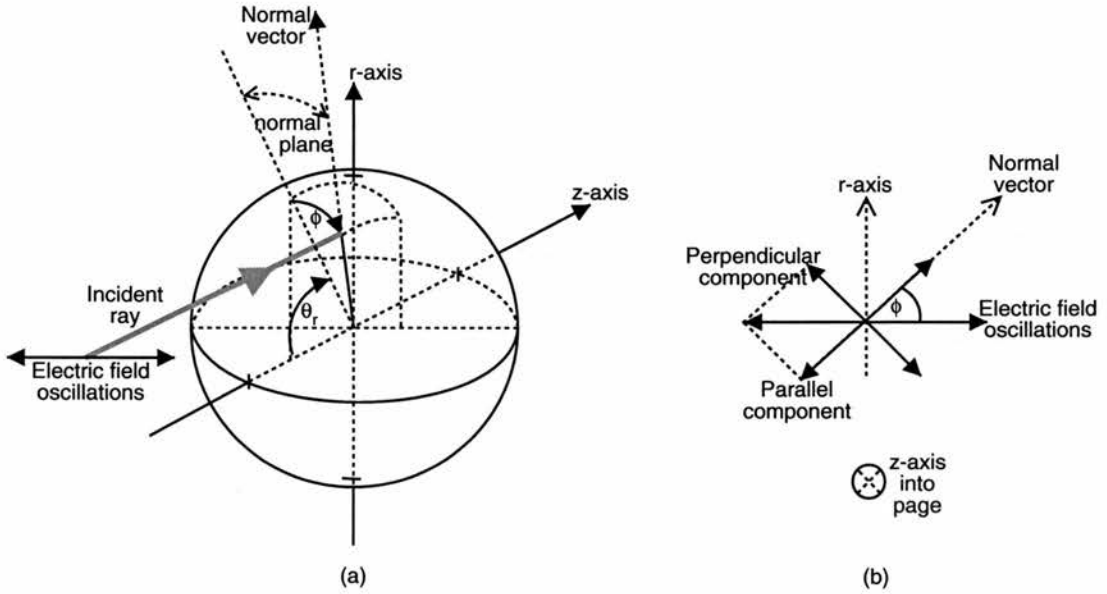


Figure 6.3: Definitions of angles  $\theta_r$  and  $\phi$ : (a) Definition of normal plane at sphere's surface; (b) components of electric field at sphere's surface.

$A_{\text{ring}} = 2\pi r_s^2 \sin \theta_r \Delta\theta$ . The power in the laser beam,  $P$ , and its cross-sectional area,  $A_b$ , give its intensity,  $I = P/A_b$ . A circular beam has a cross-sectional area  $A_b = \pi r_b^2$  where  $r_b$  is its radius. The intensity on the surface of the sphere,  $I_s$ , is lower than this, and is given by  $I_s = I \cos \theta_r$ . So, the total power striking a ring is

$$P_{\text{ring}} = P \left( \frac{r_s^2}{r_b^2} \right) \pi \Delta\theta \sin 2\theta_r \quad (6.15)$$

from which the number of photons in the ring is found by simply dividing by the photon energy,  $E = hc/\lambda$ . If the beam and the sphere have the same radius then the power in any ring is independent of the sphere size.

## 6.5 Number of Photons on Each Route

The photons in any individual ring follow the same routes, as defined in Figure 6.1. However, the number of photons on each route depends upon the reflectivity, which is divided into two components,  $R_{\parallel}$  and  $R_{\perp}$ , given by

$$R_{\parallel} = \left( \frac{\tan(\theta_{\text{inc}} - \theta_2)}{\tan(\theta_{\text{inc}} + \theta_2)} \right)^2 \quad (6.16)$$

and

$$R_{\perp} = \left( \frac{\sin(\theta_{\text{inc}} - \theta_2)}{\sin(\theta_{\text{inc}} + \theta_2)} \right)^2 \quad (6.17)$$

The amount of light that experiences each component depends upon the angle  $\phi$ , which is the angle of the electric field to the normal vector of the sphere's surface, as shown in Figure 6.3(b). In this case, the electric field from the semiconductor lasers is polarised in the horizontal plane (in a ratio of more than 100:1), so the relative sizes of the components vary regularly around the circle. The intensity is proportional to the square of the electric field, so the parallel and perpendicular intensities are, respectively,

$$I_{\parallel} = I_0 \sin^2 \phi \quad (6.18)$$

and

$$I_{\perp} = I_0 \cos^2 \phi \quad (6.19)$$

The total reflectivity at the angle  $\phi$  is then

$$dR = I_0 \sin^2 \phi R_{\parallel} + I_0 \cos^2 \phi R_{\perp} \quad (6.20)$$

which can be integrated around the circle to give the net reflectivity of the ring:

$$R(\theta) = \frac{1}{2} (R_{\parallel} + R_{\perp}) \quad (6.21)$$

The remaining fraction,  $1 - R(\theta)$ , is transmitted through the boundary. These fractions depend only upon  $\theta_{\text{inc}}$  and  $\theta_2$ , and so are the same at each boundary that is encountered by the light that enters through a ring at  $\theta_r$ .

So, having determined the number of photons that strike a ring and the fractions that are reflected and transmitted, the total number,  $N_x$ , that follow a particular route, where  $x$  denotes R1, T1, etc, is simply

$$N_{R1} = N_{\text{ring}} R(\theta_r) \quad (6.22)$$

$$N_{T1} = N_{\text{ring}} (1 - R(\theta_r)) \quad (6.23)$$

$$N_{R2} = N_{\text{ring}} (1 - R(\theta_r)) R(\theta_r) \quad (6.24)$$

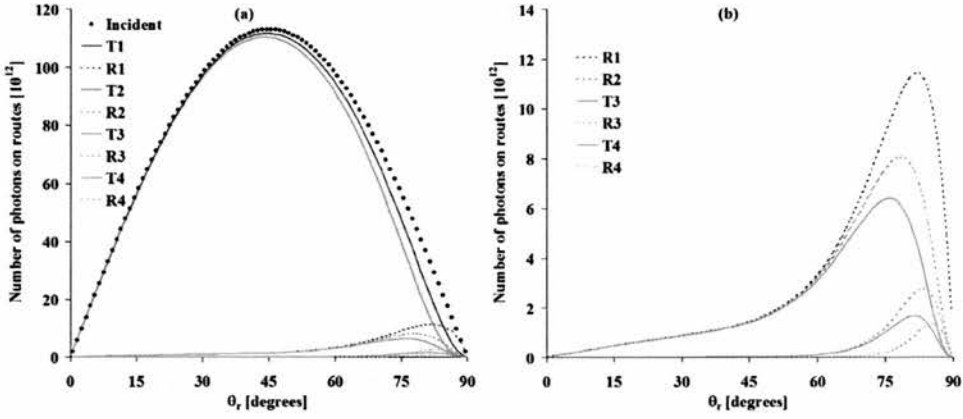


Figure 6.4: Numbers of photons on different routes with ring width  $\Delta\theta = 1^\circ$ : (a) all 8 routes; (b) close-up of less populated routes.

and so on. This data is plotted in Figure 6.4 for a total beam power of 1 mW, and refractive indices  $n_f = 1.33$  and  $n_s = 1.60$ , where the angle  $\theta_r$  is again varied in  $1^\circ$  increments, and the width of each ring is  $\Delta\theta = 1^\circ$  (giving 90 rings). Therefore, the value of  $N_x$  at any angle is the number of photons in a ring of width  $\Delta\theta = 1^\circ$ , rather than the number in an infinitesimally thin ring. The sphere's cross-sectional area equals that of the beam, so they do not affect the results.

### 6.6 Forces Due to Routes

The total axial force exerted by photons on the different routes is then found by multiplying the change in axial momentum per photon, by the number of photons on that route. The data is plotted in Figure 6.5. Again, it is important to note that the force at any angle is that due to a ring of width  $1^\circ$ .

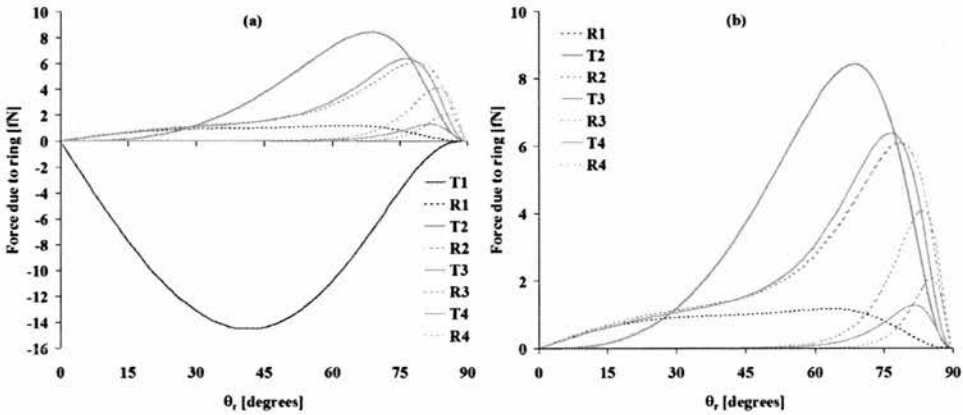


Figure 6.5: Forces due to different routes with ring width  $\Delta\theta = 1^\circ$ : (a) all 8 routes; (b) close-up of 7 routes.

Now obviously not all of these eight routes can be used together. If, for example, all four interfaces are used then routes T1, R2 and R3 should be ignored. Taking this into account, the total axial force,  $F_z$ , exerted by 1 mW of power spread uniformly over the cross-sectional area of the sphere is  $5.96 \times 10^{-13}$  N. Because the power in each ring is independent of the sphere's size it follows that this result holds true for any size of sphere over which 1 mW of power is spread; spread over the cross-sectional area, not the surface area. This allows the definition of a coefficient,  $B_z$ , that translates the power in Watts (over a spherical surface of any size) into an axial force in Newtons. This model gives a value of  $5.96 \times 10^{-10}$  N/W for the given refractive indices, which agrees very well with the value of  $6 \times 10^{-10}$  N/W in *Liebert and Prieve (1995)*. This coefficient is used in Chapter 4 to estimate the spring constant of a dual-beam trap, giving very good agreement with experimental data. Another way of expressing the efficiency of the optical interactions is the Q-factor. As discussed in the Introduction, the Q-factor of a beam is defined in the same manner as for an individual photon: it is the ratio of the resultant force in a certain direction to the total incident momentum. This model gives the value for the axial Q-factor of a sphere as 0.135, out of a maximum value of 2. It is trivial to show that the Q-factor along the  $z$ -axis is related to the co-efficient  $B_z$  according to

$$Q_z = \frac{B_z c}{n_f} \quad (6.25)$$

Another comparison with *Liebert and Prieve (1995)* can be made by setting the sphere's refractive index to some large value, such as 100,000, so that  $R = 1$ , and calculating the axial force thus generated. Both this model and their paper give answers of  $9 \times 10^{-9}$  N/W for this situation, which is the largest force that could be generated by the beam.

In addition, Figure 6.6 allows comparison with the case of reflection from a planar surface in Chapter 1. This is done by increasing the sphere's radius,  $r_s$ , whilst keeping the beam's radius,  $r_b$ , and its power,  $P$ , at values of unity and 1 mW, respectively. As  $r_s$  increases, the rings at larger values of  $\theta_r$  are no longer

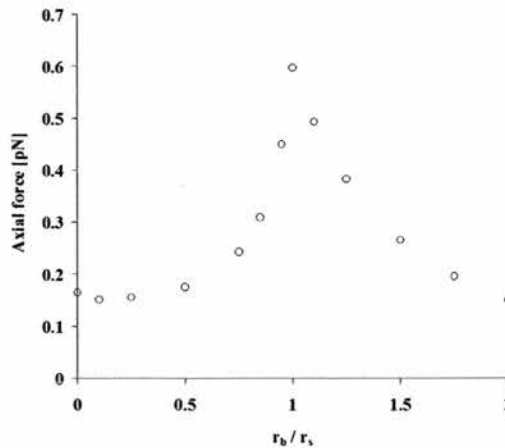


Figure 6.6: Variation of axial force with sphere radius. As the sphere radius is increased to infinity, the value of the axial force tends towards that which was obtained using the simple planar model.

struck by the beam; Figure 6.5 shows that these rings contribute much to the axial force so their absence decreases the force. Again using 90 rings, the data in Figure 6.6 was calculated. In this graph, the zero of the  $x$  axis represents that case of an infinitely-large sphere; that is, a planar surface, such as that in Chapter 1, for which the force was calculated to be  $1.64 \times 10^{-13}$  N. This agrees with the model's calculation to within 8%, which lends credence to said model. The axial force increases as the sphere's radius decreases, reaching a maximum when it exactly matches the size of the beam, allowing the high-angle rings to access the power. When the sphere's radius is smaller than that of the beam, the force falls again, because some of the power passes by the sphere, and the intensity over the sphere is lower. On the other hand, if the intensity of a beam that completely covers that sphere was to be increased, then the force would also increase.

## 6.7 Accuracy of Model

The decision to use four interfaces can be justified by considering the data in Figure 6.7. Figure 6.7(a) shows the force due to each of 90 rings, using 1, 2, 3 and 4 interfaces. Clearly using only the first interface gives a spurious result, and that is because the majority of the photons are transmitted into the sphere where the magnitude of their momentum increases, translating into a negative axial force on the sphere. In reality, those photons will exit the sphere at some later interface; indeed the data converges as extra interfaces are added into the model. In addition, Figure 6.7(b) shows the total force induced by 1 mW of power over a sphere, as calculated for different ring widths,  $\Delta\theta$ , (corresponding to different numbers of rings) and for different numbers of interfaces. Reducing the ring width does change the force estimate, but not by much, so using 90 rings is perhaps excessive, but higher resolution is preferable to low resolution. The number of interfaces is again shown to be more significant, with the results seeming to tend towards a value as the number of interfaces is increased. The amount of light that remains inside the sphere after the fourth interface is 0.19% that of the incident power; if all of it exited back along the  $z$ -axis (that is,  $Q = 2$ ), then the additional exerted force would be 0.0186 pN, which is 3% of the estimated force. In reality, not all of

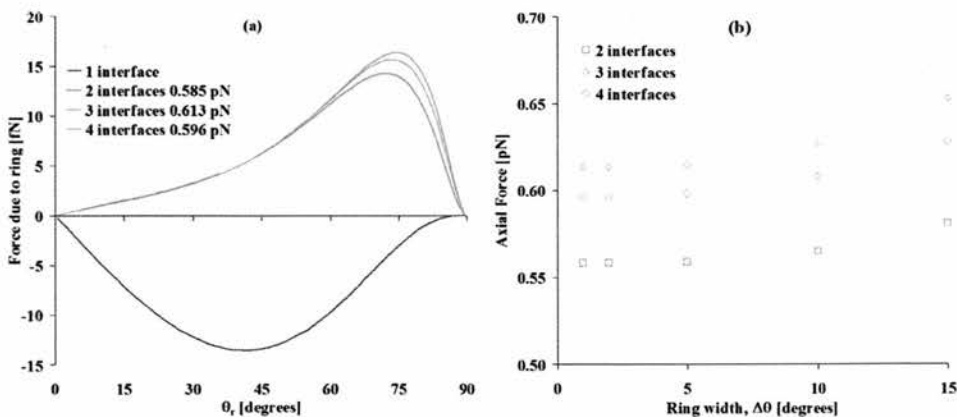


Figure 6.7: Improvements to accuracy of model: (a) increasing the number of interfaces (with ring width  $1^\circ$ ) causes the forces to tend towards a final value; (b) the accuracy of the model does not depend strongly upon the ring width,  $\Delta\theta$ .

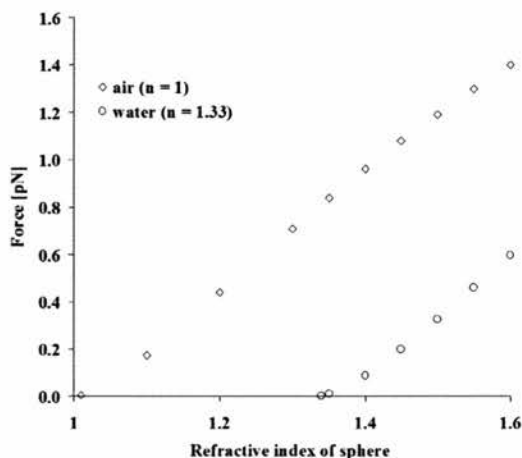


Figure 6.8: Axial force for different refractive indices. Clearly, the axial force is much weaker when the refractive index contrast is reduced, as is the case with biological cells in water.

the light would do that, so any additional force would be smaller than that maximum possible value, and the four-interface estimate is taken to be reliable.

The data plotted thus far has been for a sphere of refractive index 1.60, in water of refractive index 1.33. This was the case in the experiments of Chapter 4, but different refractive indices can be inserted into the model. Figure 6.8 shows how the forces predicted by the model are affected by the refractive index of the sphere, both in water and in air ( $n = 1$ ). This is of interest primarily in relation to biological cells, whose refractive indices are typically 1.35 to 1.45; the forces are therefore predicted to be less than a third of those for a polymer sphere. This illustrates the need for more optical power when manipulating cells, an issue that must be addressed if this technology is to be truly useful.

## 6.8 Mode Area and Force in a Device

Having obtained these predictions, it is necessary to consider how they might be applied to the experimental data of Chapter 4. The axial force exerted by a single beam is difficult to measure, because the drag force masks its effect, and the two could only be disentangled by carefully analysing the motion in order to solve Equation (4.2). The resolution of the data was insufficient to permit such a process. However, this model does provide information that is pertinent to the other two axial effects that were studied; namely the variation with beam power of the equilibrium position of a dual-beam trap, and the restoration of a particle to said equilibrium position after an enforced displacement. In both cases it was necessary to find a simplified description of the beam that was emitted into the trapping channel of a real device.

There were three main considerations. The first was the effect of the divergence upon the angle of incidence at the sphere, and hence upon all of the other angles, and the resultant force. However, the effect is only significant for large divergence angles, and the angles near to the  $z$  axis are small, especially at larger distances from the facets. This neatly negates the complications of the two different divergence

directions in the device's lasers. So, the small spheres for which data was collected were essentially sitting in a non divergent beam (although the beam does expand, reducing the intensity). Secondly, upon exiting through the GaAs facet, the beam expanded, and it was necessary to obtain an expression for the mode area,  $A_m$ , and hence the intensity, at each point along the  $z$  axis. The half angles of divergence, horizontally and vertically, were measured to be  $\theta_x = 1.2^\circ$  and  $\theta_y = 20^\circ$ , respectively, to the half maximum point in the intensity. The beam expands from an initial area  $A_m(0) = \pi\omega_{0x}\omega_{0y}$  on the facet, where  $\omega_{0x}$  and  $\omega_{0y}$  are the beam waists in the horizontal and vertical directions respectively; typical values are  $\omega_{0x} = 2 \mu\text{m}$  and  $\omega_{0y} = 0.4 \mu\text{m}$ . The mode area at a distance,  $z$ , from the facet is therefore

$$A_m = \pi (\omega_{0x} + z \tan \theta_x) (\omega_{0y} + z \tan \theta_y) \quad (6.26)$$

This is not particularly wieldy, and is more useful if approximated to a square law of

$$A_m \approx A_0 (z + z_0)^2 \quad (6.27)$$

where  $A_0 = \pi \tan \theta_x \tan \theta_y$  and where  $z_0$  is a constant distance from the facet, either in front or behind. The value of  $z_0$  can be deduced by setting  $z = 0$  in Equation (6.27) using  $A_m(0)$ , as defined above, so that

$$z_0 = \sqrt{\frac{A_m(0)}{A_0}} \quad (6.28)$$

Having thus determined  $z_0$ , Equation (6.27) can be used to determine the mode area,  $A_m$ , at any distance,  $z$  from the facet. Assuming uniform intensity across the beam, the beam intensity at any point is simply the total power in the beam divided by this area. The third and final consideration was the effect of the SU8-2000 lining in the channel. Refraction at the polymer water interface would increase the divergence angles, thus changing the other angles and the beam's intensity, but the change would be small, only a few degrees, so the polymer lining is ignored.

It is then possible to create an expression for the axial force at any point along the  $z$ -axis. Assuming that the beam's power is uniformly spread across its area, then the power that is intercepted by the sphere is

$$P_s = P \frac{A_s}{A_m} \quad (6.29)$$

Using the conversion constant,  $B_z$ , this power is translated into a force of

$$F_z(z) = B_z P \frac{A_s}{A_m} = \frac{Q_z n P}{c} \frac{A_s}{A_m} \quad (6.30)$$

These simplifications allow the model to be applied to the data in Chapter 4 in order to generate some useful comparisons. The model itself could, with time, be expanded to cover more effects.

# List of Abbreviations

AFM: Atomic Force Microscope  
BEC: Bose-Einstein condensate  
CAIBE: Chemically-Assisted Ion Beam Etching  
CCD: Charge-Coupled Device  
CVD: Chemical Vapour Deposition  
CW: Continuous Wave  
EC solvent: Developer for SU8-2000 polymer  
FACS: Fluorescence Activated Cell Sorter  
GFP: Green Fluorescent Protein  
HSC: Heat Sink Compound  
IBS: Ion Beam Source  
ID: Inner Diameter  
IPA: IsoPropyl Alcohol  
LOR-7B: Lift-off Resist (7B blend)  
MBE: Molecular Beam Epitaxy  
MEMS: Micro-Electro-Mechanical Systems  
MF319: Developer for SR1800 polymer  
MMQW: Modified Multiple Quantum Wells  
MQW: Multiple Quantum Wells  
OD: Outer Diameter  
PMMA: polymethylmethacrylate (an e-beam-sensitive polymer)  
ppt: parts per thousand  
RIE: Reactive Ion Etching  
SA2: St Andrews 2 cell line (mouse leukaemic)  
sccm: standard cubic centimetres per minute  
SEM: Scanning Electron Microscope  
SLM: Spatial Light Modulator  
SQW: Single Quantum Well  
SR1800: Shipley Resist 1800 Series (1805 and 1818 blends) - a positive photoresist  
SU8-2000: a negative photoresist  
SVC-14: Positive resist stripper

# List of Publications

## Peer-Reviewed Publications

S. J. Cran-McGreehin, T. F. Krauss and K. Dholakia, "Integrated microfluidic optical manipulation", *Lab-on-a-Chip*, doi:10.1039/b605237a, 2006

S. J. Cran-McGreehin, K. Dholakia and T. F. Krauss, "Monolithic integration of microfluidic channels and semiconductor lasers", *Optics Express*, Volume 14, p7723, 2006

## Non Peer-Reviewed Publications

S. J. Cran McGreehin, K. Dholakia and T. F. Krauss, "Lasers meet fluids: an integrated approach", *Optics and Lasers Europe*, Issue 143, p23, 2006

S. J. Cran McGreehin, T. F. Krauss and K. Dholakia, "Integrated microfluidic optical manipulation", *Proceedings of  $\mu$ TAS 2005*, Volume 2, p1358, 2005

S. J. McGreehin, L. O Faolin, J. Roberts, T. F. Krauss and K. Dholakia, "Optoelectronic integrated tweezers", *SPIE Proceedings*, Volume 5514, 2004

## Patent

"Opto Electronic Tweezers", The University Court of The University of St Andrews (applicant), K. Dholakia, T. F. Krauss and S. J. Cran-McGreehin (inventors). At PCT application stage (PCT/GB/2005/001769 filed, 10th May 2005), stemming from British Patent GB 0410579.7, filed 12th May 2004, currently published as International Publication WO 2005/112042 A1.

# Bibliography

- J. Andrus. Fabrication of semiconductor devices. *U. S. Patent 3,122,817*, 1957.
- A. Ashkin. Acceleration and trapping of particles by radiation pressure. *Phys. Rev. Lett.*, 24:156, 1970.
- A. Ashkin. Optical levitation by radiation pressure. *Appl. Phys. Lett.*, 19:283, 1971.
- A. Ashkin. Optical levitation in high vacuum. *Appl. Phys. Lett.*, 28:333, 1976.
- A. Ashkin. History of optical trapping and manipulation of small-neutral particle, atoms, and molecules. *IEEE*, 6(6):841, 2000.
- A. Ashkin and J. M Dziedzic. Optical trapping and manipulation of viruses and bacteria. *Science*, 235:1517, 1987.
- A. Ashkin and J. M Dziedzic. Internal cell manipulation using infrared laser traps. *Proc. Natl. Acad. Sci. USA*, 86:7914, 1989.
- A. Ashkin, J. M Dziedzic, J. E. Bjorkholm, and S. Chu. Observations of a single beam gradient force optical trap for dielectric particles. *Opt. Lett.*, 11:288, 1986.
- A. Ashkin, J. M Dziedzic, and T. Yamane. Optical trapping and manipulation of single cells using infrared laser beams. *Nature*, 330:769, 1987.
- A. Ashkin, K. Schütze, J. M. Dziedzic, U. Eutenauer, and M. Schliwa. Force generation of organelle transport measured *in vivo* by an infrared laser trap. *Nature*, 348:346, 1990.
- R. Bar-Ziv, T. Frisch, and E. Moses. Entropic expulsion in vesicles. *Phys. Rev. Lett.*, 75:3481, 1995a.
- R. Bar-Ziv, R. Menes, E. Moses, and S. A. Safran. Local unbinding of pinched membranes. *Phys. Rev. Lett.*, 75:3356, 1995b.
- J. E. Bjorkholm, R. R. Freeman, A. Ashkin, and D. B. Pearson. Observation of focusing of neutral atoms by the dipole forces of resonance radiation pressure. *Phys. Rev. Lett.*, 41:1361, 1978.
- S. M. Block, D. F. Blair, and H. C. Berg. Compliance of bacterial flagella measured with optical tweezers. *Nature*, 338:514, 1989.
- S. M. Block, L. S. B. Goldstein, and B. J. Schnapp. Bead movement by single kinesin molecules studied with optical tweezers. *Nature*, 348:348, 1990.
- P. J. H. Bronkhorst, G. J. Streekstra, J. Grimbergen, E. J. Nijhof, J. J. Sixma, and G. J. Brakenhoff. *Biophys. J.*, 69:1666, 1995.
- J. K. Burkhardt, J. M. McIlvain Jr., M. P. Sheetz, and Y. Argon. *J. Cell Sciences*, 104:151, 1993.
- A. Y. Cho. Film deposition by molecular beam epitaxy. *J. Vac. Sci. Technol.*, 8:31, 1971.
- A. Choudhury, B. J. Ackerson, and N. A. Clark. Laser-induced freezing. *Phys. Rev. Lett.*, 55:833, 1985.
- S. Chu, J. E. Bjorkholm, A. Cable, and A. Ashkin. Experimental observation of optically trapped atoms. *Phys. Rev. Lett.*, 57:314, 1986.

- A. Constable, J. Kim, J. Mervis, F. Zarinetchi, and M. Prentiss. Demonstration of a fiber-optical light-force trap. *Opt. Lett.*, 18(21):1867, 1993.
- J. C. Crocker and D. G. Grier. When like charges attract: the effects of geometrical confinement on long-range colloidal interactions. *Phys. Rev. Lett.*, 77:1897, 1996.
- J. C. Crocker, J. A. Mattes, A. D. Dinsmore, and A. G. Yodh. Entropic attraction and repulsion in binary colloids probed with a line optical tweezer. *Phys. Rev. Lett.*, 82:4352, 1999.
- J. Dai and M. P. Sheetz. *Biophys. J.*, 68:988, 1995.
- R. Dingle, W. Wiegmann, and C. H. Henry. Quantum states of confined carriers in very thin  $\text{Al}_x\text{Ga}_{1-x}\text{As}$ - $\text{GaAs-Al}_x\text{Ga}_{1-x}\text{As}$  heterostructures. *Phys. Rev. Lett.*, 33:827, 1974.
- J. Durnin. Exact solutions for nondiffracting beams. I. The scalar theory. *J. Opt. Soc. Am. A*, 4(4):651, 1987.
- J. Durnin, Jr. J. J. Miceli, and J. H. Eberly. Diffraction-free beams. *Phys. Rev. Lett.*, 58(15):1499, 1987.
- L. Feenstra, L. Anderson, and J. Schmiedmayer. Microtraps and atom chips: Toolboxes for cold atom physics. *Gen. Relativ. Gravitation*, 36:2317, 2004.
- H. Feigner, R. Frank, and M. Schliwa. *J. Cell Sci.*, 109:509, 1996.
- A. Fu, C. Spence, A. Scherer, F. Arnold, and S. Quake. A microfabricated fluorescence-activated cell sorter. *Nature Biotech.*, 17:1109, 1999.
- L. P. Ghislain and W. W. Webb. Scanning force microscope using an optical trap. *Opt. Lett.*, 18:1678, 1993.
- J. P. Gordon and A. Ashkin. Motion of atoms in radiation trap. *Phys. Rev. A*, 21:606, 1980.
- F. S. Goucher, G. L. Pearson, M. Sparks, G. K. Teal, and W. Shockley. Theory and experiment for a germanium p-n junction. *Phys. Rev.*, 81:637, 1950.
- J. Guck, R. Ananthkrishnan, H. Mahmood, T. J. Moon, C. C. Cunningham, and J. Käs. The optical stretcher: A novel laser tool to micromanipulate cells. *Biophys. J.*, 81:767, 2001.
- T. Gustavson, A. P. Chikkatur, A. E. Leanhardt, A. Grlitz, S. Gupta, D. E. Pritchard, and W. Ketterle. Transport of bose-einstein condensates with optical tweezers. *Phys. Rev. Lett.*, 88, 2002. 020401.
- I. Hayashi, M. B. Panish, P. W. Foy, and S. Sumski. *Appl. Phys. Lett.*, 17:109, 1970.
- E. Higurashi, H. Ukita, H. Tanaka, and O. Ohguchi. Optically induced rotation of anisotropic micro-objects fabricated by surface micromachining. *Appl. Phys. Lett.*, 64:2209, 1994.
- R. Huber, S. Burggraf, T. Mayer, S. M. Barns, P. Rosnagel, and K. O. Stetter. Isolation of a hyperthermophilic archaeum predicted by *in situ* RNA analysis. *Nature*, 376:57, 1995.
- F. V. Ignatovich and L. Novotny. Real time and background free detection of nanoscale particles. *Phys. Rev. Lett.*, 96(013901), 2006.
- C. Jensen McMullin, H. P. Lee, and E. R. Lyons. Demonstration of trapping, motion control, sensing and fluorescence detection of polystyrene beads in a multi-fiber optical trap. *Opt. Express*, 13:2634, 2005.
- P. R. T. Jess, V. Garcés-Chávez, D. Smith, M. Mazilu, L. Paterson, A. Riches, C. S. Herrington, W. Sibbett, and K. Dholakia. A dual beam fibre trap for Raman microspectroscopy of single cells. *Opt. Express*, 14: 5779, 2006.
- I. P. Kaminow, R. E. Nahory, M. A. Pollack, L. W. Stulz, and J. C. Dewinter. Single-mode c.w. ridge-waveguide laser emitting at 1.55 microns. *Electronics Letters*, 15:763, 1979.
- H. Kressel and H. Nelson. *RCA Review*, 30:106, 1969.
- H. Kromer. A proposed class of heterojunction injection lasers. *Proc. IEEE*, 51:1782, 1963.
- S. C. Kuo and M. P. Sheetz. Force of single kinesin molecules measured with optical tweezers. *Science*, 260:232, 1993.

- M. Kurachi, M. Hoshi, and H. Tashiro. *Cell Motil. Cytoskel.*, 30:221, 1995.
- G. Leitz, E. Schnepf, and K. O. Greulich. Micromanipulation of statoliths in gravity sensing chara rhizoids by optical tweezers. *Planta*, 197:278, 1995.
- H. Liang, W. H. Wright, W. He, and M. W. Berns. *Exp. Cell Res.*, 204:110, 1993.
- R. B. Liebert and D. C. Prieve. Force exerted by a laser beam on a microscopic sphere in water: Designing for maximum axial force. *Ind. Eng. Chem. Res.*, 34:3542, 1995.
- M. P. MacDonald, G. C. Spalding, and K. Dholakia. Microfluidic sorting in an optical lattice. *Nature*, 426:421, 2003.
- M. Mammer, K. Helmerson, R. Kishore, C. Seok-Ki, W. D. Phillips, and G. M. Whitesides. Optically controlled collisions of biological objects to evaluate potent polyvalent inhibitors of virus cell adhesion. *Chem. & Biology*, 3:757, 1996.
- H. Masuhara, F. C. deSchryver, N. Kitumara, and N. Tamai. *Microchemisty-spectroscopy and chemistry in small domains*. North Holland, 1994.
- N. K. Metzger, K. Dholakia, and E. M. Wright. Bistability and hysteresis for optical binding of dielectric spheres in one dimension. *Phys. Rev. Lett.*, 96(068102), 2006.
- D. Meyerhofer. Characteristics of resist films produced by spinning. *J. Appl. Phys.*, 49:3993, 1978.
- S. L. Neale, M. P. MacDonald, K. Dholakia, and T. F. Krauss. All-optical control of microfluidic components using form birefringence. *Nature Materials*, 4:530, 2005.
- G. Palumbo, M. Caruso, E. Crescenzi, M. F. Tecce, G. Roberti, and A. Colasanti. Targeted gene transfer in eucaryotic cells by dye-assisted laser optoporation. *J. Photochem. Photobiol. B.*, 36:41, 1996.
- L. Paterson, B. Agate, M. Comrie, R. Ferguson, T. K. Lake, J. E. Morris, A. E. Carruthers, C. T. A. Brown, W. Sibbett, P. E. Bryant, F. Gunn-Moore, A. C. Riches, and K. Dholakia. Photoporation and cell transfection using a violet diode laser. *Opt. Express*, 13:595, 2005.
- L. Paterson, M. P. MacDonald, J. Arlt, W. Sibbett, P. E. Bryant, and K. Dholakia. Controlled rotation of optically trapped microscopic particles. *Science*, 292:912, 2001.
- R. Schieder, H. Walther, and L. Woste. Atomic beam deflection by the light of a tunable dye laser. *Opt. Comm.*, 5:337, 1972.
- S. Seeger, S. Manojembaski, K. J. Hutter, G. Futterman, J. Wolfrum, and K. O. Greulich. Application of laser tweezers in immunology and molecular genetics. *Cytometry*, 12:497, 1991.
- N. N. Sheftal, N. P. Kokorish, and A. V. Krasilov. Growth of single-crystal layers of silicon and germanium from the vapour phase. *Bull. Acad. Sci. USSR, Phys. Ser.*, 21:140, 1957.
- E. Sidick, S. D. Collins, and A. Knoesen. Trapping forces in a multiple-beam fiber-optic trap. *Appl. Opt.*, 36(25):6423, 1997.
- A. Simon and A. Libchaber. Escape and synchronization of a brownian particle. *Phys. Rev. Lett.*, 68:3375, 1992.
- R. W. Steubing, S. Cheng, W. H. Wright, Y. Namajiri, and M. W. Berns. Laser induced fusion in combination with optical tweezers: the laser cell fusion trap. *Cytometry*, 12:505, 1991.
- K. Svoboda, C. F. Schmidt, D. Branton, and S. M. Block. Conformation and elasticity of the isolated red blood cell membrane skeleton. *Biophys. J.*, 63:784, 1992.
- A. Terray, J. Oakey, and D. Marr. Microfluidic control using colloidal devices. *Science*, 296:1841, 2002.
- G. C. Tyrell, D. Marshall, J. Beckham, and R. B. Jackman. Chemical routes to gaas etching with low energy ion beams. *J. Condens. Matter*, 3:179, 1991.
- M. D. Wang, H. Yin, R. Landrick, J. Gelles, and S. M. Block. Stretching DNA with optical tweezers.

- Biophys. J.*, 72:1335, 1997.
- M. M. Wang, E. Tu, D. E. Raymond, J. Mo Yang, H. Zhang, N. Hagen, B. Dees, E. M. Mercer, A. H. Forster, I. Kariv, P. J. Marchand, and W. F. Butler. Microfluidic sorting of mammalian cells by optical force switching. *Nature Biotech.*, 23(1):83, 2005.
- X. F. Wang, J. J. Lemaster, B. Herman, and S. Kuo. *Opt. Engin.*, 32:284, 1993.
- X. Wei, B. J. Tromberg, and M. D. Cahalan. Mapping the sensitivity of T cells with an optical trap: Polarity and minimum number of receptors for  $\text{Ca}^{2+}$  signaling. *Proc. Natl. Acad. Sci. USA*, 96:18471, 1999.
- J. W. Whelan-Curtin. Private communication. 2002.
- H. Yin, D. Wang, K. Svoboda, R. Landick, S. M. Block, and J. Gelles. Transcription against an applied force. *Science*, 270:1653, 1995.